Search for Neutrino Bursts from Supernovae with the AMANDA Detector

Diplomarbeit

Humboldt-Universität zu Berlin
Mathematisch-Naturwissenschaftliche Fakultät I
Institut für Physik

eingereicht von

Andrea Silvestri
geb. am 30.11.1973 in Norcia

1. Gutachter. Prof. Thomas Hebbeker
2. Gutachter. Prof. Hermann Kolanoski

Berlin, Februar 2000

Abstract

The AMANDA high energy neutrino telescope is able to search for low energy neutrino bursts from supernova collapses. A copious number of positrons originating from a large flux of $\bar{\nu}_e$ would induce an excess on top of the counting rate background in all optical modules (OMs). A first full supernova analysis of the AMANDA-B10 array data is presented. The detector characteristics and methods used to search for burst candidates are discussed. A satisfactory long-term stability of a sub-sample of 170 selected OMs of a total of 302 OMs has been found. A moving average method of the combined counting rate of all OMs was used. A Maximum-Likelihood approach rejected efficiently non-Gaussian rate excesses which might fake supernova events. A Monte Carlo for data comparison and for signal prediction is presented. A total of 220 days of data from the detector operation in 1997 and 98 has been analyzed. No clear neutrino burst candidates have been found during this interval. A rate of one fake event per year is expected when setting the threshold to 90% detection efficiency for a supernova of SN 1987A type at a distance of 8.8 kpc. Presently a supernova search with AMANDA covers over 50% of the stars in the Galaxy with a S/N$\geq$ 1, assuming a *signal* S of 1 supernova per century in our Galaxy. On the basis of this data a 90% c.l. upper limit on the rate of gravitational stellar collapses in the Milky Way of 8.59 $events{\cdot}year^{-1}$ is derived. Scaled to the live-time of the LVD detector, this limit would correspond to 0.93 $events{\cdot}year^{-1}$, which is about twice worse than the LVD limit. An algorithm ASTA (AMANDA Supernova Trigger Algorithm) for real time supernova monitoring has been developed, giving no false alarms after test on 11 days live-time.

a mio fratello BENEDETTO

Sempre caro mi fu quest'ermo colle,
E questa siepe, che da tanta parte
Dell'ultimo orizzonte il guardo esclude.
Ma sedendo e mirando, interminati
Spazi di là da quella, e sovrumani
Silenzi, e profondissima quiete
Io nel pensier mi fingo, ove per poco
Il cor non si spaura. E come il vento
Odo stormir tra queste piante, io quello
Infinito silenzio a questa voce
Vo comparando; e mi sovvien l'eterno,
E le morte stagioni, e la presente
E viva, e il suon di lei. Cosí tra questa
Immensità s'annega il pensier mio:
E il naufragar m'è dolce in questo mare.

GIACOMO LEOPARDI

L'INFINITO Dai *Canti*.

Contents

1 Introduction

AMANDA is a high-energy neutrino telescope located at the geographical South Pole. The main goal of AMANDA is to search for high-energy neutrinos as a probe for the highest energy phenomena in cosmos and to open new observation windows to the Universe.

Neutrinos are interacting only weakly, and undeflected by interstellar magnetic fields they can travel astronomical distances providing hidden information complementary to that obtained from electromagnetic observations. Candidate astronomical neutrino sources are thought to be Active Galactic Nuclei (AGN) and Gamma Ray Bursts (GRBs), which might provide an accelerator mechanism of high-energy hadrons. Neutrinos could also be produced in the center of the Earth or the Sun, generated by annihilation of Weakly Interacting Massive Particles (WIMPs). The discovery of these particles would provide a clue for the understanding of the cold dark matter amount of the Universe. X-ray binary system and young supernova remnants might also be high-energy neutrino sources. Neutrino telescopes can also be used to search for exotic particles such as magnetic monopoles.

High-energy neutrino telescopes are deployed in transparent media like ocean or lake-water, or deep in Antarctic ice. Their principal aim is to achieve a large detection area and keep a relatively low energy threshold. The principle of detection is based on the arrival time of the Cherenkov light emitted by muons traveling through the clear medium. The light is detected by photo-multiplier tubes (PMTs) arranged on strings forming an array. The recorded arrival time distribution is the essential information to reconstruct the muon track, and subsequently to infer the origin of the high-energy neutrino.

The pioneering project of underwater telescopes was the meanwhile terminated DUMAND [Ste82, Pry88]. Other projects are BAIKAL [Kuz99], ANTARES [ANT97] and NESTOR [NES95].

Although AMANDA is a high-energy neutrino telescope, it can be used to search for low energy neutrino bursts from Galactic supernova explosions. However, only a time profile of the neutrino burst during the collapse phase can be measured. Additional information on the energy and direction of the supernova neutrinos is unlikely to be reconstructed in such a detector.

The most important neutrino reaction for supernova detection in ice is electron anti-neutrino absorption. A large number of MeV positrons radiating Cherenkov light would be generated due to these interactions of neutrinos with protons. Assuming a burst duration of tens of seconds, this light would give many hits in all optical modules (OMs). Although the signal for an individual OM will be statistically weak compared to the background, it can be significant when summing it over a large number of OMs. The main advantage for AMANDA compared to ocean based detectors with respect to supernova detection is the lower background in sterile Antarctic ice, thanks to the absence of bioluminescence and radioactive decay of ^{40}K.

Presently a SuperNova Early Warning System (SNEWS) [Sch99] intends to connect an international collaboration looking for coincidences of independent neutrino detectors to herald gravitational collapses. The detectors participating are Super-Kamiokande [Fuk98], LVD [LVD99] and MACRO [Ahl92], AMANDA and SNO [Hei98] are going to be included in the future.

This thesis starts with a detailed chapter on stellar evolution, supernova theory and neutrino bursts from supernovae.

Chapters 3-4 describe the AMANDA detector and give a brief summary of the present knowledge about the optical properties of the glacier ice at the South Pole.

Chapter 5 summarizes the possibility to detect supernova neutrinos with AMANDA.

Chapter 6 describes the hardware for the SN electronics.

Chapters 7-8 deal with data handling and with the basic behavior of the data and describes the non-Poissonian behavior of the dark noise background.
Chapter 9 gives a description of the Monte Carlo simulation used to study background and signal.
Chapter 10-12 deals with the methods used in the analysis and with the calculation of the signal prediction taking into account factors which influence the signal detection.
Chapter 13 deals with the performance of the detector, using the information coming from the ratio S/N as a function of distance and discussing the current capability of AMANDA to survey stars in our Galaxy.
The current upper limit of AMANDA on the rate of gravitational stellar collapse in the Galaxy is presented in Chapter 14, and the comparison with other experiments is discussed.
Chapter 15 discusses the possibility to connect AMANDA to a world wide supernova network and summarizes the triangulation principle to point back to a supernova.
The final chapter deals with the study and the development of a Supernova AMANDA Trigger Algorithm (ASTA).

2 Theory

2.1 What is a Supernova?

Burning its fuel, a star which has lived undisturbed, evolving peacefully for several million years, will eventually turn off its nuclear process, so that it can no longer support its own weight. The core of the star collapses and the star disappears in less than a second. The death of the star is the birth of the supernova. A supernova is an incredibly vast explosion disrupting completely the progenitor star, which is blown up into the interstellar medium. This explosion is one of the most wonderful and spectacular astrophysical events. For this reason astrophysicists wait in excited anticipation for the next visible supernova.
The definition *Supernova* was first introduced in 1930 by Baade and Zwicky [BZ34a] to distinguish the appearance of extremely luminous novae from ordinary novae [1]. The light output of the stellar explosion at the maximum light is extremely bright and corresponds to the whole amount of the light of all the rest of stars in the Galaxy. However, most of the observed supernovae do not belong to the Milky Way, but occur in very distant galaxies. About 700 supernovae were counted during the last decade [Suz94].
The rapid release of huge amounts of energy from a supernova is also associated with the process of neutron star and black hole formation. The shock wave caused by supernova explosions propagates through the interstellar medium and generates the material to form new stars.
Supernovae are very rare in our own Galaxy, and only 5 [TLS94] have been observed during the last millennium. The first reported supernova is dated from 1006 (Lupus), then the supernova of 1054 occurred, which gave rise to the Crab Nebula, and the third mentioned is the supernova of 1181 (3C58). Tycho Brahe discovered in November 1572 a supernova in the constellation Cassiopeia, now called Tycho's supernova. In October 1604, just three years after Tycho's death, Johannes Kepler, his student and assistant, observed a new star, now known as Kepler's supernova. In each of these historical cases, the star became the brightest star in the sky when it exploded.
These five supernovae occurred in a relatively close region of our Galaxy, in a distance range between $\sim 1.4 - 4.2$ kpc [Lon94, KZ97]. More distant supernovae which also exploded in the

[1] The classical *novae* are mentioned to be stellar explosions, which can increase the brightness of the new stars by more than 10 magnitudes [Lon94].

Galactic plane were not observed, because of the high opacity of interstellar dust. The last most spectacular event since Kepler's supernova occurred on 23 February 1987, when a blue supergiant star, Sanduleak $-69°$ 202, exploded in a satellite galaxy of our Milky Way, the Large Magellanic Cloud. With this event the astrophysics of supernova neutrinos began [Hir87, Bio87].

2.2 Stellar Evolution

2.2.1 The Hertzsprung-Russel Diagram

In order to understand how supernovae can occur and why these are rare events, it is important to understand how the progenitor stars are evolving. Stars are responsible for the most of the visible light of the Galaxy. The luminosity [2] L, is defined as the total radiated energy from the whole star surface in all frequencies per unit time. The study of stars is based on the measurement of their luminosity and surface temperature. In fact, from the luminosity-temperature diagram, known as *Hertzsprung-Russel (H-R) diagram* or as *color-magnitude diagram*, most of the peculiarities of stellar behavior can be observed. One of these in particular is that the stars are sitting along a well-defined band called *main sequence*, where the majority of stars are clustered in a region from the bottom right to the top left (see Fig.2.1).

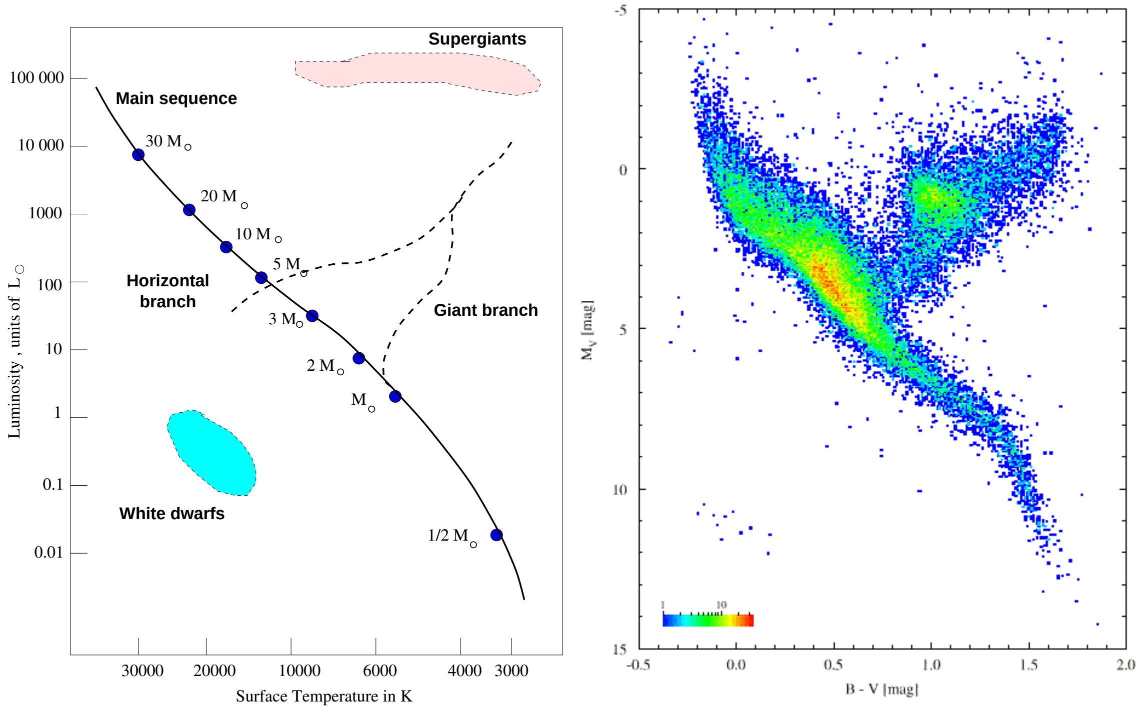

Figure 2.1: Left: a schematic representation of the H-R diagram (picture following [Lon94]). Notice how the mass itself distinguishes the different stars along the main sequence. Right: H-R diagram for 41704 single nearby stars determined from observations made by the *Hipparcos* astrometry satellite. Picture from [Gro99].

The more massive stars lie on the top left, and the less massive on the bottom right. Such a behavior can be described through their luminosity as a function of the star's mass. For stars with a mass in the range $1M_\odot < M_\star < 10M_\odot$, the relation follows a power law of the type: $L \propto M_\star^\alpha$, where the

[2] For references about astrophysical units and constants see App.A

exponent is $\alpha \approx 4$ and $M_\odot$ is the Sun mass. For stars with a mass less than $M_\odot$ and larger than $10M_\odot$, the power law is better described with an exponent $\alpha < 4$ [Lon94].
The presence of a star population starting at the location of the Sun towards the top right is known as the *giant branch*, while the region of stars extending across the diagram, from the giant branch is called *horizontal branch*. At low temperature and high luminosity, very massive stars are clustered, which are known as *supergiants*. Finally, blue and compact stars known as *white dwarfs* lie far away from the main sequence on the bottom left. Two questions arise from the star distribution on the H-R diagram: why do stars appear only in certain regions of the luminosity-temperature diagram? Why do stars evolve from one part to another distinct part of this diagram?
The answer to these questions is one of the main goals of the theory of stellar evolution.

2.2.2 Main Sequence

If the force of gravity were not balanced by the pressure gradient of the hot gas within the star itself, it would immediately lead to the collapse of the star. Stars are stable, thanks to the hydrostatic equilibrium maintained through the continuous generation of nuclear energy in their center.
What governs different nuclear reactions is the particular temperature reached at the center of the star. If the temperature T_{center} is less than $2 \cdot 10^7$ K, the conversion of hydrogen to helium is dominant, and 0.7% of the hydrogen rest mass is released in radiation energy. This released energy is the nuclear binding energy of helium and is the source of light radiated from the surfaces of stars. At this temperature, the primary energy source of the main sequence stars is the so called *p-p chain*, whose main reactions are:

$$\begin{array}{l} p + p \longrightarrow {}^2\text{H} + e^+\nu_e \\ {}^2\text{H} + p \longrightarrow {}^3\text{He} + \gamma \\ {}^3\text{He} +{}^3\text{He} \longrightarrow \alpha + 2p \end{array} \tag{2.1}$$

If the temperature T_{center} is larger than $2 \cdot 10^7$ K, the reaction cycle known as the *carbon-nitrogen-oxygen* (CNO) cycle dominates, where the hydrogen is also fused into helium by the C-N cycle provided that carbon, nitrogen, or oxygen are present to act as a catalyst [Lan99, Bah89]:

$$\begin{array}{l} {}^{12}\text{C} + p \longrightarrow {}^{13}\text{N} + \gamma \\ {}^{13}\text{N} \longrightarrow {}^{13}\text{C} + e^+ + \nu_e \\ {}^{12}\text{C} + p \longrightarrow {}^{14}\text{N} + \gamma \\ {}^{14}\text{N} + p \longrightarrow {}^{15}\text{O} + \gamma \\ {}^{15}\text{O} \longrightarrow {}^{15}\text{N} + e^+ + \nu_e \\ {}^{15}\text{N} + p \longrightarrow {}^{12}\text{C} + \alpha \end{array} \tag{2.2}$$

In the p-p chain, the released energy is transported through the central star's regions by *radiation*, whereas if the CNO cycle takes place, the central region where the energy is produced becomes unstable through the phenomenon of *convection*. Stars burning hydrogen to synthesize helium are very stable. In fact they remain for almost all their live inside the main sequence. So stars like the Sun are estimated to live undisturbed for 10^{10} years.
Once 10 % of the available hydrogen is converted into helium, a star evolves to the giant branch. At this stage the star has reached a limit known as the *Schönberg-Chandrasekhar limit* [3] and becomes

[3] In a historical paper Schönberg and Chandrasekhar studied the evolution of the stars of the main sequence, where they showed that the core of the star can evolve to an isotherm core due to the decrease of hydrogen during the burning. Furthermore they put an upper limit to the fraction of the total mass of hydrogen which can be exhausted, namely $\leq 10\%$ [SC42].

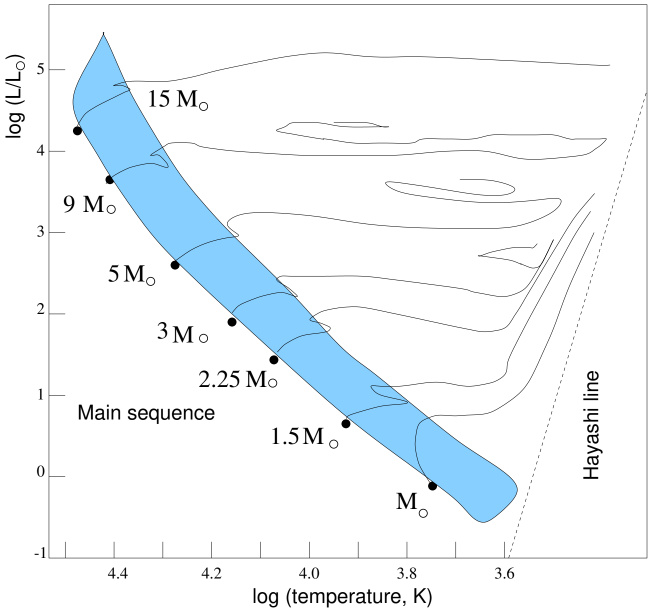

Figure 2.2: Evolutionary behavior for stars of different initial masses in the H-R diagram. (Picture following [MB81]). The stars spend most of their lifetime on the main sequence (dashed zone). For only a much shorter timescale they remain on the giant branch. Note that different stars-masses correspond to very different tracks in the diagram. The Hayashi line [WW96] which separates the allowed from the forbidden area is also indicated.

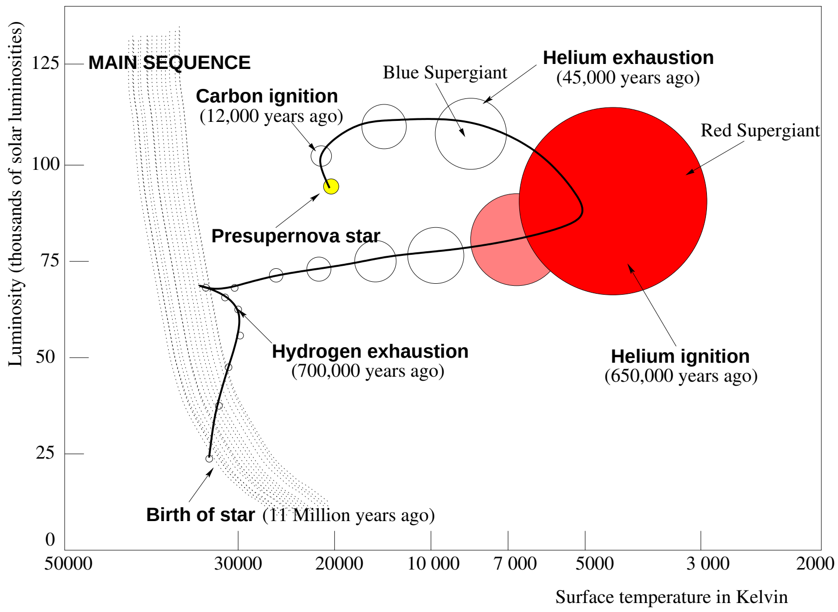

Figure 2.3: H-R diagram from a model evolution for the SN 1987A based on a calculation for a initial star mass of $M_\star = 18 M_\odot$, and lifetime $t(M_\star) = 1.1 \cdot 10^7$ years. Picture following [WW89].

unstable. The instabilities, due to the increased gravitation, can no longer be halted through the insufficient energy generation by hydrogen burning, so the star compensates this effect through its contraction. The outer envelope of the star expands so that the star becomes a giant.
The stars become cooler during the giant branch phase, and their convective outer layers expand

deeper towards their center. The maximal depth of the convective zone depends only on the effective temperature at the surface, T_{eff} (App.A). The lower T_{eff}, the deeper the convective zone will reach into the star. At total convection, (i.e. the convective zone spreads from the surface to the center of the star), the star has reached a limit. This limit divides the H-R diagram in two areas: the *allowed area* on the left of the line, where the hot stars of the main sequence are sitting; and the *forbidden area* on the right, which can only be touched but not exceeded by the cooler fully convective stars. This line, shown in Fig.2.2, is known as the *Hayashi line* [WW96].
The lifetime of the massive stars is much shorter than that of the small ones, because they exhaust their fuel much faster to support their large mass. Thus, the lifetime of a star is a function of its mass, which can be described with the following law: $t(M) \propto M/L \propto M^{-(\alpha-1)}$, where again $\alpha \approx 4$, or $\alpha < 4$ for $M_\star < M_\odot$ and $M_\star \gtrsim 10M_\odot$, respectively. The lifetime of the Sun is estimated to be $t_\odot \simeq 10^{10}$ years, while for more massive stars one obtains the following relationships: for $2M_\odot$, $t = 1.3 \cdot 10^9$ years, for $5M_\odot$ $t = 8 \cdot 10^7$ years, and for $M_\star \geq 10M_\odot$, $t(M_\star) \leq 10^7$ years [Lon94]. Massive stars with a mass $M_\star \gtrsim 8M_\odot$ are considered to be candidates for progenitor stars of supernovae [Ken84]. Fig.2.3 depicts the evolution of a star using a model for the progenitor star of SN 1987A [WW89, Woo97]. After the hydrogen-burning (Schönberg-Chandrasekhar limit), the core contracts and becomes hotter, and the outer envelope expands and cools. At this stage the star moves to the right to become a red supergiant. When the helium is exhausted, the envelope contracts again and the star becomes a blue supergiant. In this way heavier and heavier elements are burned successively until the iron-peak, where the nuclear reactions stop. Ultimately the iron-core collapses, triggering a supernova.

2.2.3 Dead Stars

After the Schönberg-Chandrasekhar limit, a star in the mass range $1M_\odot < M_\star < 4M_\odot$ evolves creating more and more convective regions within the outer layers, until it is totally unstable and the outer shells are blown off, becoming a *planetary nebula*. The star cools further and ends as a *white dwarf* (see also Fig.2.4). The evolution of stars with $M_\star > 4M_\odot$ is different. After the star has left the main sequence, the hydrogen-burning continues in an outer shell, and in the core helium is converted into carbon. In that form different nuclear reactions are switched on and the star will take up an 'onion-skin' structure, so that successive burning shells of hydrogen, helium, carbon, oxygen-neon, and silicon are created, with a central core of iron, for the most massive stars. Iron is the element with the greatest nuclear binding energy (see Fig.2.5). At this stage nuclear fusion stops because energy can no longer be produced by this process.
Here it is natural to ask the question, which type of objects could be formed at the end of a star's lifetime.
From the theory of stellar evolution it is well understood, that there are three types of 'dead stars' (see Fig.2.4). 'Dead' has to be interpreted as a star in which there is no longer any generation of nuclear energy. When fusion ends in a small star, the star shrinks slowly becoming a *white dwarf*, which is a very faint body. This is the first type of dead star, in which the internal pressure is supported by the pressure of electron degeneracy. The second and third class of dead stars are coming from *supernovae* due to the collapse of more massive stars with a mass $M_\star \gtrsim 8 \pm 1M_\odot$ [Ken84]. The maximum mass of the inner core, that a star can support against the gravitational forces by degeneracy pressure of electrons, is the *Chandrasekhar mass limit* [Cha31], given by $M_{Ch} = 5.836\ Y_e^2 M_\odot = 1.46M_\odot$ [Lon94], where $Y_e \approx Z/A$ is the electron ratio per baryon. Once this limit is exceeded, the core is compressed by its own gravity, so that both the temperature and the pressure are increasing. These conditions, instead of decelerating the collapse,

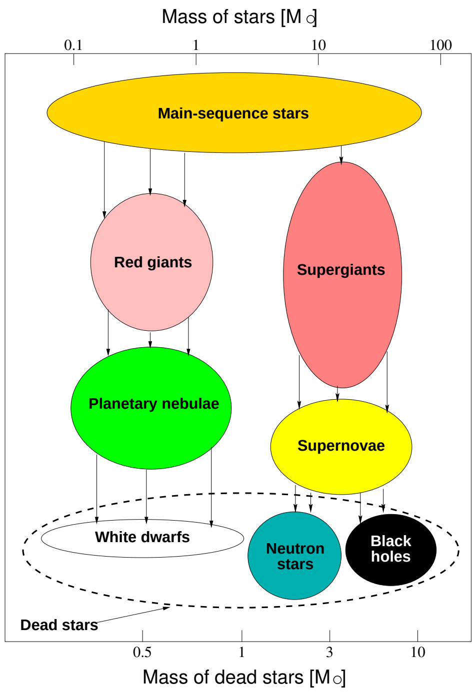

Figure 2.4: Schematic star evolution. The main sequence represents the initial position of the stars evolution. Their different evolutions are defined by their different masses. Finally they can become as dead stars white dwarfs, neutron stars or black holes. Picture following [Wor99].

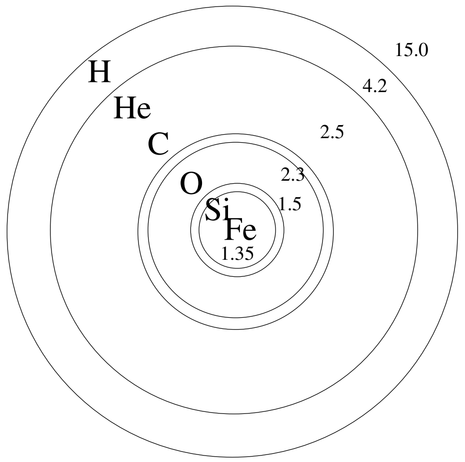

Figure 2.5: The Supernova progenitor structure. Here the different element shells of a pre-supernova $15M_\odot$ are indicated. In addition also the different masses of each shell in units of $M_\odot$ are outlined. Picture from [CB90].

lead to the opposite effect, accelerating it [Bah89]. The result of stellar collapses are *neutron stars*. If the nuclear matter were not sufficiently stiff, the core would collapse directly into a *black hole*. These are the second and third possibility of dead stars , respectively. The internal pressure of neutrons stars is provided by the pressure of neutron degeneracy. These stars are incredibly compact with a mass $M_\star \approx M_\odot$ and a radius about 10 km.
To sum up, a star in the mass range $1M_\odot < M_\star < 4M_\odot$ ends up as a white dwarf. More interesting for our topic are more massive stars with a mass range $4M_\odot < M_\star < 10M_\odot$ which might evolve

catastrophically to a supernova explosion. The probable remnants after a supernova explosion are neutron stars or black holes. There is great confidence that stars with a mass $M_\star \geq 10M_\odot$ might leave black holes.

2.3 Classification of Supernovae

The theory of supernova explosion distinguishes two fundamental explosion mechanisms. Type Ia supernova are thought to be the result of thermonuclear explosions of carbon-oxygen white dwarfs [HW90, Arn99] (see Sec.2.4). Type II supernovae (perhaps also Type Ib) are believed to come from more massive progenitor stars, which will evolve to core-collapse explosions (see Sec.2.5).
There is no unique way to classify the different types of supernovae. However, traditionally the fundamental classification scheme is based on the light spectrum of the supernova. The basic distinguishing property considered is whether or not hydrogen is present in the spectra. In 1939 Minkowski was the first to define a supernova Type II or Type I, whose light spectra show evidence of hydrogen or not, respectively. This is a first general distinction, which is further subdivided in subclasses, as is shown in Fig.2.6. The Type II supernovae are subdivided through the features of their *light curve*, the time evolution of their luminosity, and through their maximum light spectra. Type I supernovae are distinguished by their Si content. Type II supernovae which show a pronounced plateau in the early light curve, are called SN II-P, whereas those with a linear decline after the peak, are called SN II-L, (see Fig.2.7). SN1987A was a peculiar case, its light curve behavior could not be assigned to any precedent Type II light curves. This exception was attributed to the nature of its blue compact progenitor star [HW90].

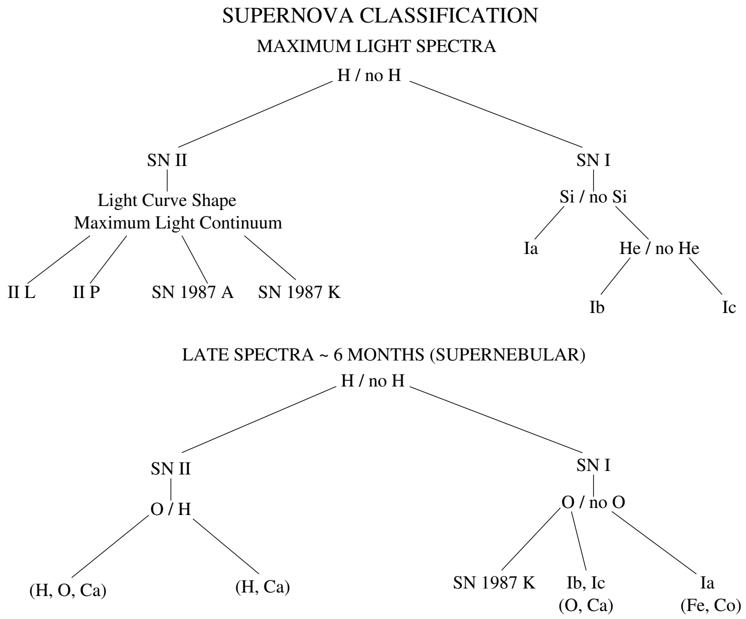

Figure 2.6: Classification of supernovae. See text for details and further discussion. Picture from [HW90]

Looking at the later phase of the supernova light curve, usually six months after the maximum light, one can classify supernovae by peculiarities of their late-time spectra. The Type II supernovae, also at the late phase, show strong Balmer lines, which confirm the hydrogen presence at the early phase. However, their spectra look different due to the emission of heavier elements (see

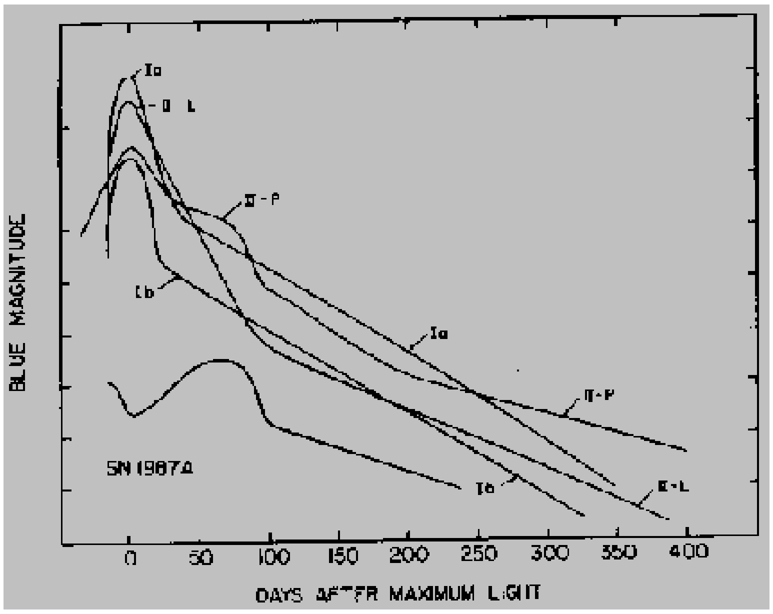

Figure 2.7: Schematic light curves of various types of supernovae. Note the very different behavior of the SN1987A light curve. Picture from [HW90].

Fig.2.6). Curious is again the event SN1987A, which is considered a Type II supernova, but has an ultraviolet spectrum during the late phase looking similar to that of Type Ia and Ib.
Tab 2.1 summarizes some key parameters needed to determine the nature of supernovae explosions and in particular to identify the development of their spectra. The radius of the progenitor determines the form of the ultraviolet spectrum. The peak and the tail luminosity are determined from the amount of ^{56}Ni, while the envelope composition gives the form of the post-maximum light curve. Important are also winds, which generate radio emission before the explosion [HW90]. Furthermore it is believed that some supernovae leave neutron star remnants, whereas other are expected to be completely disrupted.

Property	Ia	Ib	II-P	II-L	SN 1987 A
Initial radius R_0 (cm)	$\lesssim 10^{11}$	$\gtrsim 10^{12}$	$\gtrsim 10^{16}$	$\gtrsim 10^{16}$	$\sim 3 \cdot 10^{14}$
^{56}Ni $(M/M_\odot)$	> 0.6	0.15?	0.075?	0.6?	0.075
Envelope mass $(M/M_\odot)$	None	He (< 5)	H $(\gg 1)$	H(?)	H/He (~ 10)
Winds/circumstellar nebula	Negligible?	Yes	Yes	Yes	Yes(small)
Neutron star	No	Yes?	Yes?	No?	Yes(finally?)

Table 2.1: Key properties of supernova explosion. Table from [HW90].

2.4 Type Ia SN-Thermonuclear Explosions

White dwarfs are thought to be the progenitors, through runaway thermonuclear reactions, of Type Ia supernova explosions. However, at the moment there is no unique scenario, which leads from the evolution of the progenitor star to an explosion [Arn99]. There are two different pictures, which are the following for Type Ia supernovae: (1) A growing structure is formed through matter accretion in

a binary pair system, where a white dwarf accretes matter from a neighbor companion. (2) A merge system is formed through a pair of white dwarfs. While the accretion models favor a mechanism, where ^{12}C ignites in the core of the white dwarf, the merge scenario presumes a result from a combined mass, which exceeds the Chandrasekhar mass leading to explosion. The total energy released in the thermonuclear Supernova explosion is estimated to be of $O(10^{51})$ erg [Suz94].
These thermonuclear explosions result in a weaker neutrino burst than that of core-collapse supernovae (Type II, Ib, see Sec.2.5). The typical energy emitted by neutrinos comes either from thermal neutrinos or from neutrinos produced through electron capture. The order of magnitude of this neutrino energy is not more than a few MeV. Since the neutrino mean free path is longer than the white dwarf radius ($\lambda_\nu > R_{WD}$), all emitted neutrinos escape freely from the white dwarf. They carry away only a small fraction of the thermonuclear energy released, which is estimated to be $O(10^{49})$ erg, i.e. $\sim 1\%$ of the total energy released [Suz94] within a burst time scale of $\sim$ 0.2 - 60 sec. For this reason neutrinos do not play an important role for Type Ia supernovae.

2.5 Gravitational Collapse

2.5.1 General Considerations

Type II and Type Ib supernovae are thought to be produced by a gravitational core-collapse of massive progenitor stars with a mass $M_\star \gtrsim 8\ M_\odot$.
Baade and Zwicky were first to connect supernova explosions with neutron star formation in 1934 [BZ34b], and the theory that describes neutrino bursts implicated by supernovae and neutron stars has been developed especially during the last four decades. The phenomenon of the supernova touches several fields of physics, from nuclear to plasma physics and hydrodynamics, from astrophysics and stellar theory to neutrino physics. The explosion mechanism of a supernova develops in different stages, from the progenitor star formation to the collapse phase triggering the supernova onset and liberating the emergent neutrino burst, which precedes the emission of the light.
The gravitational energy liberated by core collapse is estimated to be

$$\Delta E_G = -\left(\frac{GM_{core}^2}{R_{Fe\ core}} - \frac{GM_{core}^2}{R_{Neutro\ Star}}\right) \sim O(10^{53})\text{erg}. \tag{2.3}$$

which represents the difference in the binding energy between the core and the growing neutron star [Suz94, Bur90]. The second term is dominant, due to the tiny neutron star radius (10 km only). This incredible amount of energy is distributed in different forms as follows. The optical emission which corresponds to the total light radiated, amounts to only ~ 0.01 % of the gravitational energy, i.e. E_{rad} is of $O(10^{49})$ erg. The kinetic energy of the debris is just 1 % of the gravitational energy, i.e. E_{rad} is of $O(10^{51})$ erg. Full 99 % of the released energy is emitted in form of neutrinos, E_ν is of $O(10^{53})$ erg [Bur90]. In contrast to the thermonuclear explosion, here neutrinos play the fundamental role. Because of the profound opacity of the dense core to light, the neutrinos are the only messengers, which give us the possibility to 'see' directly the supernova core.

2.5.2 Progenitor Structures

Results of several model calculations let argue, that at the collapse phase there might exist two distinct families of core structures: (1) progenitor stars with a small and compact core (iron or O-Ne-Mg) at low entropy ($S < 1$ Boltzmann constant per baryon), which show a steep density profile at the outer mantle. (2) progenitor stars with a more massive core at high entropy ($S \geq 1$), which show a slower decay of the density profile [BHF95]. Fig.2.8 shows the density profile as a function of the interior mass coordinate. The first core-family (11, 12, $15M_\odot$) and the second one (20, $25M_\odot$) are clearly distinguishable. The main differences between the two core structures are, that the smaller cores accumulate mass from outer layers more slowly, but explode easier. For heavier cores, the mass accretion rate $\dot{M}$, i.e. the capability to accumulate mass from the outer layers of the star can be large enough to slow down the explosion and even abort the supernova [BHF95].

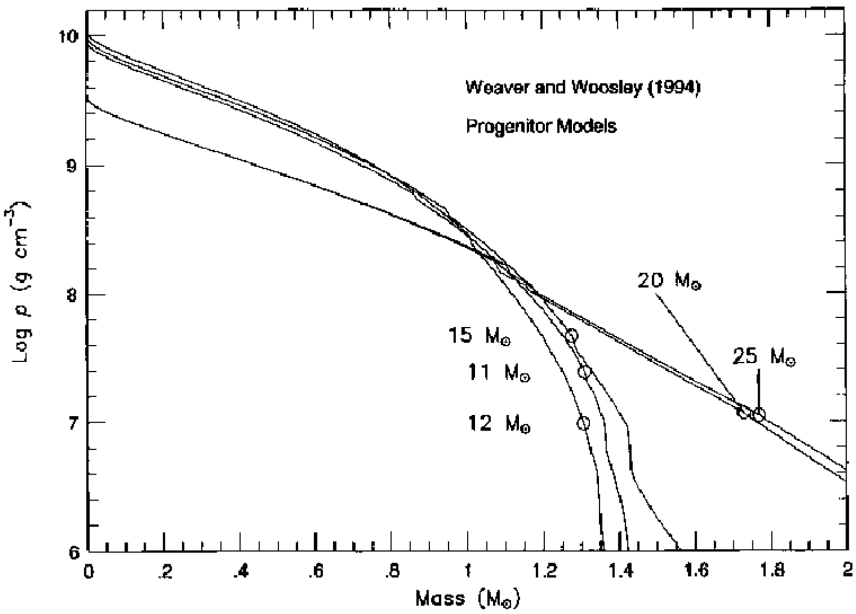

Figure 2.8: Density profile as a function of interior mass up to $2M_\odot$ for different models performed by (Weaver and Woosley, 1994). Note the different behavior of the density profile for the two families of core structures. See text for details. Picture from [BHF95]

2.5.3 Supernova Onset

In a hydrodynamic framework it can be understood, why a progenitor star becomes unstable and under which particular conditions the onset of the collapse appears. The stability of the core depends on the *adiabatic index* Γ_S of the matter [CB90], which is defined as

$$\Gamma_S \equiv \left(\frac{\partial \mathrm{ln} P}{\partial \mathrm{ln} \rho} \right)_S \tag{2.4}$$

where P, ρ and S are the pressure, the density and the entropy of the matter, respectively. The range of values, that the adiabatic index can take, is between $\Gamma_S = 5/3$ for a non-relativistic and $\Gamma_S = 4/3$ for a relativistic ideal gas [Suz94]. Two processes cause the drop of Γ_S to the critical value $\Gamma_{critic} < 4/3$, where the star starts to collapse:

1. Electron capture
2. Nuclear photodissociation.

The inner core (Fe or O-Ne-Mg) increases its mass with the ashes from the burning until the Chandrasekhar limit and becomes unstable because of these two fundamental processes.

Electron Capture When the Fermi energy ϵ_F of electrons within the core exceeds the threshold energy of the electron capture reactions

$$\begin{array}{llll} {}^{24}\mathrm{Mg} + e^- & \longrightarrow {}^{24}\mathrm{Na} + \nu_e & \epsilon_0 = 5.513\ \mathrm{MeV} \\ {}^{56}\mathrm{Fe} + e^- & \longrightarrow {}^{56}\mathrm{Mn} + \nu_e & \epsilon_0 = 3.695\ \mathrm{MeV} \end{array} \tag{2.5}$$

(with ϵ_0 being the threshold energy for electron capture [Arn96, Suz94]), the collapse of the star is triggered. The deficit of electrons causes a decrease of the internal pressure. This is the stage, where the core starts to collapse. During the triggered collapse phase the Fermi energy of the electrons increases further, so that more and more electrons are further captured. Therefore the collapse accelerates.

Iron Photodissociation The second process responsible for the core instability, known as *endothermic photodissociation of nuclei*, takes place once the temperature climbs up to $T > 5 \cdot 10^9$ K [Suz94]

$$^{56}\mathrm{Fe} + \gamma \longrightarrow 13^4\mathrm{He} + 4n - 124.4\ \ \mathrm{MeV} \tag{2.6}$$

The increase of temperature and internal energy, due to the further contraction in the collapse phase, is quickly exhausted by this endothermic reaction. Therefore, the pressure does not increase sufficiently to stop the core-collapse.
Stars with less massive cores ($M_\star \lesssim 12 - 15 M_\odot$) become unstable due to electron capture, more massive core stars reach instability by photodissociation. Note, that the core-collapse contracts matter to higher and higher density and temperature, which should decelerate the collapse, but these extreme conditions favor electron capture and photodissociation, which in the contrary accelerate the core-collapse.

2.5.4 Neutrino Trapping

Neutrino trapping is of fundamental importance for supernova physics. The dominant source of opacity to neutrinos is the existence of the neutral current of the weak interaction. Opacity during the core-collapse phase is due to *coherent scattering of ν_e off nuclei* which has a cross section proportional to the square of the mass number A, $\sigma_{\nu N} \propto A^2$ [Bah89]. During the collapse stage, only ν_e's are produced copiously by electron capture, which can escape from the core, before it becomes opaque for them. The critical density, where the core starts to become opaque, is roughly $\rho_{critic} \gtrsim 3 \cdot 10^{10}\ \mathrm{g/cm^3}$ [Suz94]. At this stage, the corresponding *mean free path* of the neutrinos becomes shorter than the radius of the core, i.e. $\lambda_{\nu_e} < R_{core}$. Consequently neutrinos form, within the dense core, a neutrino-volume known as *neutrinosphere*. The neutrinosphere surface defines the limit of the neutrinosphere, which separates the inner opaque region from the outer transparent region, where neutrinos can escape to infinity. Within the opaque region the neutrinos can only diffuse, and their diffusion time, for a core density $\rho_{core} \sim 10^{11} - 10^{12}$ g/cm^3, can be written as a function of core radius and neutrino mean free path [Suz94]

$$\tau_{diff} = \frac{3 R_{core}^2}{c \cdot \lambda_{\nu_e}} \tag{2.7}$$

Since this diffusion time $\tau_{diff} \sim O(sec)$ is larger than the collapse time of the core $\tau_{dyn} \sim O(msec)$, the neutrinos cannot escape during the collapse phase. The neutrinos are trapped.
At this extreme density, once neutrinos are trapped, they start to become degenerate like the electrons in the core. It is interesting to note, that neutrinos influence also the nuclear status of the core.

At first, through the electron capture, the nuclei become neutron-rich, but after the trapping, neutrino degeneracy suppress further neutronization. The cause of that is the Pauli exclusion principle, which forbids neutrinos to be at the same quantum status and stops the electron capture.

2.5.5 Core Bounce

Homologous Core The dynamics of collapse separates the core into two dynamical regions:
(1) The inner core-collapse, which occurs within the subsonic region, i.e. where the sound speed is larger than the magnitude of the infall velocity. This region represents the *homologous* core, where the infall velocity is proportional to the radius of the core.
(2) The outer core-collapse, which occurs as supersonically free falling, outside the sonic point (the point in the star where the sound speed equals the infall velocity), where the velocity is proportional to the inverse square root of the radius [May90]:

$$\begin{array}{ll} v \propto r & subsonic\ inner\ core \\ v \propto \frac{1}{\sqrt{r}} & supersonic\ outer\ core \end{array} \tag{2.8}$$

The mass of the homologous core is related to the Chandrasekhar mass. The Chandrasekhar mass is a function of the lepton fraction Y_L, $M_{Ch} = 1.457(Y_L/0.5)^2 M_\odot$, where $Y_L = Y_e + Y_{\nu_e}$ is the electron lepton fraction per baryon. After neutrino trapping the value of the lepton fraction is still $Y_L \approx 0.30 - 0.38$ [Bur90, Suz94], which corresponds to a core mass $M_{core} \approx 0.5 - 0.8 M_\odot$. Note that the mass of the inner core increases with the square of the lepton fraction ($M_{innercore} \sim M_{Ch} \propto Y_L^2$). The typical dynamical time scale for the inner core is much shorter than the time scale for the outer core, which means that the homologous core contracts and falls much faster, leaving behind the free infall of the outer mantle [Suz94].

Bounce When the density of the infalling subsonic inner core exceeds nuclear density ($\rho_{center} > \rho_{nuclear} \sim O(10^{14})$ g/cm^3) [May90], the matter achieves the incompressible nature of uniform nuclear matter. At this point the adiabatic index Γ_S (see Sec.2.5.3) reaches the critical value of $4/3$. This is the dramatic situation of the halting of the collapse, in which the subsonic inner core bounces back with a typical time scale of $O(msec)$ [May90].
The dimension of the unshocked core, i.e the inner region of the core below the launched shock wave, can be thought of as that of the homologous collapsing core, which locks up a mass region of $M_{unshocked} \approx 0.6 - 0.9 M_\odot$ with a radius $R_{unshocked} \approx several \cdot 10$ km. This dimension depends quadratically on the trapped lepton fraction Y_L, since $M_{unshocked} \propto Y^2_{Ltrapped}$. A tremendous pressure wave is generated, which propagates outwards to the outer core. At the boundary between the inner core and the supersonic outer core, the wave clashes with the infalling core producing a *shock wave*. The gravitational binding energy of the unshocked inner core corresponds roughly to the initial energy of the shock wave E_{shock}, which can be written as follows [JML85]

$$E_{shock} \sim \frac{GM^2_{unshocked}}{R_{unshocked}} \sim \text{several} \cdot 10^{51}\text{erg}. \tag{2.9}$$

2.5.6 Core Explosion

Comparing the kinetic energy of the supernova debris of $\sim 10^{51}$ erg from observations, with the previously estimated shock energy $E_{shock} \sim several \cdot 10^{51}$, one would expect, since $E_{shock} \gtrsim E_{obs}$, that the shock wave propagates through the outer star envelop and finally causes the supernova explosion. However, during the propagation of the shock wave through the outer core, some processes occur, which impede further evolution of the outgoing shock.

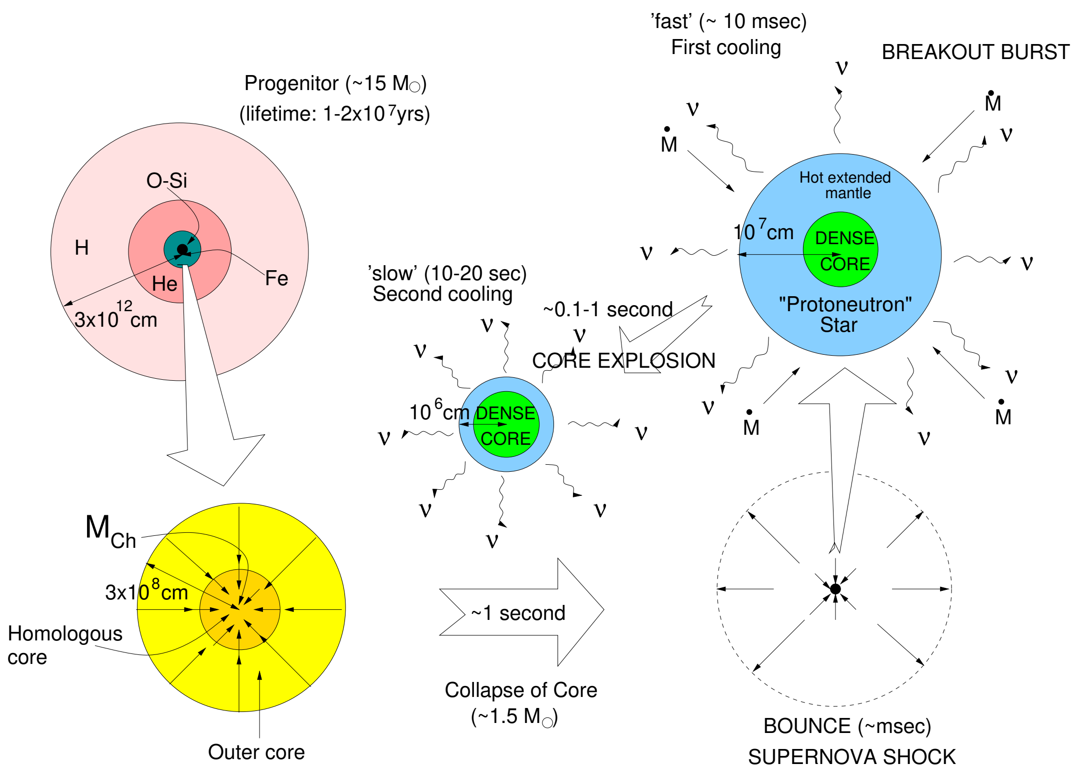

Figure 2.9: Schematic evolution from a progenitor star to core explosion. First neutrino burst (breakout burst) during the first cooling of the outer core, ultimate neutrino burst of 10-20 sec during the slower cooling of the inner core. Picture following [Bur90].

Prompt Mechanism The shock passage heats up the matter of the infalling supersonic core so much that photodissociation of nuclei occurs (Eq.2.6). The process of photodissociation exhausts the thermal energy just produced by the shock itself. Moreover the free protons, just created by photodissociation, have a larger electron capture cross section than the heavy nuclei. Consequently, electron capture in the shocked matter is further favored, so much that the local pressure decreases extremely behind the shock front. The decrease of the lepton fraction implies the drop of the pressure, $P_e \propto Y_e^{4/3}$ [Suz94], which should push out the shock wave, to the point that the shock propagation might stall without successful supernova explosion [Bru87, MB90].
If, in the opposite case, the shock wave successfully propagates through the outer core without stalling, a hydrodynamic core explosion is liberated in a time scale of $\sim$ 10 msec [Bru87, HNW84]. This explosion is known as the *prompt mechanism*. Most of numerical models argue, that the prompt mechanism can be successful only under the constraints of: (1) a small and cool core, which makes the propagation of the shock easier. (2) high contraction of the core and consequent large release of gravitational energy. Currently, the prompt shock mechanism seems to be disfavored, since in all models the shock stalls and prompt explosion fails [Mez98].

Delayed Mechanism If the prompt explosion aborts, due to the shock stall, then the infalling supersonic outer core overcomes the shocked matter, generating an inward moving *accretion shock*,

with a radius of $O(100)$ km. Therefore the supernova does not appear and the non-halted star collapses further into a black hole. Nevertheless the stalled shock wave can be revived by the phenomenon of the so-called *neutrino heating*. Bethe and Wilson were first to postulate such a thesis in 1985 [BW85].
A small fraction of produced neutrinos, in the hot region behind the stalled shock front, can escape from the dense inner core and quickly be absorbed from the free nucleons just produced by photodissociation due to the shock passage (Eq.2.6). The neutrinos then heat up the matter mainly through the following reactions: neutrino absorption, pair annihilation of the most energy neutrinos (ν_μ, ν_τ), and electron scattering

$$\begin{array}{llll} \nu_e\, n \longrightarrow p\, e^-, & \bar{\nu_e}\, p \longrightarrow n\, e^+; \\ \nu\, \bar{\nu} \longrightarrow e^+\, e^-; & \nu\, e^\pm \longrightarrow \nu\, e^\pm. \end{array} \tag{2.10}$$

In this way, neutrinos pour thermal energy into the region behind the shock front, driving within the shocked matter vigorous boiling referred as a *hot bubble* [BHF95]. The bubble is now sufficiently hot to expand and push out the stalled shock, reviving the shock spread. This is the so-called *delayed mechanism*. Compared to the typical time scale of the prompt mechanism of $\sim$ 10 msec, the delayed explosion time scale is to the order of 0.1-1 sec. However, a better understanding of neutrino transport is needed to confirm the delayed mechanism as the true explosion mechanism. Moreover it is argued that for the delayed explosion the contribution of convection due to Rayleigh-Taylor and Kelvin-Helmholtz instabilities should be essential both within the hot bubble and in the center [BHF95, Suz94]. Without convection boost in the driving neutrino luminosity, also the delayed mechanism would fail [BHF95].

2.5.7 Two Dimensional Supernova Explosion Model

The models referred to above were all 1-dimensional simulations, (i.e all calculations related in a spherical spatial configuration), the conclusions of a two dimensional model are rather different. In one dimension, the problem is the too small shock radius and the high density due to the subsequent post-shock accretion, which caused a large pressure and mass accretion rate $\dot{M}$. In two dimensional models with the same progenitor stars, the shock through neutrino heating leads to an explosion without stalling [BHF95]. However, convection and Rayleigh-Taylor and Kelvin-Helmholtz instabilities are fundamental ingredients also in two dimensional simulations to lead to successful core explosions. A delicate balance is set before the explosion, which is influenced positively by neutrino heating and convection, and negatively by electron capture, neutrino loss and large mass accretion rate. By some critical condition, the balance is tipped in favor of the positive dynamic expansion. The conclusion of this scenario is that the neutrino heating is a crucial phenomenon to drive a supernova explosion.

2.5.8 Cooling and Stellar Explosion

Protoneutron Star (PNS) Formation During the shock propagation, the unshocked inner core establishes a configuration of hydrostatic equilibrium in a time scale of $O(\mathrm{msec})$. Meanwhile the accretion shock through the infalling outer core forms a further hot outer mantle around the inner core. In this way the protoneutron star (PNS) grows through the cool unshocked inner core with lower entropy ($S \sim O(1)$) and the hot shocked mantle with high entropy ($S \sim O(10)$). Thus, as shown above, the core evolves achieving the critical conditions, which decide its explosion.

Neutrinos, during the diffusion time (Eq.2.7), carry away from the PNS both the trapped lepton number Y_L in $\tau_L \sim 3$ sec and thermal energy in $\tau_{th} \sim 10$ sec [Bur90]. The evolution of the PNS into a neutron star can be divided in two distinct stages:

1. the stage of rapid cooling of the shocked outer mantle;
2. the stage of slower cooling of the inner core.

As will be shown in Sec.2.6.2, 2.6.3, these two stages of the core cooling can be distinguished through distinct neutrino signatures. The shocked outer core cools down quickly, and because of its relatively low density, neutrinos can escape freely ($\lambda_\nu > R_{outercore}$). This gives rise to the prodigious electron neutrino burst know as *breakout burst* implicating the phenomenon of *deleptonization*. After just one second, the radius of the PNS becomes of the order of ~ 10 km, the corresponding final radius of the growing neutron star, while its initial radius was of ~ 100 km.
The gradual decrease of the entropy causes the contraction of the outer core, with a subsequent increase of its temperature. But after ~ 10 sec the temperature profile achieves a shape of monotone decrease from the center to the surface of the star. The central region now starts to cool down. At this stage further deleptonization takes place in the whole PNS, and it becomes a neutron star.

Supernova Explosion After the core explosion, the penetrating shock wave reaches the outer layers of the star, which are blown off into the interstellar medium. The shock wave breaks through the photosphere (not to be confused with the neutrinosphere), which leads to the final stage, observed as a supernova. In the soft outer stellar envelope, where the binding energy is small and processes like photodissociation of nuclei or neutrino loss are negligible, the shock proceeds without obstacles. The propagation time of the shock depends on the size of the stellar radius, nevertheless generally the order of magnitude is between several hours to days.
However, before the burst of electromagnetic waves can be recognized as supernova explosion, a prodigious neutrino burst from the core reaches us in advance, signaling the occurrence of a supernova and the birth of a neutron star.

2.6 Neutrinos from Supernovae

2.6.1 Neutrino Interactions in the Supernova Core

The following discussion is focused on neutrinos from core-collapse supernova explosions. In the extreme conditions of the supernova core ($T \lesssim 100$ MeV; $\rho \lesssim 10^{15}$ g/cm^3; $0 \lesssim Y_e \lesssim 0.5$) the main neutrino interactions occurring in the core are summarized in Eq.2.11. Heavy nuclei are represented by 'A' ; 'N' is a nucleon, either proton or neutron; 'l' has to be interpreted as either an electron 'e' or a muon 'μ', since the available energy in the core $O(100)$ MeV is not sufficient to create the mass of a 'τ' lepton. Hereafter the neutrino species $\nu_\mu,\ \bar{\nu}_\mu,\ \nu_\tau,\ \bar{\nu}_\tau$ are collectively denoted through the symbol "ν_μ''.
Electron neutrinos ($\langle E_{\nu_e}\rangle \sim 10$ MeV) are produced during a supernova explosion especially by: (1) electron capture on free protons; (2) electron-positron pair annihilation; (3) plasmon [4] decay. During the collapse phase the reaction: (4) electron capture by heavy nuclei becomes important. Due to the greater number of electrons compared to positrons within the core, the positron capture

[4]The plasmon is the quantum in plasma, whose propagation in plasma can be compared with the phonon propagation in a solid body.

by free neutrons producing $\bar{\nu}_e$ of $(\langle E_{\bar{\nu}_e}\rangle \sim 13$ MeV) is suppressed by electron capture on protons. The very few muon and tau neutrinos are only produced via neutral-current channels through processes (2) and (3) with $(\langle E_{``\nu''_\mu}\rangle \sim 24$ MeV)

Once neutrinos are produced, they interact with matter. The main processes involved are: (5) the inverse reactions of the above described neutrino production processes; (6) elastic scattering off free nuclei and nucleons (protons, neutrons); (7) neutrino scattering off electrons [MB90, Suz94].

$$\begin{array}{lll} p\,e^- \longleftrightarrow n\,\nu_e, & n\,e^+ \longleftrightarrow p\,\bar{\nu}_e, & A\,e^- \longleftrightarrow A'\,\nu_e \\ e^-\,e^+ \longleftrightarrow \nu\,\bar{\nu}, & plasmon \longleftrightarrow \nu\,\bar{\nu}, & \\ N\,N' \longleftrightarrow N\,N'\,\nu\,\bar{\nu} & & \\ N\,n \longleftrightarrow N\,p\,l^-\,\bar{\nu}_l, & N\,p\,l^- \longleftrightarrow N\,n\,\nu_l & \\ \nu\,N \longleftrightarrow \nu\,N, & \nu\,A \longleftrightarrow \nu\,A, & \nu\,l \longleftrightarrow \nu\,l, \end{array} \tag{2.11}$$

2.6.2 The First Fast Cooling Phase

In the early phase, neutrinos created through electron capture behind the shock front are still deep below the neutrinosphere surface. As the shock reaches the neutrinosphere surface, the 'newly' produced electron neutrinos are able to escape freely outside. This is the great neutrino burst known as the *breakout burst* or *neutronization burst* with a peak luminosity of $O(10^{53})$erg sec^{-1} [MB90]. The order of magnitude of the burst time duration is roughly the same of the shock propagation timescale of $O(10)$ msec. However, due to its very short duration time, the energy carried out during this burst is only of $O(10^{51})$ erg ($\sim 1\%$ of the total neutrino energy E_ν subsequently radiated). Fig.2.10 depicts the evolution of the neutrino luminosity from a successful delayed mechanism of

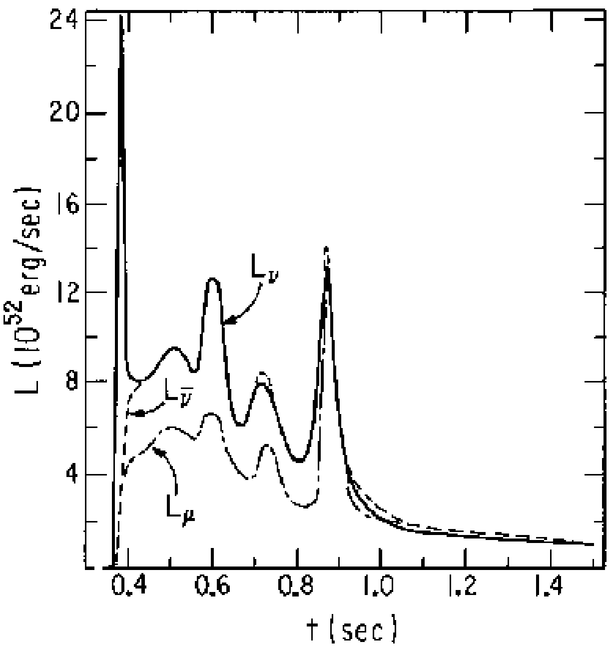

Figure 2.10: Neutrino luminosity versus time for all neutrino species from a 25 $M_\odot$ progenitor star. The solid line (L_ν) represents the electron neutrino luminosity, the dashed line ($L_{\bar{\nu}}$) is the antielectron neutrino luminosity, while the dash-dot-dash line (L_μ) means the muonic "ν''_μ neutrino luminosity. Note that, to permit a better graphic presentation, the electron capture burst peak is drawn one-half its actual height. Picture from [MW87].

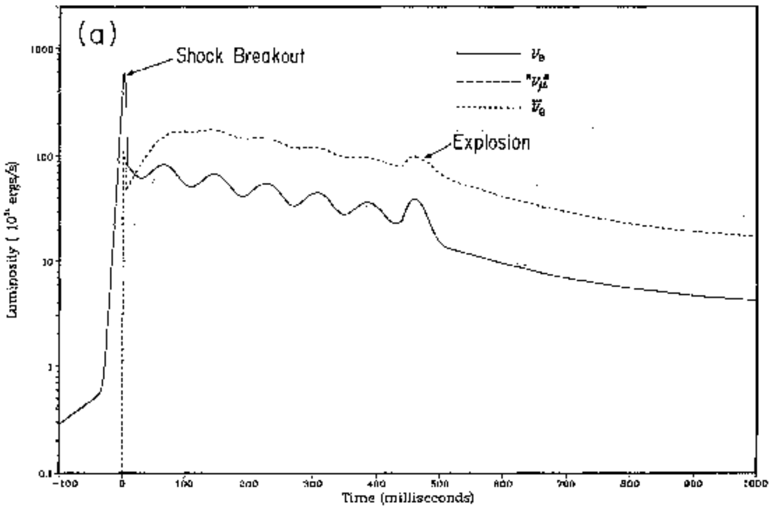

Figure 2.11: Luminosity profile versus time for all types of neutrinos represented as ν_e, $\bar{\nu}_e$ and "ν_μ''. The electron neutrino luminosity is peaked at the shock breakout, as the shock wave penetrates its neutrinosphere. After the oscillation behavior the explosion spot is also indicated. Picture from [BKG92].

a model computed by Mayle and Wilson [MW87]. The first very prominent peak of the electron neutrino luminosity is due to the breakout burst. However, after the shock breakout, the behavior of the three curves is quite similar. The oscillation within the first second after the burst, is due to the variation of the mass accretion rate $\dot{M}$ during the shock stagnation. Note that this oscillation is a property only of the delayed mechanism, which makes it the most important characteristic for a future detection through large neutrino telescopes. Through this detection it can be decided if the delayed mechanism is the right one. The spike at ~ 0.9 sec indicates the core explosion, after that the luminosity decay gets a monotonous shape, which indicates the end of the matter accretion [MW87].

A model computed by Burrows, Klein and Gandhi (BKG) takes into account the features from both prompt explosion [Bru87, MB90] and delayed explosion models [BW85]. The BKG model simulates also nicely the rapid rise of the electron neutrino luminosity (L_{ν_e}, first peak), due to the accelerating rate of electron capture during the collapse phase, as in Fig.2.11. The penetration of the shock through the electron neutrino-sphere produces the prodigious shock breakout burst. At shock breakout the first peaks of $\bar{\nu}_e$ and "ν_μ'' luminosities exhibit a sudden"turn-on" (see Fig.2.11 dashed line). This feature is a typical behavior of the prompt mechanism [MB90]. The huge spike of the L_{ν_e} in Fig.2.11 indicates only the neutronization phase of the low density outer mantle of the PNS, and not the neutronization of the whole PNS. The gradual increase of the $\bar{\nu}_e$ and "ν_μ'' luminosities at ~ 20 msec is due to the passage of the shock wave through the neutrinosphere. From this time until the core explosion, the "ν_μ'' luminosity (L_{ν_μ}) amounts to $\sim 1/2$ of the total luminosity, and the ν_e and $\bar{\nu}_e$ ones (L_{ν_e}, $L_{\bar{\nu}_e}$) with a similar decay shape, only to $1/4$ of the total luminosity respectively [MB90, BKG92].

The subsequent accretion rate may gradually decay with a consequent gradual decay in the luminosities until the delayed explosion (around 500 msec), as shown in Fig.2.11. This is due to the fact that the neutrino luminosity is directly affected by the magnitude and the duration of the accretion phase [Bur88, Bur90],

$$L_\nu \propto \frac{GM}{R}\dot{M}. \tag{2.12}$$

All these characteristics in neutrino luminosities are very important features for a future detection to diagnostic the evolution of the shock.
Moreover it has to be emphasized, that during the shorter time of the accretion rate $\dot{M}$ of the prompt explosion, less mass is accumulated in the PNS. As a consequence, the released gravitational binding energy of the growing neutron star is smaller, which implies a smaller radiated total neutrino energy than by the delayed explosion ($E_{\nu(prompt)} < E_{\nu(delayed)}$).

2.6.3 The Second Slow Cooling Phase

The corresponding accretion rate assumed by Burrows [Bur88] is given by the formula $\dot{M}(t) = \dot{M}_0\, e^{-t/\tau}$, where the quantities $\dot{M}_0$ and τ depend upon the particular explosion mechanism. Several models have been computed to describe the characteristic behavior of the neutrino luminosity and the signal evolution of the core during the late phase [Bur88, Bur90]. Thus, the decrease of the neutrino luminosity must be very strong in the prompt mechanism due to the stopped accretion mass. Otherwise it must be softer, like in the case for a successful delayed mechanism.
The late phase is characterized basically by the long-term diffusive neutrino-cooling of the inner core. Here L_{ν_e} sinks to 10^{51} erg/sec, as depicted in Figs.2.12 and 2.13. The early short phase the neutrino luminosity follows an exponential decay ($\tau \gtrsim 4$ sec) during the first second, whereas for the following 20-40 sec it is better described with a power law (index $\sim 1 \pm 0.5$) [BKG92]. This long time behavior is a consequence of the high density and high neutrino energy in the inner part of the PNS, which is the main source of the thermal neutrino emission. The early fast phase and the later slow phase seem to be fundamental to define the generic characteristics of PNS cooling. In fact a clear luminosity smearing over many tens of seconds to a minute is expected for a Galactic collapse [BKG92], whereas for SN 1987A in the Large Magellanic Cloud, events were detected only within the first 10 sec. The end of the PNS cooling phase is defined by the moment, when the core becomes completely transparent to neutrinos, as indicated in Fig.2.12.
The possible formation of a black hole is a very interesting information which could be carried by the neutrino signature. As the PNS accumulates matter at very high mass accretion rate $\dot{M}$,

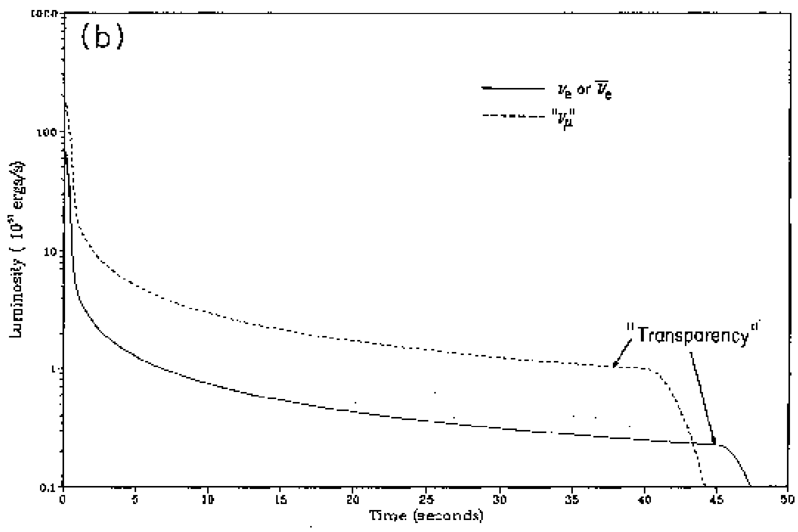

Figure 2.12: Time evolution of the luminosity for all neutrino species ν_e, $\bar{\nu}_e$ and "ν_μ'' during the first 50 seconds of the neutrino burst. It is clear to recognize the two phases of the PNS cooling. See text for further discussion. Picture from [BKG92].

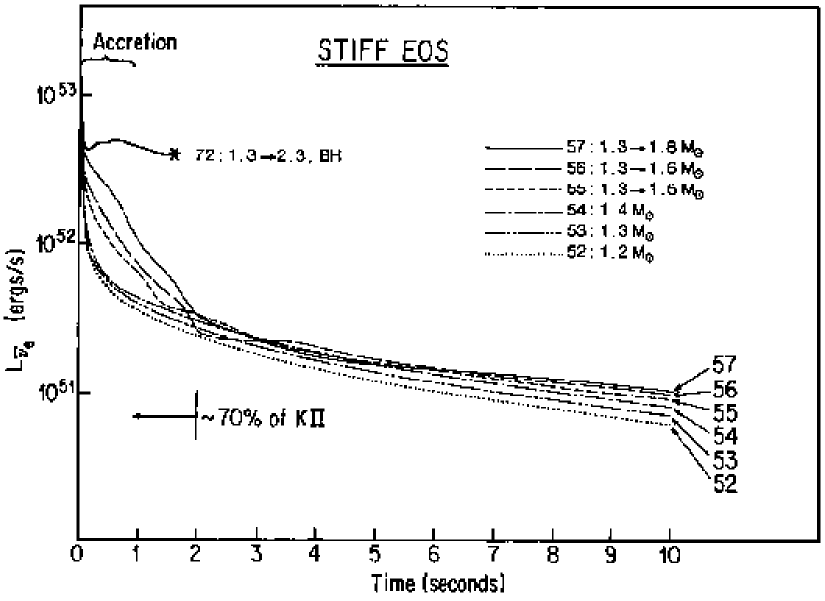

Figure 2.13: Antineutrino luminosity ($L_{\bar{\nu}_e}$) versus time in seconds. Models 52-57 end with a neutron star, and model 72 leads after $\sim$ 2 sec to a collapse into a black hole. Picture from [Bur88].

it becomes so dense that general relativistic effects must be taken into account. Due to the strong value of $\dot{M}$ during the accretion shock, core neutrino emission ceases immediately, after a general relativistic instability [Bur88]. Indeed, matter which has already collapsed into a black hole radiates neutrinos very inefficiently. What could be observed, is that a high neutrino luminosity is generated and then abruptly truncated after just 1 sec, which indicates a black hole formation. This very distinct neutrino signature is shown in Fig.2.13 (model 72 [Bur88]). If such a neutrino signature will be detected using underground neutrino telescopes, it would correspond to the detection of a stellar-mass black hole birth. However, since the Galactic supernova rate is estimated to be roughly the same of the Galactic neutron star formation [Bur88, Lon94], only a small fraction of collapses is expected to lead to a black hole.

2.7 Supernova 1987 A

On 24 February 1987, supernova 1987A was discovered in the Large Magellanic Cloud at an estimated distance of $\sim$ 52 kpc, by its optical observation. The spectrum showed hydrogen lines, so that it was classified as a Type II supernova. Since SN 1987A was regarded as a collapse driven supernova explosion, a detection of its neutrino burst by underground neutrino telescopes was expected. Indeed, before the optical discovery, Kamiokande II [Hir87] and IMB [Bio87] detectors had recorded 11 and 8 epochal events, respectively, on 23 February 1987, 7:35:35 UT. Two others detectors, the Mont-Blanc-Experiment (5 events) [AF87] and Baksan (5 events) [AAV87] reported also their detection of supernova neutrino events. However due to their time inconsistency, Mont-Blanc-events 4.5 hours earlier and Baksan 35 sec later, and to their low statistics [KZ97], they were not taken into account for the combined analysis.
Fig.2.14 shows the data taken by IMB and K II, which are represented as electron energy versus time. The electron energy refers to secondary electrons or positrons, which generated the Cherenkov light detected by phototubes inside the detectors. Although the observed signal is sta-

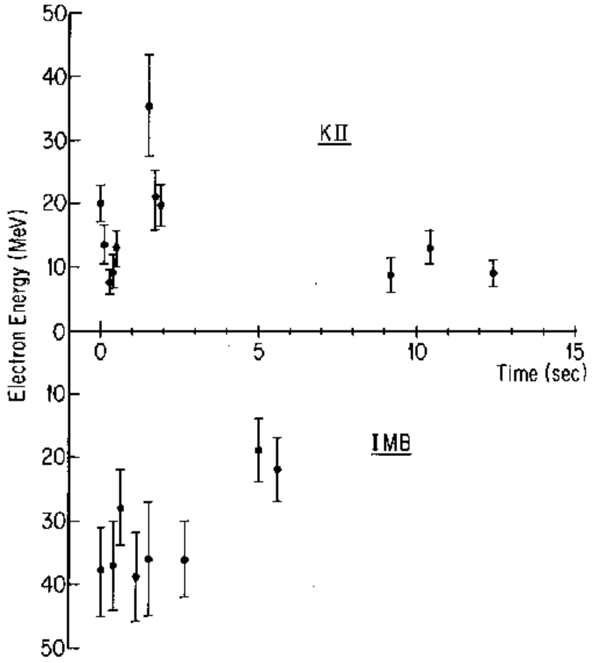

Figure 2.14: The 19 historical neutrino events from the Supernova 1987A, electron energy versus time. (Upper) 11 events detected by KII, (lower) the 8 ones by IMB. Picture from [Bur88].

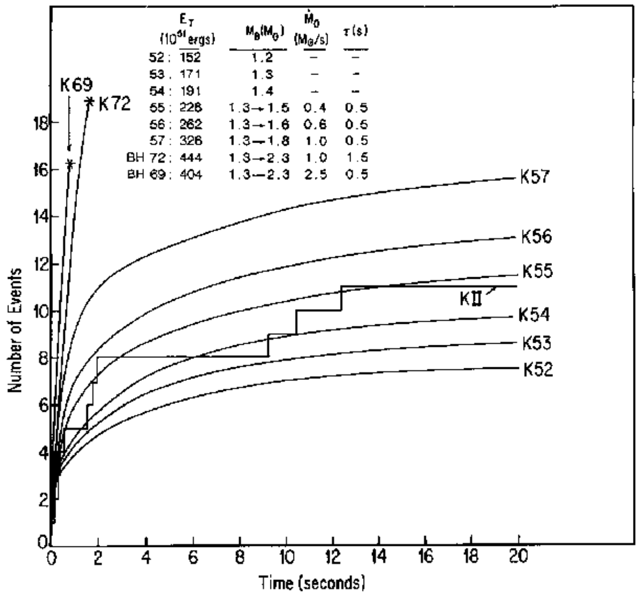

Figure 2.15: Theoretical predictions from different models computed by Burrows of the integrated number of $\bar{\nu}_e$ events recorded in KII. Notice that model K69 and K72 predicts a black hole formation. Picture from [Bur88].

tistically poor, an analysis was performed to prove theoretical models of the late phase. The signal expectation for models computed by Burrows [Bur88] is depicted in Fig.2.15. The two-phase nature of the protoneutron star cooling from the model prediction is quite well reproduced in the data.

2.8 Supernova Rate in the Milky Way

In order to estimate the supernova rate in our Galaxy, two sources are considered: (1) The supernova rate in other galaxies; (2) The few historical observed supernovae in the Milky Way. To estimate the supernova rate in external galaxies, a fiducial sample of 96 supernovae is used, subdivided and classified as follows: 11 Type Ia supernovae, which are assumed to come from white dwarfs, belonging to a old stellar population and 7 Type Ib and 78 Type II supernovae, which are assumed to come from gravitational stellar collapse of massive stars, belonging to young star population [TLS94].
The supernova rate is affected by several features, which must be taken into account: (1) The high central brightness of the galaxies which can obscure supernova detection, implies an increase of the supernova rate with the distance. (2) The supernova rate observed depends also on the inclination of spiral parent galaxies. (3) The supernova rate is expected to be proportional to the number of progenitor stars in a galaxy. (4) It depends further on the galaxy luminosity and its Hubble type. Our Galaxy is expected to be of type Sbc [TLS94].
From the five historical Galactic supernovae in the last millennium a global rate can be derived, using a detailed model of the Milky Way. A Galactic model consists of a thin stellar disk, which represents the young stellar population, and of a thick stellar disk as well as of a halo, which contains most of the old stars. Therefore it is expected, that supernovae Type II and Ib are located in the thin disk, while the Type Ia supernovae are thought to be located in the thick disk. Results from these considerations give an expectation of 39 Galactic supernovae in 1000 yr to explain the only five observed [TLS94].
Combining the results from all information of these two sources, one gets a rate of 2.5 ± 0.8 SNe per 100 yr, which means one galactic supernova per 40 ± 13 yr [TLS94]. Note that $\sim 85\%$ of these supernova come from massive stars, which are progenitors for Type II, Ib SNe. In other words, a Galactic neutrino burst is expected every 47 ± 15 yr, which means 2.1 ± 0.7 per century.

2.9 Interaction and Detection of Neutrinos

Neutrinos can interact with matter either via charge current (through the exchange of gauge bosons W^+, W^-), or via neutral current processes (through the propagation of the gauge bosons Z). Important reactions for detection of neutrinos are: (1) neutrino absorption; (2) neutrino electron scattering; (3) neutral current processes. From neutrino interactions information about their sources can be reconstructed. For instance, the shape of the recoil energy spectrum reflects the shape of the spectrum of neutrinos emitted by the source, or neutrino flavor information can be extracted from their different cross sections.

2.9.1 Neutrino Absorption

Absorption describes reactions in which an incoming neutrino (anti-neutrino) is absorbed, an electron (positron) is created and a neutron (proton) in the target nucleus is transformed into a proton (neutron). The cross section contains the information on the dynamics (the nuclear matrix element), which represents the neutron-proton transformation and the kinematics of the process (the phase space factor), which gives the number of available final states [HM84].
The absorption or neutrino capture reaction is symbolically represented as

$$\nu \; + \; {}^{Z-1}A \; \longrightarrow \; e^- \; + \; {}^{Z}A \tag{2.13}$$

where Z is the atomic number of the final nucleus, and A indicates the mass number [Bah89]. The corresponding cross section depends upon the energy and the momentum of the electron that is produced. Note that, due to momentum conservation, the nucleus recoil energy is small compared to the energy of the emitted lepton, which can be measured by detectors. The most important neutrino reaction for supernova detection in light-water Cherenkov detectors is the anti-neutrino absorption [Hax87, BKG92]

$$\bar{\nu}_e + p \longrightarrow n + e^+. \tag{2.14}$$

Its cross section with an average of $\sigma_\nu \sim 10^{-41}\mathrm{cm}^2$ for E_ν in the 10-30 MeV range [BKG92], represents the largest cross section in water, as depicted in Fig.2.16. Therefore light-water detectors are $\bar{\nu}_e$ filters with little neutral current sensitivity. In fact the contribution of the $\bar{\nu}_e$ response in such detectors compared to the neutrino-electron scattering and scattering off oxygen nuclei is: $\bar{\nu}_e p = 95.9\%$, $\nu_i e = 2.6\%$, $\nu_i\mathrm{O} = 1.5\%$, where ν_i indicates all neutrino and anti-neutrino flavors [BKG92].

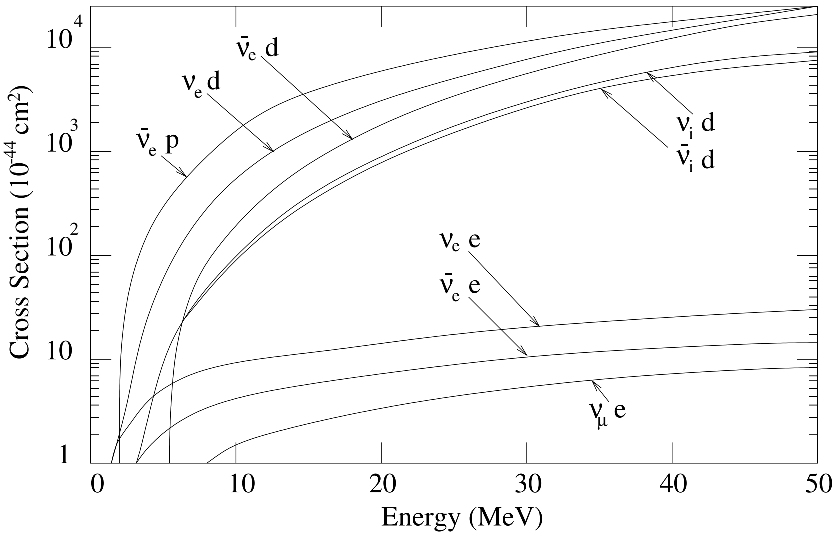

Figure 2.16: Neutrino cross sections in 10^{-44} cm^2 versus neutrino energy in MeV on proton, electron and deuterium target. The largest cross section in light-water detectors results from $\bar{\nu}_e p$, whereas for "ν_μ'' are dominant NC deuterium processes. Picture from [BKG92].

2.9.2 Neutrino-Electron Scattering

In neutrino-electron scattering

$$\nu_e \;+\; e^- \;\longrightarrow\; \nu_e \;+\; e^- \;, \tag{2.15}$$

the electrons are scattered forward in the direction, which connects the Earth and the source (e.g. supernovae, the Sun, other astronomic sources). The peaked angular distribution allows to determine whether neutrinos come from a supernova. The cross section can be described as a function of neutrino energy q approximately by $\sigma(q) = 9.2(q/10\ \mathrm{MeV}) \cdot 10^{-44}\mathrm{cm}^2$ [Bah89]. A recent calculation of the error of the νe^- forward scattering for Super-Kamiokande (SK) indicates an uncertainty in the angle of only $\delta\theta \simeq 5°$, i.e. $\delta(cos\theta) \simeq 4 \cdot 10^{-3}$ [BV99]. In addition, the measured recoil energy spectrum can be compared with the theoretical expectations and their consistency tested. The time resolution is of fundamental importance to diagnostic the two different cooling phases (see Sec.2.6.2 and Sec.2.6.3) of the protoneutron star [Bur90]. Unfortunately the very small cross section of ν_e makes its detection difficult.

2.9.3 Neutral Current Interactions

Neutral current interactions can yield information about both the solar neutrino problem and the cause of neutrino oscillations [Bah89]. However, neutral current processes are not sensitive to neutrino flavor. Neutrino-nucleus elastic scattering, which can be represented symbolically by the reaction

$$\nu + A \longrightarrow \nu + A \tag{2.16}$$

is an important neutral-current reaction, where A is a nucleus with N neutrons and Z protons. At low energies, relevant for supernova neutrinos $O(\mathrm{MeV})$, the nucleus can be considered as a point scatterer, all of whose nucleons respond coherently. The cross section of such reactions is proportional to N^2 , for $N = Z$, and amounts to $\sigma_\nu \sim 4 \cdot 10^{-43}\mathrm{cm}^2\ N^2(q/10\ \mathrm{MeV})^2$, where q is the incident neutrino energy [Bah89].
We noted previously the most energetic neutrinos from supernovae explosion are "ν_μ'', i.e. muon and tau neutrinos (anti-neutrinos). For the moment the only possibility to detect such neutrinos is through neutral current processes in heavy-water Cherenkov detectors. A detector example of present interest is the Sudbury Neutrino Observatory (SNO) constructed in Sudbury, Ontario. The detector consists of 1 kton of heavy water (D_2O) surrounded by a fiducial mass of 1.6 kton of light-water (H_2O) [BKG92]. In fact this detector is uniquely suited to detect "ν_μ'' neutrinos via NC reactions with deuterium:

$$\nu_i + d \longrightarrow n + p + \nu_i \tag{2.17}$$

Fig.2.16 also depicts the cross section versus neutrino energy for supernova neutrinos on a deuterium target, which presents roughly the same shape and order of magnitude the larger $\bar{\nu}_e p$ cross section. Furthermore the duplex nature of SNO can be used, as in the case of the SK detector, for pointing to a supernova through ν_e scattering, with an estimated angular resolution of $\delta\theta \backsimeq 20°$, i.e $\delta(cos\theta) \backsimeq 6 \cdot 10^{-2}$ [BV99].
To sum up, it is interesting to compare the total energy radiated by all neutrino species, during a supernova explosion: $\nu_e : \bar{\nu}_e :$"$\nu_\mu'' \mid 1.2 : 1 : 3$, with the contribution of each flavor to the total signal expected in water: $\nu_e : \bar{\nu}_e :$"$\nu_\mu'' \mid 2 : 40 : 1$ [Bur88, Bur98a]. Although the smaller energy is carried away from $\bar{\nu}_e$, the anti-neutrino absorption yields the most important contribution to the signal.

2.9.4 Cherenkov Radiation

In order to detect neutrinos they must interact with matter in the detector, so as to create secondary charged particles which can be detected. When a charged particle in a material moves faster than the speed of light in the medium, Cherenkov radiation is emitted. The speed of light in the medium is given as $\beta c = v = c/n$ [Leo94], where n is the index of refraction of the medium, where for ice $n = 1.32$ and c is the speed of light in vacuum.
The Cherenkov effect is generated through the polarization of the medium during the passage of the charged particle. The neighboring atoms around the particle trajectory become dipoles, which influence the dipole field of the medium. If $v_{particle} < c/n$, the dipoles remain symmetric around the particle track, so that no radiation is emitted. In the case of $v_{particle} > c/n$, the resulting dipole field, due to the coherent oscillation of the dipoles, is non-vanishing and the symmetry is broken producing the radiation [Gru93].

Thus, an electromagnetic shock wave is generated, which propagates behind the particle track. This coherent wave shock front is emitted at a well-defined angle in a cone shape. The angle is given by the formula:

$$cos\ \theta_C = \frac{1}{\beta \cdot n(\omega)} \tag{2.18}$$

Therefore the Cherenkov angle θ_C depends both on the speed of the particle and the frequency of the emitted radiation. Note that β must be greater than $1/n$, in order to get a meaningful physical value for the angle θ_C.
The number of photons emitted as a charge particle travels through the medium is important for Cherenkov detectors. The number of photons emitted per unit length in the sensitivity range of $\lambda_1 - \lambda_2$ is

$$\frac{dN}{dx} = 2\pi z^2 \alpha\ sin^2\theta_C \int_{\lambda_1}^{\lambda_2} \frac{d\lambda}{\lambda^2} \tag{2.19}$$

where the frequency dependence of n has been neglected over the limited sensitivity range of photo-multipliers (PMs). For typical PMs with a sensitivity range of 300-600 nm and $cos\theta_C = 0.75$ (water), about 200 photons per cm are emitted by a relativistic particle with $z = 1$.

3 The AMANDA Detector

3.1 Detector Description

The AMANDA detector is a neutrino telescope deployed deep in the Antarctic ice at the South Pole. It consists of a shallow array, AMANDA A, deployed in 1993/94 and a deep array AMANDA B consisting of 10 strings. The AMANDA B10 detector is a composite array, where the inner four strings form the original sub-detector AMANDA B4 (strings 1-4). Six outer strings (strings 5-10) surround the first four. Strings 1-4 were deployed at beginning of year 96, and strings 5-10 were added during the 96/97 season [And99]. In the mean time, 9 more strings have been added, the last 6 during the season 1999/2000.
The first four strings support 20 OMs except for the fourth string which holds 26 modules. Strings 5-10 have been deployed with 36 OMs per string. All OMs were installed facing down with the exception of a few modules at strings 1-4. In the deep ice holes were drilled up to a depth between 2000 and 2180 meters, in which the strings run from the ice surface to depths of 1900-2000 meters. The detector length is $\sim$ 480 m, from its top at $\sim$ 1520 m up to the bottom at $\sim$ 2000 m. A main cable starting at the top of the string contains 20 coaxial cables (strings 1-4) or 36 twisted-pair cables (string 5-10) which are bundled together inside a ‘supercable’. The purpose of these cables is both to supply the PMTs with the high voltage and to transmit the PMT pulse to the electronics located at the surface. Additional cables are deployed adjacently to the supercable holding optical fibers in order to emit diffuse light below each OM. The aim of their installation is to calibrate the PMTs through a photon source. Extra cables enclosed inside the supercable were needed for PMT time calibration, study of the optical parameter of the ice and measurement of pressure and temperature. At shallow depth two radio receivers from RICE (Radio Ice Cherenkov Experiment) were also buried for feasibility studies of the radio tail of the Cherenkov light emitted by particle showers.

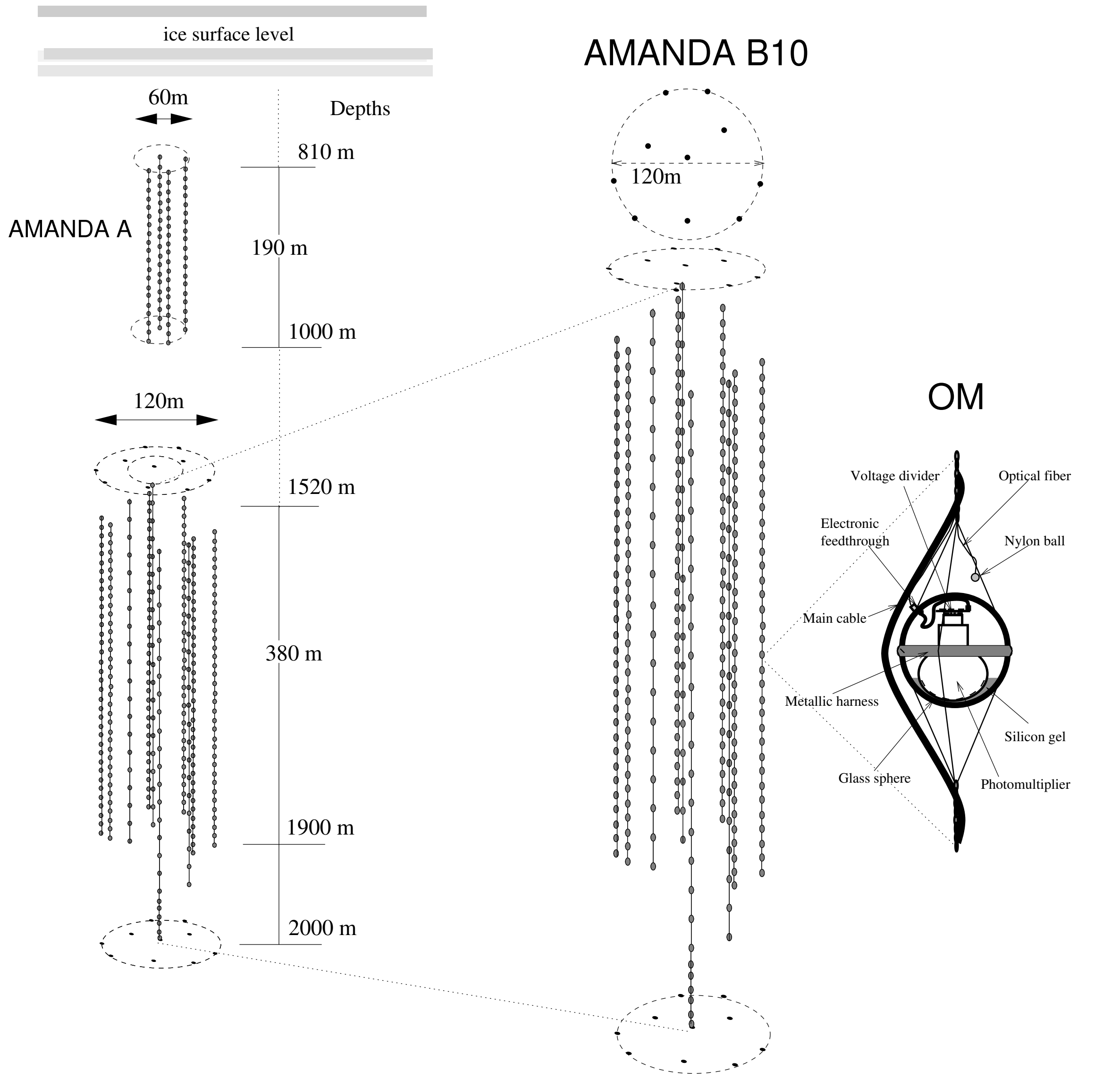

Figure 3.17: Schematic representation of AMANDA A and AMANDA-B10 arrays, true scaling.

AMANDA-A was deployed in four strings each with 20 OMs at a depth between 800 and 1000 m. For AMANDA-A a supernova analysis was done with a total number of 60 PMTs for a selected live-time of 81.9 days [Wis95, Bir97].

3.1.1 AMANDA B4

The four strings of the AMANDA B4 sub-detector were equipped with 20 8-inch PMTs from Hamamatsu at a vertical spacing of 20 meters. The strings are deployed with a spacing of $30 - 40$ meters. All PMTs are facing down with the exception of PMTs # 1, 10 (string 1-3), and # 1, 2, 10, 19, 20 (string 4). For SN analysis the orientation of an OM does not play any role (see Sec.5.3). Additional components deployed together with the strings in order to calibrate the OMs and to investigate the optical properties of the ice include a nitrogen laser, 3 DC halogen lamps and LED beacons.

3.1.2 AMANDA B10

During the 96/97 season 6 strings of 36 OMs surrounding the four strings of AMANDA B4 were deployed on a circle with 60 m radius (Fig.3.17). The OMs were constructed with the same PMTs as in AMANDA B4, which are all facing down with a shorter vertical spacing of 10 meters, so each string spans a length of $\sim$ 350 m. For the high voltage connection and the transmission of the PMT pulse a twisted pair cable was adopted instead of the coaxial cable used in AMANDA B4. The main advantages using such a cable are the better timing characteristics, better rejection of common mode noise, less attenuation and their thinness allowing to deploy a larger number of PMTs per string.
Additional calibration components include a second brighter N_2-laser, and a transmissometer at a depth of $\sim$ 1800 m to measure the attenuation length in the range of 660 nm inside the re-freezing ice of the hole.

3.2 Deployment

AMANDA is located at the Amundsen-Scott base at the South Pole, where access is possible only during the Austral Summer end-October until mid-February (Fig.3.18). The ice sheet at the South Pole is $\sim$ 3000 m thick, in which holes are drilled up to a depth of $\sim$ 2000 m with a typical diameter of 60 cm, large enough for OMs with a diameter of 30 cm. A mechanical drilling of the ice column would be very expensive and difficult, so a hot-water drill is adopted to drill deep holes. The drill mechanism consists of a drill head, which pumps 80° hot water melting the ice with a speed of $\sim$ 1 cm/sec. Roughly three and a half days are necessary to drill a hole. The deployment of a string follows immediately, since a time limit of $\sim$ 35-40 hours is set by the re-freezing of the hole.

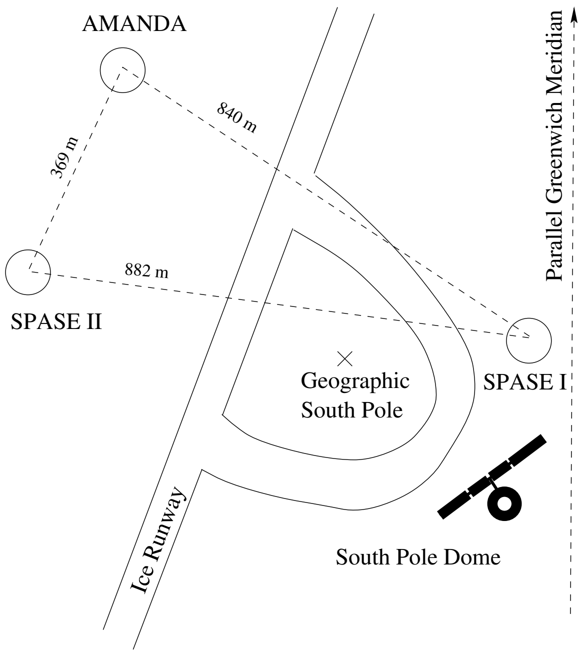

Figure 3.18: Overview of the Amundsen-Scott base together with AMANDA and the air shower detectors SPASE I and SPASE II.

3.3 Optical Modules

An optical module is essentially composed by a photo-multiplier enclosed in a pressure-tight sphere of thick glass. The used PMT is an 8-inch Hamamatsu R5912-02 with 14 stages of diameter 20 cm as shown in Fig.3.19 (left). This PMT is a special development in order to achieve a gain of 10^9 for a PMT pulse, which must be transmitted through more than 2000 m of cable without further amplification. In order to reach a high efficiency and a good time resolution the electron is focused through grids before it passes through the 14 dynode stages [Bou98]. The range of the sensitivity of their bialkali photocathode is 300-650 nm, with a peak quantum efficiency of $\sim 23\%$ at 420 nm, as depicted in Fig.3.19 (right). In spite of its large photocathode, the optimized Hamamatsu PMT for AMANDA, has a good time resolution of $\sim$ 3-5 nsec FWHM.

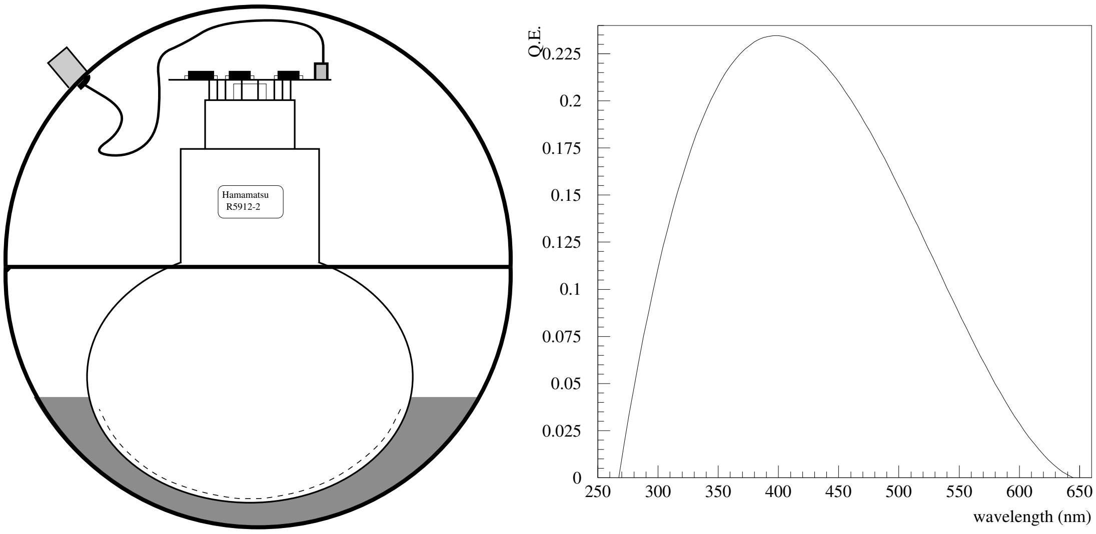

Figure 3.19: (Left) Sketch of the optical module deployed in AMANDA-B10. (Right) Quantum efficiency as a function of wavelength for PMTs adopted in AMANDA.

Another important feature of AMANDA PMTs is their low noise rate. The absence of bioluminescence and radioactive decay of potassium reduces the dark noise rate by more than two orders of magnitude compared with that measured in the ocean [Pry88]. In order to understand the behavior of the PMT dark noise rate at deep temperatures, PMTs were tested in the laboratory within a light-isolated refrigerator [Hun99]. Fig.3.20 (left) shows the noise rate versus temperature. As expected, the noise rate decreases with the temperature up to $\sim 0^\circ$ and subsequently after a plateau around $\sim -10^\circ$ increases again up to the end point at -50°. This effect was explained with a related increase of the amplification with respect to the room temperature which corresponds to a ratio of $A_{-50^\circ}/A_{20^\circ} = 1.2 \pm 0.13$ [Hun99]. The measurement showed that the PMTs are adequate to operate also in extreme conditions at -30° without disturbances or changes of their characteristics. In the laboratory the influences of the pre-pulsing and the after-pulsing were also studied with short cables. Fig.3.20 (right) depicts the afterpulse behavior of a PMT, which presents two dominant peaks at ~ 2 μsec and at ~ 7 μsec respectively. The resulting measured contamination of the dark noise pulse due to the afterpulse has an effect between 5% and 30% as shown in Fig.3.21 (left). As will be described below, the SN data are taken with a programmable afterpulse suppression (APS) dead time which shows a reduction of ~ 25 % in noise rate compared with muon data without APS (see Sec.7.5). The noise rate measured in situ for SN data lies between 0.3-0.4 kHz and 1.1-1.2 kHz for strings 1-4 OMs and strings 5-10 respectively (see par.7.3.2). We will see

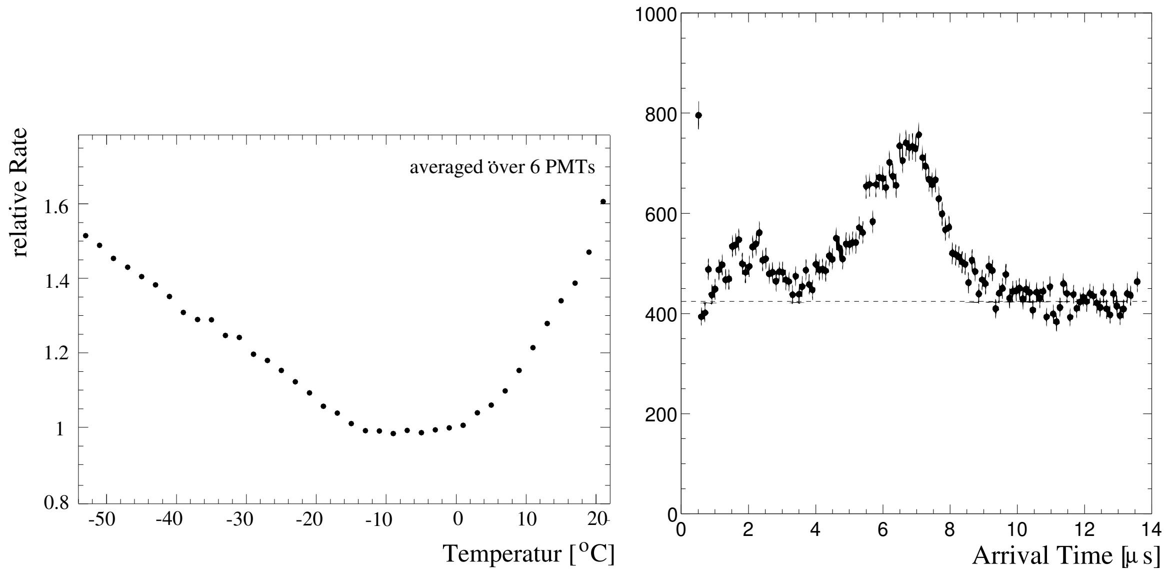

Figure 3.20: Noise rate relative to 0° as a function of temperature measured in the laboratory (left). Distribution of the arrival time due to the effect of the afterpulse. Two distinct afterpulses can be seen around 2 and 7 μsec, respectively, also measured in the laboratory (right) [Hun99].

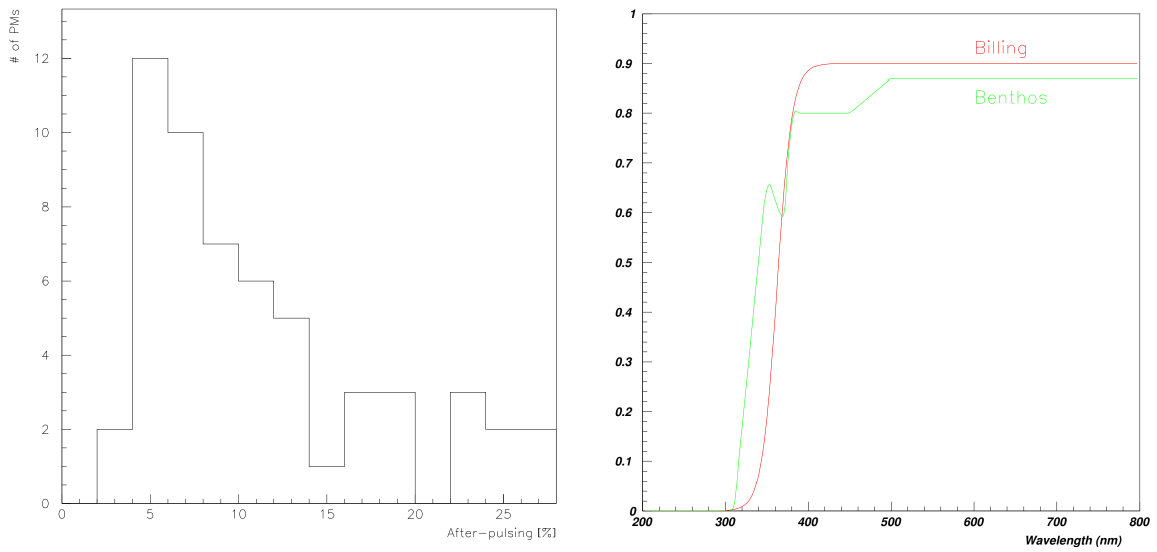

Figure 3.21: (Left) Distribution of the after-pulsing effects in percentage to the pure dark noise pulse. (Right) Transmissivity of the two different glass spheres adopted in strings 1-4 (Billings) and in strings 5-10 (Benthos).

that the main difference of the noise rate values between the strings 1-4 and strings 5-10 PMTs is due to the different glass spheres. The PMTs of strings 1-4 were put in spheres of 9 mm glass from Billings. Although such spheres have worse transparency than that from OMs of strings 5-10, which are enclosed in Benthos spheres, they contain nearly no contamination of ^{40}K. This radioactive isotope is responsible for the noise rate excess by a factor four of the Benthos compared to the Billings sphere. Fig.3.21 (right) depicts the transmissivity of both the Billings and Benthos sphere. It is clear that the Billing transmissivity is 90% from 400 nm and then drops suddenly to

zero around 350 nm where the PMTs are still sensitive, while the transmission edge of the Benthos glass is 50 nm longer.
To ensure both a mechanical and an optical contact, an optical silicon gel was put inside the sphere between the PMT and the internal glass surface (see Fig.3.19). The base card circuit for the high voltage distribution is also contained in the sphere, but all additional electrical component (amplifiers, discriminators, ADC, TDC,...) are located 2000 m far away at the ice surface.

4 Optical Properties of South Pole Ice

In order to study the optical properties of the glacier ice, various light calibrations sources have been deployed at different depth (see Sec.3.1.1). This investigation helps to answer two important questions.
(1) At which depth will disappear air bubbles trapped in the ice, which are responsible for the decrease of the scattering length?
(2) In which depth range is the clearest ice stratum, ideal for a $1\mathrm{km}^3$ high-energy neutrino telescope located?
In order to calculate analytically the optical parameter of the ice, the time distribution of an isotropic light source (i.e. the Green's function for an isotropic light source) can be defined as follows, if is known the probability for a photon to reach the photocathode at distance d after N scatters [Ask95]:

$$f(d,t) = \frac{1}{(4\pi D t)^{3/2}} \exp^{-\frac{d^2}{4Dt}} \exp^{\frac{c_i t}{\lambda_a}} \tag{4.20}$$

where $D = c_i \lambda_{eff}/3$, λ_a is the absorption length, c_i, a proportional factor, $\lambda_{eff} = \lambda_{scatt}/(1 - \langle cos\theta \rangle)$ is the scattering length and $\langle cos\theta \rangle$ represents the average cosine of the scattering angle which is supposed to be ~ 0.8 in deep ice [RW97].
Measurements *in situ* of the time-of-light have been made with several optical fiber emitters in order to detect the light by OMs located at different depths in the ice. Fitting the data with the function Eq.4.20, an estimate of the parameters λ_a and λ_{eff} can be obtained, yielding $\lambda_a(515\mathrm{nm}) = 59 \pm 1(stat) \pm 3(syst)$ m and λ_{scatt} in the range 12.5-25 cm. These measurements were taken with the AMANDA-A array at depth between 810 and 1000 m, where air bubbles are present. However the scattering length increases with depth. This can be seen studying the arrival time distribution for AMANDA-A and AMANDA-B at a depth between 1520 and 2000 m (see Fig.4.22). The AMANDA-A histogram is much broader due to scattering by air bubbles, while at depth $\sim$ 1400 m [Wos99] the bubbles disappear, as demonstrated by the AMANDA-B peak with much smaller width.
For AMANDA-B, Eq.4.20 could not be used because of the longer scattering length at this depth, instead simulated time distributions were used to fit the parameters to the data. The length which characterizes the decrease of the photon flux as a function of the distance is called attenuation length λ_{att}. It can be derived from the photon flux at distance d integrating Eq.4.20 over time

$$F(d) = \frac{N_0}{16\pi\lambda_{eff} d} \exp^{-\sqrt{\frac{3}{\lambda_a \lambda_{eff}}} d} \qquad \text{where} \qquad \lambda_{att} = \sqrt{\frac{\lambda_a \lambda_{eff}}{3}} \tag{4.21}$$

and N_0 are the number of photons assuming an isotropic source. The results from all combined analyses yield [Low96]: $\lambda_a = 95 \pm 5$ m at 337 nm and 90-120 m at 350-480 nm; $\lambda_{eff} = 24 \pm 2$ m; which gives λ_{att} of 27-30 m.

A recent analysis [Wos99] summarizes the measurements for the optical properties discussed in terms of the absorption coefficient $a = 1/\lambda_a$ and of the effective scattering coefficient b_e/λ_{eff}, and their theoretical prediction by the He-Price model (see Fig.4.23). The peaks in scattering length are expected to be produced due to an extended presence of a thick dust band at depth > 1400 m [Wos99].

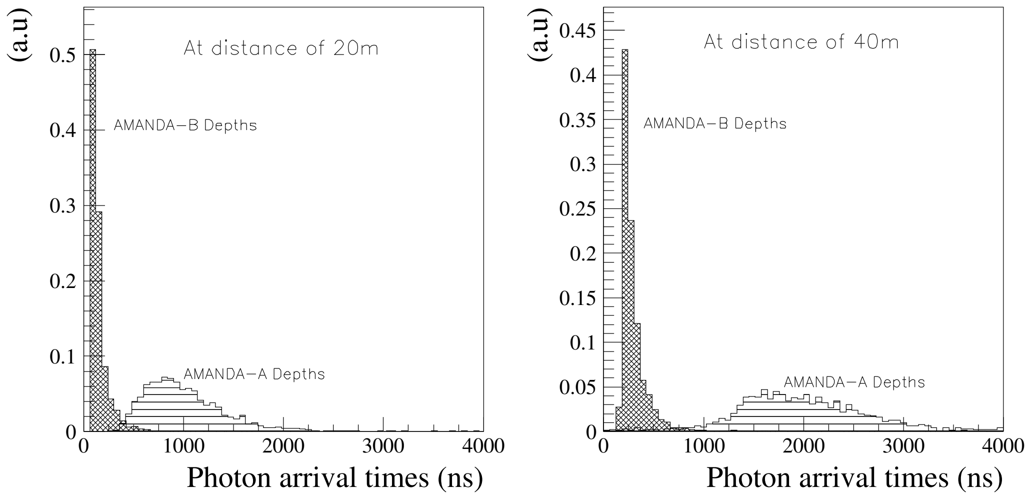

Figure 4.22: Arrival time distributions at 20 m and 40 m separation between light sources and OMs. Black histogram: AMANDA-B, hatched histogram AMANDA-A. Pictures from [Til97]

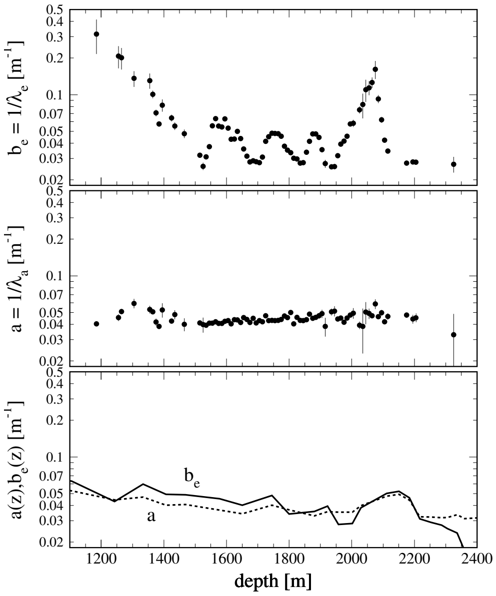

Figure 4.23: (Upper) The coefficients a and b_e from the data and (lower) their prediction by He-Price model as a function of depth. Pictures from [Wos99]

5 AMANDA as a Galactic Supernova Watch

5.1 Introduction

It was shown in the previous chapter that most of the released gravitational binding energy of a young neutron star is carried away by all neutrino species with a thermal spectrum of a typical temperature $\sim 2-4$ MeV in a time scale of $\sim$ 10 sec. Since the $\bar{\nu}_e$ cross section on protons in light-water Cherenkov detectors is significantly larger than the cross section for the other neutrino flavors, $\bar{\nu}_e$ is dominant for the supernova signal.
In the reaction of Eq.2.14, the positrons are emitted with a random orientation with respect to the initial neutrino direction, and with an energy close to that of the $\bar{\nu}_e$. Considering a thermal spectrum of temperature of $\sim$ 4 MeV, and taking into account that the inverse $\beta-$ decay cross section increases with the square of the neutrino energy, the positron energy distribution observed is expected to peak at $\sim 10-20$ MeV [HJZ94].

5.2 SN Detection with High Energy Neutrino Telescopes

High energy neutrino telescopes are constructed in a clear medium (water or ice), where the Cherenkov light created by charged particles is detected by optical modules (OM). Such telescopes are designed to search for long-range high energy muons with a typical threshold energy of several GeV, which is too high to observe supernova neutrinos of $O(\mathrm{MeV})$.
However there is a possibility to detect supernova neutrinos with large neutrino telescopes. The large flux of $\bar{\nu}_e$ produces a large number of positrons of energy $10-20$ MeV. During the typical burst duration of $\sim$ 10 sec, the resulting Cherenkov-light will give many signals in all optical modules. Although the signals of a single OM will be statistically not significant on the background of the thermal noise, it can be significant considering the collective contribution for a large number of OMs [HJZ96].
Through the summed excess signal, such telescopes can yield the time profile and a rough estimate of the distance, but cannot reconstruct any energy, direction or neutrino species, as some other Supernova detectors can.
The OMs of AMANDA have been deployed in the sterile Antarctic ice. The background is lower by a factor 10^{-2} [Pry88] than in ocean water Cherenkov detectors, due to the absence of bioluminescence and radioactive decay of potassium in ice. This of course plays a crucial role for Supernova detection via counting rate excesses. Furthermore, measurements of the absorption length of light, λ_{abs}, for deep South Pole ice show an unexpected large value of $\sim$ 100 m for the 350-400 nm frequency range, where the phototubes are most sensitive. The value of λ_{abs} is of fundamental importance for SN detection, since the effective detector volume V_{eff} depends linearly on λ_{abs} [HJZ94].

5.3 The Effective Volume of an AMANDA OM

The track-length of 20 MeV positrons in ice is $O(10\mathrm{cm})$, from which roughly 3000 Cherenkov photons are emitted. Fig.5.24 depicts symbolically positron showers created by $\bar{\nu}_e$ interactions in the AMANDA detector. Assuming a quantum efficiency of 20 % , the number of detectable photons would be of the order $N_\gamma \approx 600$. However, the probability that an OM could detect a photon of

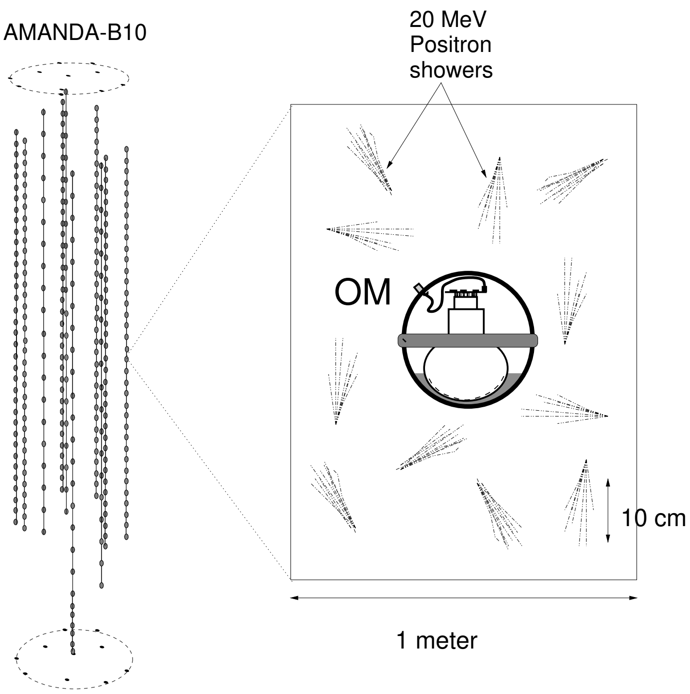

Figure 5.24: Expected positron shower by $\bar{\nu}_e$ interactions off protons within the AMANDA detector

the N_γ at large distance falls with the square of R

$$P(R) \approx \left(\frac{R_d}{R}\right)^2 \qquad for \;\; R \gg R_d \tag{5.22}$$

where R and R_d are the distance to the positron shower and the distance where the probability becomes unity. The effective area for the detection is

$$\pi R_d^2 \approx N_\gamma A \tag{5.23}$$

which is proportional to the detectable number of photons and to the collection area $A = 0.028\,\mathrm{m}^2$ corresponding to a typical OM of the AMANDA detector. Integrating the probability function $P(R)$ over volume, the effective volume can be calculated

$$\int_{R_d}^{\lambda_{abs}} P(R)R^2 dR \approx \frac{1}{\pi} N_\gamma A \lambda_{abs} \tag{5.24}$$

for $\lambda_{abs} \gg R_d$. So the effective volume for Supernova positrons corresponding to each OM is proportional to both the collection area of the OM and the absorption length of the light λ_{abs}.
A more complete and rigorous treatment to determine the effective volume for Supernova positrons was studied with a Monte Carlo simulation [Jac96]. Four different cases have been considered as input parameters for the simulation: models with and without scattering of the photons in ice, and two different estimated absorption lengths ($\lambda_{abs} = 90, 310$ meters). Since recent measurements of the absorption length in deep ice yield an estimation of $\lambda_{abs} \sim 95$ m, the model (HG-90) with *Henyey Greenstein* scattering and peak absorption length of 90 meters was considered which yields an expected effective volume per OM of $V_{eff} \sim 414\ \mathrm{m}^3$ [Jac96].

5.4 Expected Neutrino Signature in AMANDA

Using the 11 events from SN 1987A observed by the Kamiokande detector, a neutrino signature can be estimated for AMANDA at a given distance, rescaling the results of Kamiokande. For that, the ratio of the effective volumes of both experiments is necessary. From the 11 events observed by Kamiokande with a volume $V_{Kam} = 2140\ \mathrm{m}^3$ one can predict the excess in the number of photo-electrons (pe) in the whole array AMANDA as

$$N_{1\mathrm{pe}} = 11\ N_{OM} \left(\frac{\rho \cdot V_{eff}}{f \cdot V_{Kam}}\right)\left(\frac{52\ \mathrm{kpc}}{d}\right)^2 \tag{5.25}$$

where ρ, N_{OM} and d are the density of ice ($\rho = 0.924\ \mathrm{g/cm}^3$), the total number of the optical modules and the distance from the supernova to the Earth respectively [HJZ96, Jac96]. The factor $f = 0.8$ has to be considered for Kamiokande, since its instrument has an energy threshold, whereas AMANDA is a pure counting detector collecting photons from all positron showers. So considering the effective volume of $V_{eff} \sim 414\ \mathrm{m}^3$, one would expect a total number of events $N_{1\mathrm{pe}} \approx 100$ per OM for a supernova like SN 1987A close to the Galactic center (~ 8 kpc) within a 10 sec time interval.

For AMANDA the supernova signal detection must be performed taking into account the presence of the background counting rate of all phototubes. The measured average noise rate per OM is ~ 300 Hz and ~ 1100 Hz for strings 1-4 and for strings 5-10, respectively. Over 10 sec duration of the neutrino burst, the RMS-fluctuation of the noise from all OMs is expected to be

$$\sigma_{RMS} = \sqrt{10\ \mathrm{sec}\ R_{back}\ N_{OM}} \tag{5.26}$$

where R_{back} is the average of the counting rate in a single OM [HJZ94]. This is the expectation assuming Poisson statistics of the behavior of the counting rate distribution. However, as discussed below, the counting rate of individual OMs in AMANDA detector does not follow Poisson statistics. It shows a broader standard deviation by a factor ~ 1.6 and ~ 1.8 for strings 1-4 and 5-10 respectively [Wis95, Bir97], (see Sec.7.4.1).

6 SNMP System

6.1 SNMP Electronics

The SNMP (SuperNova & MonoPole) electronics was originally intended to record rate excesses on the μsec scale due to the passage of slow magnetic monopoles, and on the sec scale due to supernova occurrences. The SNMP system was the first hardware development of the DESY-group for AMANDA [Bir97], installed in 1994/95. This electronics resolves PMT pulses separated from each other by more than 100 nanoseconds [Tho]. Fig.6.25 depicts schematically the structure of the SNMP electronics, which represents a system completely independent from the main AMANDA DAQ.

PMTs operate at 10^9 gain, the signal amplification and the high voltage supply are performed by the SWedish AMPlifier modules (SWAMP). The discriminators are LeCroy 4413 and 3412E, converting the analog input pulse into digital ECL pulses. The high voltage is set for each individual PMT to achieve a peak amplitude of 1-pe signal pulse of ~ 400 mV and ~ 500 mV (for strings 1-4 and strings 5-10 PMTs, respectively).

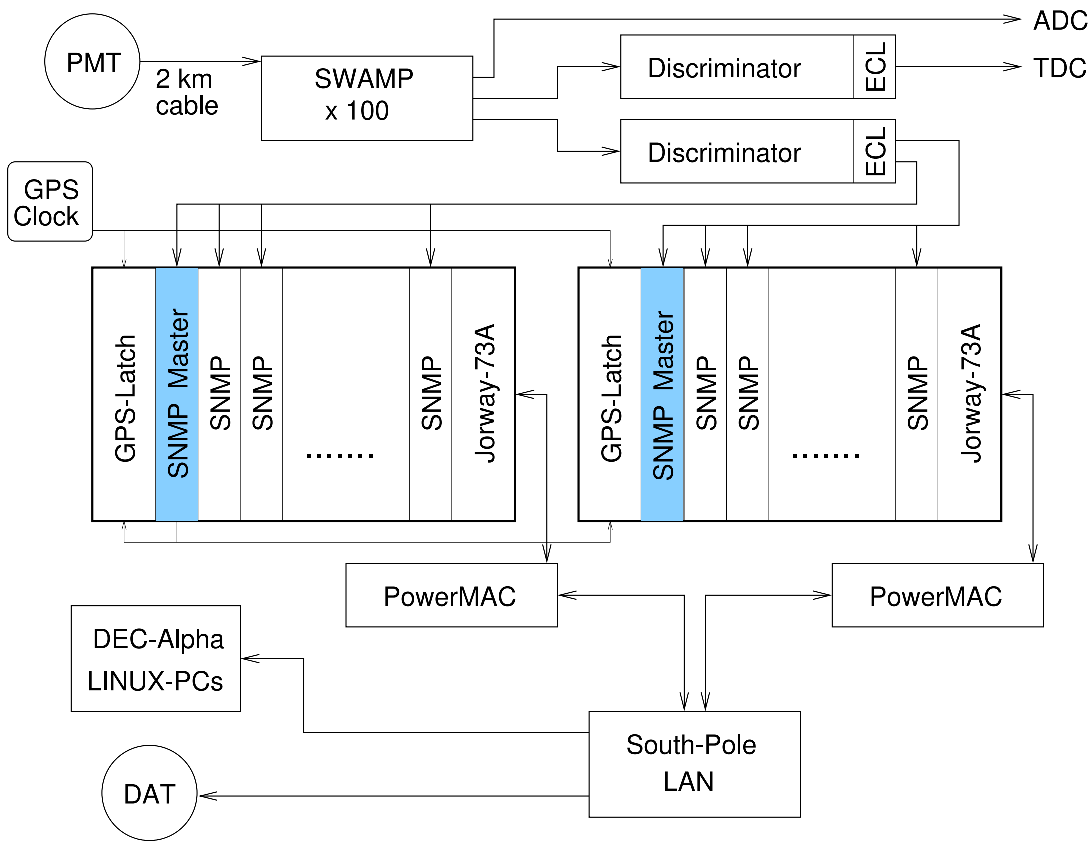

Figure 6.25: Schematic representation of the SNMP system. The SWAMP modules are DC-blocking linear high pass filters in the frequency range 0.1 MHz-10 MHz [Bou98]. The signal is split into two independent amplifiers with amplification range (x20-x200). One is set to x100, which represents the pulse input to the TDC (muon-electronics) and to SNMP-electronics, and the other is set to x25 and sent to the the ADC (muon-electronics). See text for further discussion.

6.2 SNMP Triggerboard

A full CAMAC crate contains 22 SNMP boards, corresponding to a maximal number of 352 channels (Fig.6.25). A SNMP board receives the leading edges of the discriminator outputs from a total of 16 channels. A schematic representation of a SNMP CAMAC board is shown in Fig.6.26. Each module contains [Tho]:

1. Four ECL-TTL level converters (L.C.)
2. One Field Programmable Logic Array (FPLA) XC 3164A with a digital monoflop deadtime circuit
3. Four FPLAs with the trigger logic (2 SuperNova & 2 MonoPole)
4. One (16k x 16 bit) data FIFO
5. One FPLA for the CAMAC and FIFO control

The ECL input signals are converted into TTL-level and transmitted to a digital monoflop circuit. All asynchronously arriving pulses are distributed with a defined timing information with a single 10 MHz master system clock. This internal clock is generated inside the SNMP master module (see Fig.6.25), and serially distributed through a twisted pair bus over all remaining 21 SNMP modules [Tho96]. The first FPLA converts the incoming asynchronous pulse to an output pulse of a minimal duration of 100 nanoseconds. To get an absolute timing information of each pulse, a CAMAC-GPS latch interfaced to the SNMP master clock is connected with a central GPS clock.

6.2.1 Afterpulse Suppression

The digital monoflop serves also as programmable deadtime circuit for PMT afterpulse suppression. The main idea is to pass the synchronized incoming pulses to the Supernova counters (in 2 groups of 8 signals) through individual gates which, immediately after the first input pulse, divert the information to the monoflop. The monoflop circuit itself is programmable for time intervals of a minimum of 100 nanoseconds up to a maximum of 12.8 μsec in single steps of 100 nsec. Since each CAMAC SNMP module receives the input pulse of 16 channels, the dead time interval will be the same for all 16 channels [Tho].

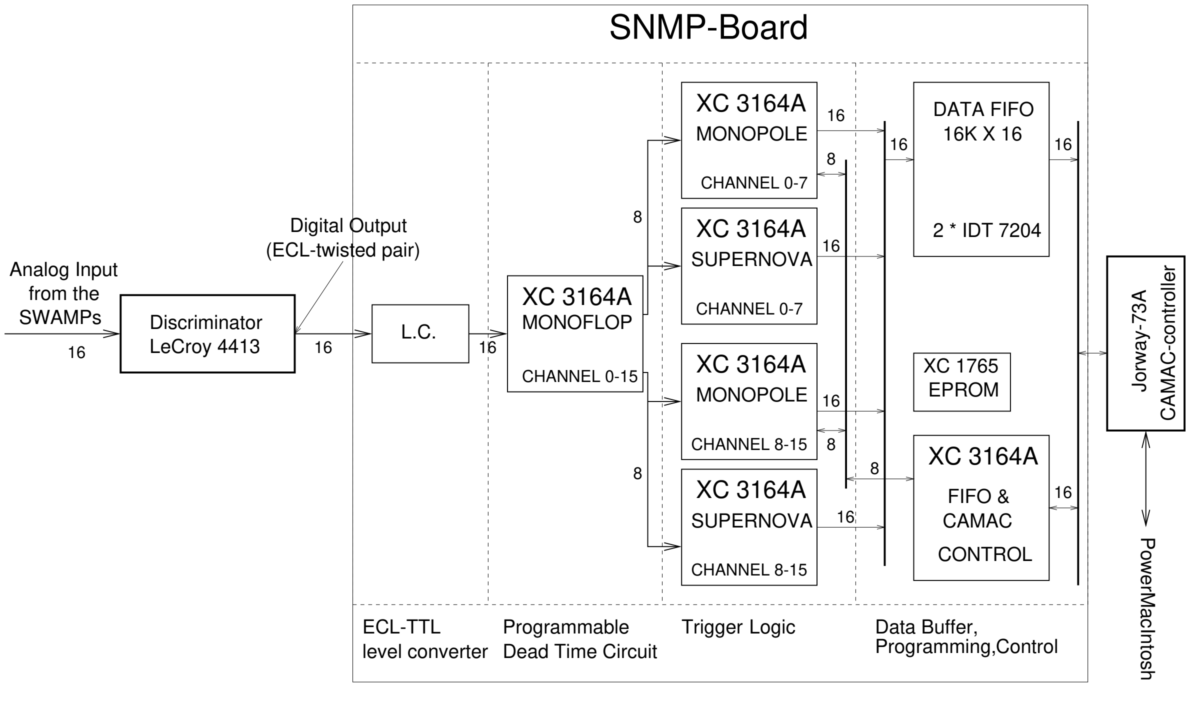

Figure 6.26: Sketch of the internal electronics of a SNMP module. It consists essentially of programmable logic arrays, which serve both for afterpulse suppression and trigger logic. The internal CAMAC & FIFO control is handled through an extra chip. The readout to the 16k x 16 bit FIFO (IDT 7204) data output buffer is decided by an interrupt signal from each of the individual SN counters. The FIFO control transfers the FIFO content to the CAMAC backplane via the Jorway-73A readout controller.

6.2.2 Supernova Trigger Logic

The aim is to measure permanently the counting rate of all channels. The incoming pulses are sent to the SN counter, which determines the counting rate in all PMTs in fixed time intervals of 500 msec. The output pulses of 16 channels from the gates are subdivided in 2 groups of 8 channels, which are distributed to the SN counter. Each counter records the arrival pulse within 500 msec in a 'prior' register set, and subsequently transfers the information into a shadow register set. The information of each counter is then transfered to the data FIFO. A continuous counting of the incoming pulses is done with the only possible loss of 300 nanoseconds which can be due to three factors [Tho96]: (1) 100 nsec of the transient dump interval due to the asynchronous nature of the input pulses. (2) 100 nsec of transfer time to write into the shadow register set. (3) 100 nsec for the read out and reset time of the counters.

6.3 SNMP DAQ

The output data structure set to data word of 16 bit length are sent to the Jorway CAMAC controller interfaced with the SNMP board. SN data are sent with a rate of 16 datawords per 500 msec. The output signals of all 22 SNMP boards (302 channels) are distributed to the Jorway controller, and a LAM (look at me) signal from the FIFO control can be sent for the readout. Both the GPS time and the counting rate information in 500 msec intervals are directly sent to Power-MacIntoshs, where a SNMP DAQ algorithm stores the data. In the Power-MacIntoshs the features of the data are checked and only meaningful data are written into binary files. The data are sent via the South Pole LAN to the AMANDA DEC-Alphas and Linux-PCs, where a first off-line treatment can be performed, and written to DAT-tape storage (150 MB/day). The full set of SNMP data together with the muon data are shipped back to the home institutes at the end of the Antarctic Winter.

7 Data

First data from the SNMP system has been obtained for AMANDA-A. A SN analysis for AMANDA-A (over the years 1995 and 1996) have been performed [HSTW94, Bir97]. For that analysis, about 60 PMTs behaving acceptably stable during 20 selected files were used.
In this work the SN analysis of AMANDA-B10 (strings 1-10) is presented. In this analysis more refined methods have been developed: a moving average subtraction and a maximum-likelihood method, which are central for the present work.
The data analyzed here, were taken during the seasons of Austral Winter of the years 97 and 98 at the South Pole. The size of each of the 8000 files is roughly $\sim$ 3MB which amounts to $\sim$ 24GB per year. This total amount of data for a whole year is more or less the same for the data sample 97 and 98.
Compressed SNMP data can be transfered via satellite with a rate of 3 MB per day [Bir97]. Raw data coming from the SN DAQ are translated by a reader [Wis97] into HBOOK files [Cou95, Bun95] where the information of 25 binary raw files is merged. The HBOOK files contain the information of counting rates in 10 sec intervals for each individual PMT and an additional summed counting rate for the whole array in 0.5 sec intervals. Part of these HBOOK files are sent via satellite with a current time coverage of $\sim$ 50% due to the overlapping of the geosynchronous visibility of different satellites.

7.1 Time Information and Run Statistics

Since AMANDA can provide only time information about the supernova event, it is important to get a good time resolution. The current off-line SN analysis was computed with fixed 10 sec time bin. Hereafter the individual time bins will be referred to as “events”.
A future upgrade of the SN DAQ should improve the time resolution to the order of several msec, perhaps giving the possibility to diagnostic the evolution of the supernova explosion.

The information about the whole run is saved in an additional log file. The run start is recorded in year, month, day and down to a second. Furthermore two different times with a precision of one second are compared: (1) the time from the GPS clock, and (2) the time from a local clock of a DAQ-host machine. For each single raw file it gives the start time indicating the beginning of the file. If for some reasons the run is interrupted, the crash-time and the total size of the complete run are also reported.
Of course, the length of the run is varying in time. Fig.7.27 shows the run evolution versus time for the years 97 and 98. The smaller number of runs in 98 (43 runs) illustrates that runs in 98 have been longer than runs in 97 (83 runs). Nevertheless, the run profile of the two years shows the same shape without sudden jumps or drops, which suggests a linear behavior of the run evolution as a function of time.

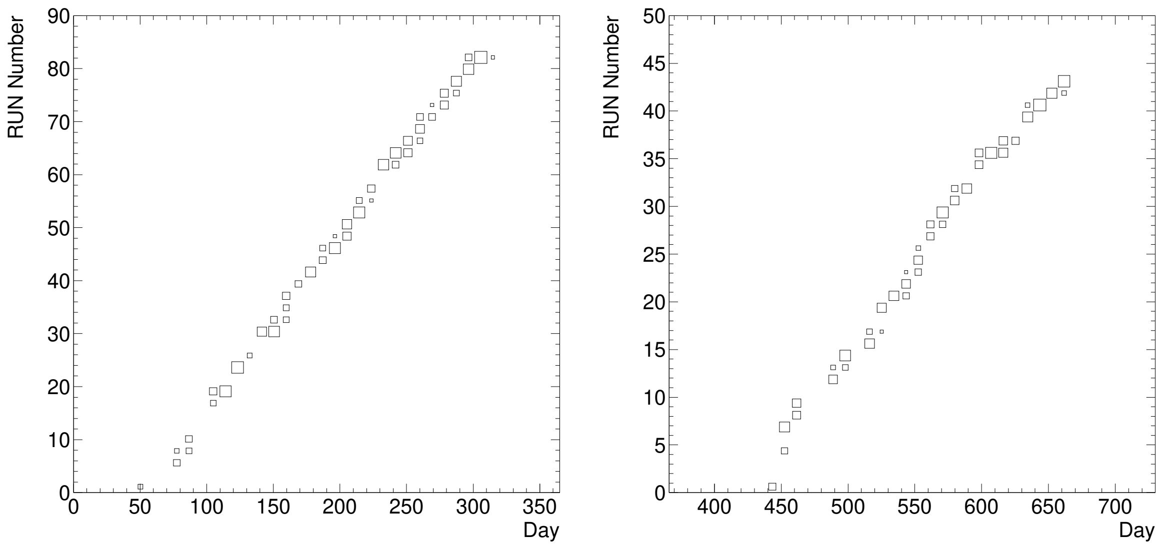

Figure 7.27: Profile of the run number as a function of time (day), left for 97 data and right 98 data.

7.2 Quality of Data

To study the statistical features of the SN data and to understand their behavior a *Statistics* program was developed, which produces a large Ntuple enclosed in HBOOK files. The quality of the SN data depends mostly on two different factors. Data are considered to be of "good" quality if:

1. the optical module is stable;

2. the status of the files is not affected by external disturbances, which would destroy the important information.

Not all PMTs of the AMANDA array are in a optimal status for the SN analysis. To define their quality, the PMTs can be classified in three different classes: (1) *good*, (2) *bad*, and (3) *dead*.
To assign the individual PMTs to their classes, statistical information is calculated periodically for every file (length $\sim$ 15 hours) throughout the two years (97 & 98). Assuming a Gaussian behavior of the counting rate, PMTs are classified as a function of the behavior of the following variables: (1) average counting rate; (2) root mean square (RMS) of the counting rate distribution; (3) standard

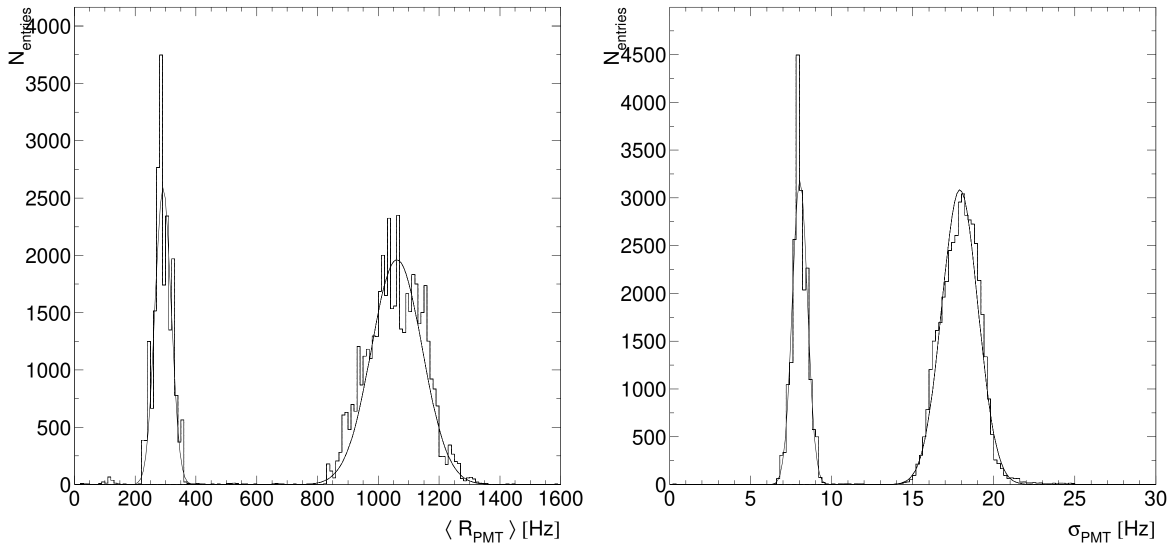

Figure 7.28: $\langle R_{\rm PMT}\rangle$ and $\sigma_{\rm PMT}$ distribution for the selected runs and PMTs of 97 and 98 data. The two peaks correspond to string 1-4 and string 5-10. The fits give $\langle R_{\rm PMT}\rangle = 290 \pm 26$ Hz and 1100 ± 80 Hz; $\sigma_{\rm PMT} = 8.0 \pm 0.5$ Hz and 18 ± 1 Hz.

deviation; (4) chi-square of Gauss fit; (5) frequency of large fluctuations of the counting rate which exceed a given number of standard deviations. These are some variables which can be checked to prove the stability of single PMTs for long-term periods. PMTs are defined as "good", when they show for a long time period (e.g. two years) a stable behavior of the noise rate, ($\langle R_{\rm PMT}\rangle \sim 300$ Hz for strings 1-4 and ~ 1100 Hz for strings 5-10) and a constant value of the RMS, ($\sigma_{\rm PMT} \sim 8$ Hz and ~ 18 Hz) without sudden jumps or drops (see Fig.7.28 and 7.29), as results after the final cleaning (see Sec.8.4). The information given by these variables distinguishes stable PMTs from unstable PMTs. Although the corresponding average value can be changed by long-term trends, the RMS remains rather constant for the stable PMTs.
Fig.7.30 shows the same variables versus day as in Fig.7.29, but for a sample of "bad" and "dead" PMTs. Some PMTs are clear examples of dead PMTs, since they show either high values or very low values of RMS close to zero. "Bad" PMTs are PMTs which show unstable behavior of the counting rate over long-term periods. Such PMTs were rejected by *pre-cleaning*, described quantitatively in Sec.8.

7.3 Disturbances

7.3.1 External Disturbances

The data in some periods during the year are affected by disturbances, which can involve either some PMTs of the array or even the whole array. Such disturbances can be classified into two types:
(a) External disturbances due to factors outside the detector.
(b) intrinsic disturbances inherent to the under-ice part of AMANDA independent from human control.
The first can be summarized as follows:

1. Crash of the SNMP DAQ system;

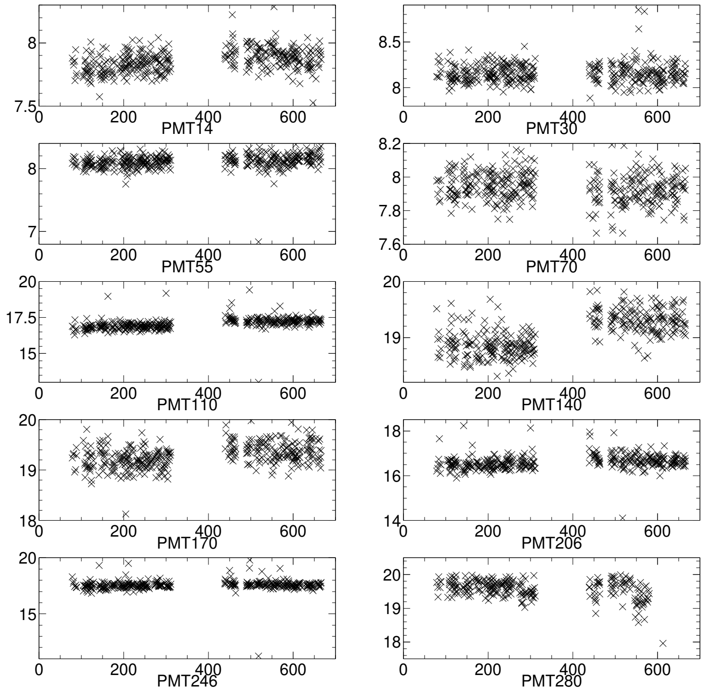

Figure 7.29: RMS of the rate as a function of time for 10 different "good" PMTs each belonging to a different string of AMANDA B10. Here it can be clearly noted that PMTs belonging to strings 1-4 are sitting around the value RMS $\sim$ 8 Hz, while strings 5-10 have a larger value around $\sim$ 18 Hz due to their higher counting rate.

2. Stop of the SNMP system;
3. Turn on of calibration light sources (YAG laser);
4. Start of external experiments, like "RICE", "SPASE";
5. Crash of the GRB (Gamma Ray Burst) system;
6. Power problems, Power out, or High voltage problems;
7. Other external disturbance sources not yet known.

The mentioned occurrences were recorded in a special log-book for SNMP and GRB systems [Sch97]. In Fig.7.31 an example of such external disturbances is depicted, where some PMTs got very high value of the noise rate due to the turn on of artificial light sources. Files showing such disturbances were removed a priori by pre-cleaning (see Sec.8.2).

7.3.2 Intrinsic Disturbances

The second class of disturbances are of intrinsic nature and can affect either individual PMTs or several PMTs showing correlation behavior. These effects cannot be changed, once the detector is deployed. The following factors can be referred to as intrinsic disturbances:

1. properties of the glass spheres of some OMs

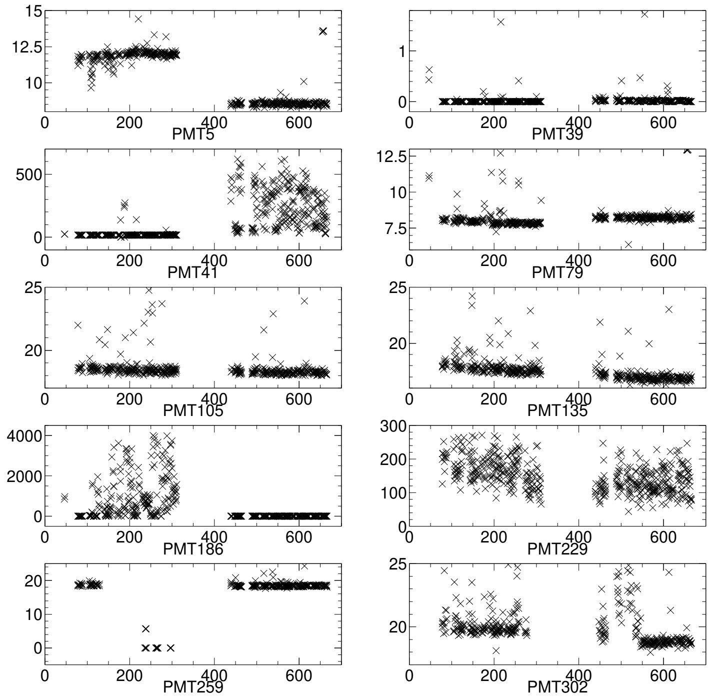

Figure 7.30: RMS of the rate as a function of time for pathological PMTs. Such instabilities are reflected in the bad value of the RMS, in sudden jumps and discontinuities in the counting rate. Again PMTs are chosen one for each string of AMANDA B10.

2. cross-talk
3. Internal variation of PMTs like aging, discharges, etc.

The first characteristics plays an important role for PMTs belonging to strings 5-10. The glass of these OMs contains a higher percentage of $^{40}\mathrm{K}$, a radioactive isotope of potassium with a decay time constant of $\sim 1.3 \cdot 10^9$ yr. This feature leads to a serious problem for a SN analysis, because the counting rate due to the radioactive decays is four times larger for strings 5-10 (Benthos-sphere) compared to strings 1-4 (Billings-sphere). The potassium content of Benthos is 2.3% , that of Billings is $< 0.5\%$ [Spi]. The typical counting rate averages $\langle R_{SN} \rangle$ are ~ 300 Hz and ~ 1100 Hz for OMs 1-86 (strings 1-4) and OMs 87-302 (strings 5-10), respectively (see Fig.7.32 and Fig.7.28). The higher value of the counting rate of OMs 87-302 causes a broader background dark noise distribution.
The second concerns the intrinsic correlations due to “cross-talk” between neighbour electrical cables. Via cross-talk, PMTs can affect otherwise stable OMs located on the same string.

7.4 Data Behavior

Interesting data behavior can be seen in Fig.7.33 plotting the summed counting rate averaged for each file ($\sim$ 15 hours) $\langle S_{tot} \rangle$ of the 170 selected PMTs during two years. The lines on top of each cluster are the corresponding fits with an exponential function. $\langle S_{tot} \rangle$ decreases by $\sim 2\%$ per year, and the estimated time decay constant of $\langle S_{tot} \rangle$ amounts to 65 yr for both data samples. This

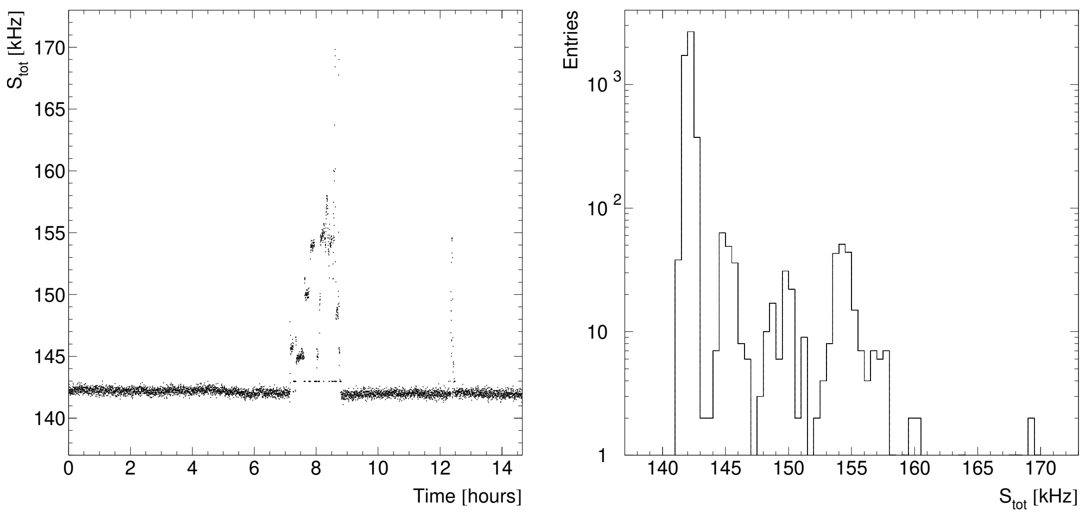

Figure 7.31: (Left) Summed noise rate over the good selected PMTs S_{tot} (kHz) as a function of time (hours). The plot shows data from a file which was rejected. (Right) S_{tot} distribution for the same file. Due to such disturbances the Gaussian behavior is destroyed.

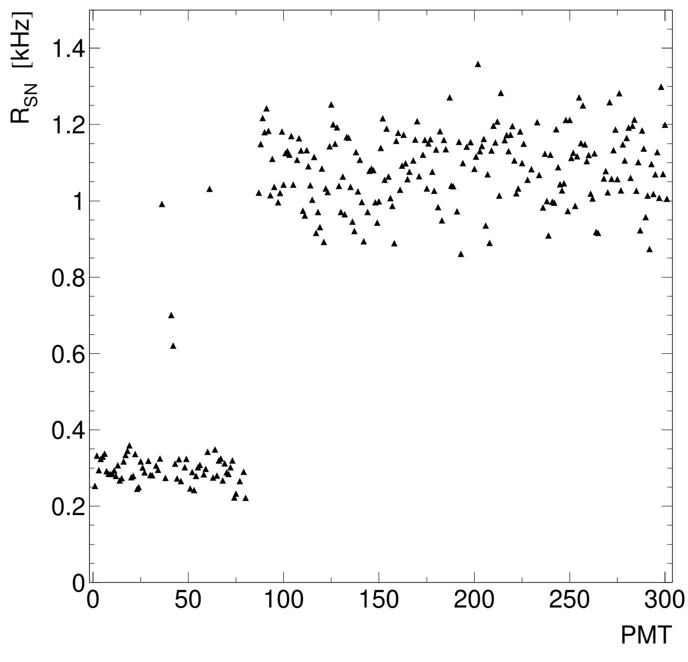

Figure 7.32: Counting rate average $\langle R_{SN} \rangle$ as a function of PMT number. The two clusters distinguish strings 1-4 ($\langle R_{SN} \rangle \sim$ 300 Hz) strings 5-10 ($\langle R_{SN} \rangle \sim$ 1100 Hz)

is consistent with the observed slight decrease of the 1 pe amplitudes for OMs 87-302 [Spi99]. Notice the fast decay at the beginning of each data sample, which does not follow the exponential behavior, especially accentuated at the start of 98 data taking around day $\sim$ 450. This feature is not yet completely understood and is still under study.

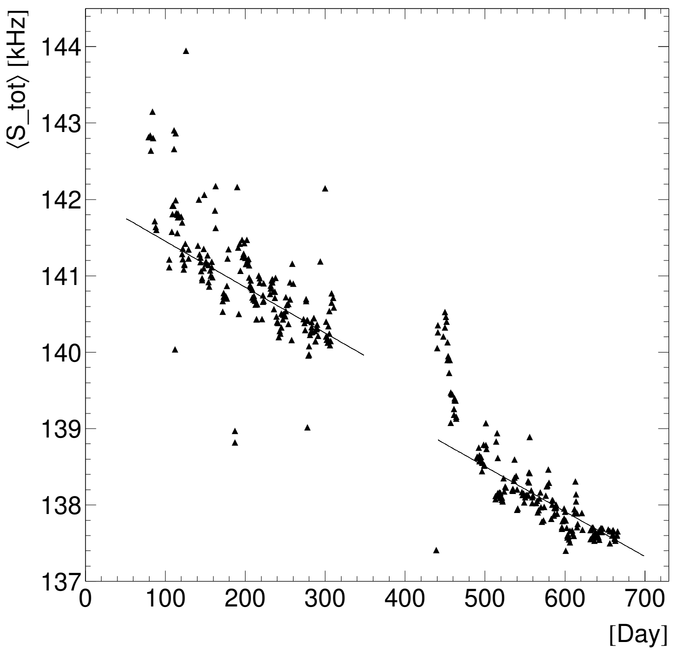

Figure 7.33: Summed counting rate $\langle S_{tot} \rangle$ (kHz) averaged every $\sim$ 15 hours as a function of time (day), each point represent the average value over one file. Both data samples were fitted with a exponential function. One clearly sees the slight decay ($\sim 2\%$) of $\langle S_{tot} \rangle$ both for the first and second cluster of points which distinguishes the 97 & 98 data, the gap between day 320-420 is related to the Austral Summer period where no data are taken.

7.4.1 Dark and non-Poissonian Noise

The counting rate background shows stronger variations than Poisson statistics would predict. Assuming Poisson statistics, the RMS fluctuation of the combined noise from all the OMs is expected to be, as discussed in Sec.5.4

$$\sigma_{RMS} = \sqrt{10 \text{ sec } R_{back} \; N_{OM}} \tag{7.27}$$

where R_{back} and N_{OM} are the observed background counting rate of an individual PMT and the total number of OMs, respectively. This expression has to be independently considered for strings 1-4 and strings 5-10, since the observed dark noise background for these PMTs corresponds to $\sim$ 300 Hz and $\sim$ 1100 Hz, respectively. Fig.7.34 shows the ratio $\sigma_{obs}/\sigma_{Poi}$ distributions for strings 1-4 and 5-10 corresponding to 1.49 $\pm$ 0.03 and 1.74 $\pm$ 0.05, respectively. To estimate how large the disagreement is between the expected Poissonian and the observed behavior, one can calculate the ratio $\sigma_{obs}/\sigma_{Poi}$, where σ_{obs} is the measured standard deviation of the background noise and $\sigma_{Poi} = \sqrt{10 \text{ sec } \langle R_{back} \rangle}$ is the expected RMS fluctuation individually considered for each PMT. The reason of this discrepancy is not yet completely understood.
The non-conformity with the Poisson behavior is clearly correlated to the magnitude of the average of the measured noise (see Fig.7.35).

7.5 SN Data compared with Muon Data

Sec.6.2.1 explained the principle of the after-pulse suppression (APS) which inhibits the counting electronics for a maximum of 12.8 μsec after a pulse. To estimate the efficiency of the APS on the

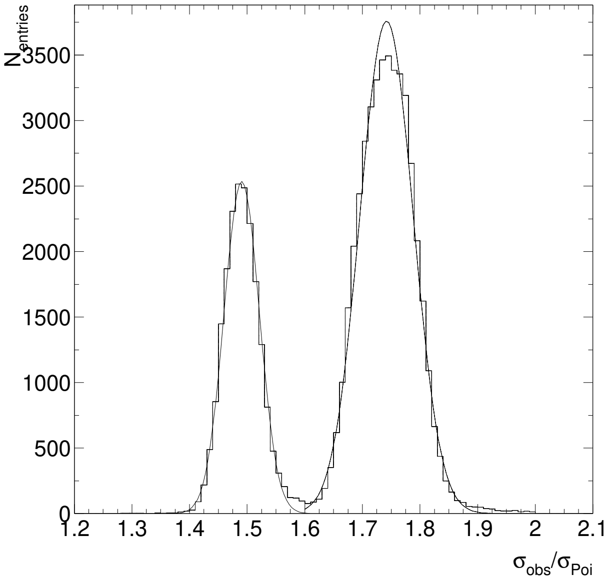

Figure 7.34: The ratio $\sigma_{obs}/\sigma_{Poi}$ distribution for the two years statistics 97 & 98 data. The two prominent peaks correspond to strings 1-4 and strings 5-10, which are centered around the values 1.49 $\pm$ 0.03 and 1.74 $\pm$ 0.05, respectively.

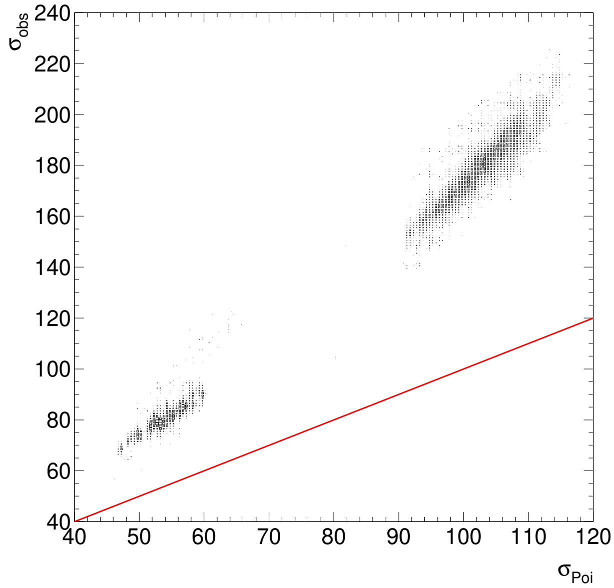

Figure 7.35: Scatter plot of the observed standard deviation versus the expected Poisson RMS fluctuations. The two distinct clusters indicate the OMs of strings 1-4 (on bottom left) and strings 5-10 (on the top right), again for two years statistics. The solid line represents the value of σ_{obs} if it would be the case of a pure Poisson process.

SN data, a comparison is useful between these and "muon-data" where no APS is applied.
The difference of the magnitude in the counting rate is easy to see, comparing the average $\langle R_\mu \rangle$ and $\langle R_{SN} \rangle$ in Fig.7.36 and Fig.7.32, respectively. The muon data cluster around $\sim$ 400 Hz and $\sim$ 1500 Hz for strings 1-4 and strings 5-10, whereas the SN data rates are reduced to $\sim$ 300 Hz and

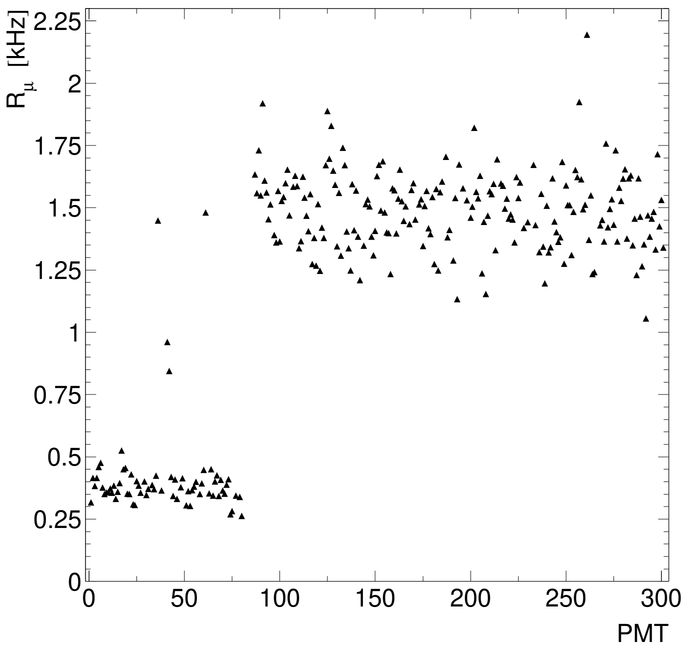

Figure 7.36: Average of the counting rate $\langle R_\mu \rangle$ as a function of PMT number for the muon data to be compared to Fig.7.32.

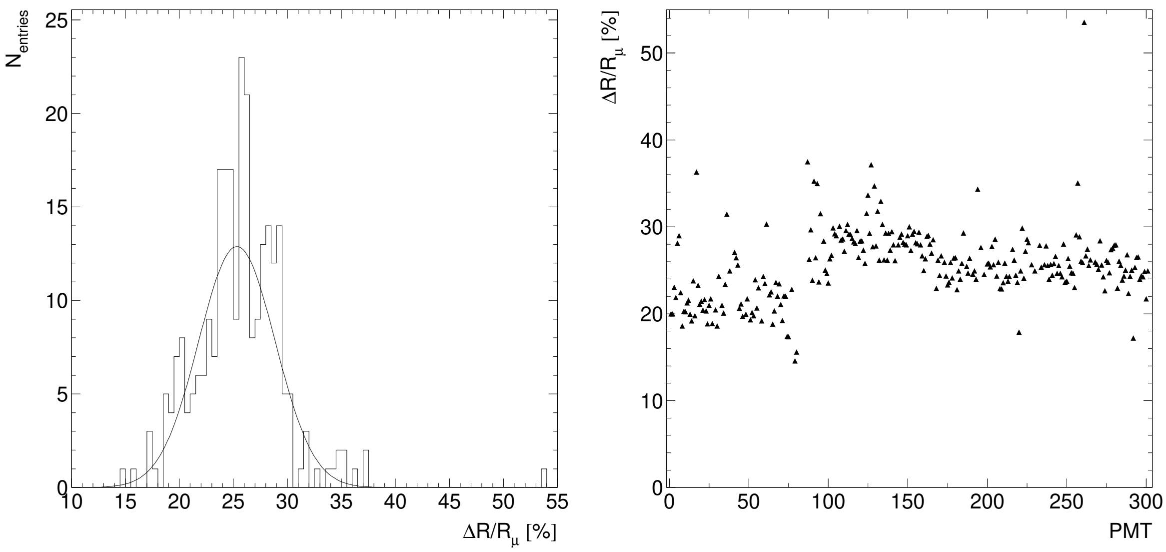

Figure 7.37: (Left), relative excess of the noise rate of the muon data compared to SN data. Fitting the distribution of the excess rate with a Gaussian one gets $25 \pm 3.5\%$ for the mean excess. (Right), the variable $\Delta R/R_\mu$ as a function of PMT number

$\sim$ 1100 Hz, respectively. Fig.7.37 shows the relative excess of the noise rate $\Delta R/R_\mu$ due to the after-pulse which amounts to $\sim 25\%$. Plotting this variable versus PMT number (Fig.7.37 right), it appears that the excess is not uniformly distributed over all PMTs. This suggests that the APS is more efficient for the more noisy PMTs of strings 5-10 than for strings 1-4.

8 Data Cleaning

8.1 Introduction

The main goal of this section is to present how the different features of the data can be understood. This involves both characteristics of the single PMTs and of single files. The process of file and PMT cleaning occurs in different stages. First a so-called *pre-cleaning* is needed both for the file and PMT sample, which means removing known periods and PMTs known to be very bad and unstable. Notice, that the "bad" PMTs for SN analysis in most cases can be used for the standard muon analysis.
The second step consists in an iterative cleaning through an algorithm, which making use of quality parameters, rejects automatically the remaining unstable files and PMTs. After that the final sample of "good" files and PMTs has been obtained.

8.2 Pre-Cleaning of "Bad" Files and PMTs

The pre-cleaning consists in the removal of very unstable files *by hand*, using the information reported in the log-book for SNMP and GRB system as discussed in Sec.7.3.1. Indeed some strong correlations were found between the technical problems reported in the log-book and the very bad behavior of the SN data in the same periods. Thus, these files were considered "damaged" by external actions, and therefore they have been rejected a priori. As second criterion to reject unstable files, the χ^2/ndf of Gaussian fit of the summed counting rate distribution S_{tot} over the selected PMTs for each individual file was considered. A file was defined to be of bad quality if its χ^2/ndf was found larger than 2. Thus, for the SN off-line analysis a total number of 26 and 36 files have been pre-cleaned which correspond to $\sim$ 16 and 22 lifetime days of 97 and 98 data respectively, see also Tab.8.2.
Pre-cleaning consists also in a removal of PMTs, which are known to be very noisy for very long periods or even for the whole year, considering the feature studied in Sec.7.2 In total 117 PMTs have been removed, so that the remaining 185 PMTs have to be checked at the second cleaning stage.

8.3 Choice of Cuts for each PMT Behavior

After the first cut selection of the pre-cleaning, a proper quality is defined for the remaining PMTs considering their statistical features. For each file, the behavior of the counting rate distribution R_{PMT} for each PMT is studied. Assuming Gaussian behavior of this distribution the mean value, root mean square, fitted mean and its standard deviation can been calculated. Studying independent statistical properties for each single PMT, three different constraints have been considered.
I) As a first constraint, adequate value ranges of the average $\langle R_{PMT} \rangle$ were chosen taking into account if the PMTs belong to strings 1-4 or 5-10. Because of the different nature of these two PMT families, the ranges of $\langle R_{PMT} \rangle$ were decided as follows: ($180 < \langle R_{PMT} \rangle < 400$) Hz and ($800 < \langle R_{PMT} \rangle < 1400$) Hz for PMTs on strings 1-4 and 5-10 respectively. Fig.8.38 shows the scatter plot of $\langle R_{PMT97} \rangle$ versus $\langle R_{PMT98} \rangle$ where the two clusters representing PMTs of strings 1-4 (on the bottom left) and PMTs of strings 5-10 (on the top right) can be seen clearly. Notice that the picture was plotted without application of any cuts, this proves the fact that the considered subsample contains PMTs of long term stability.

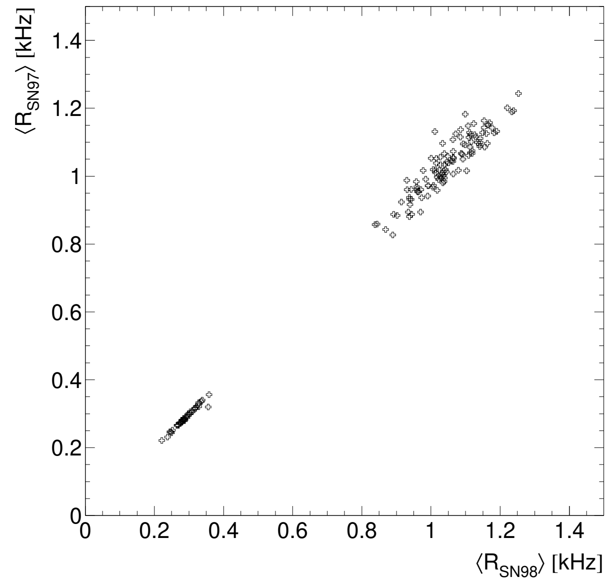

Figure 8.38: Counting rate average $\langle R_{PMT} \rangle$ of data 97 versus $\langle R_{PMT} \rangle$ data 98. The plot shows the selected subsample of PMTs for the combined data of the two years.

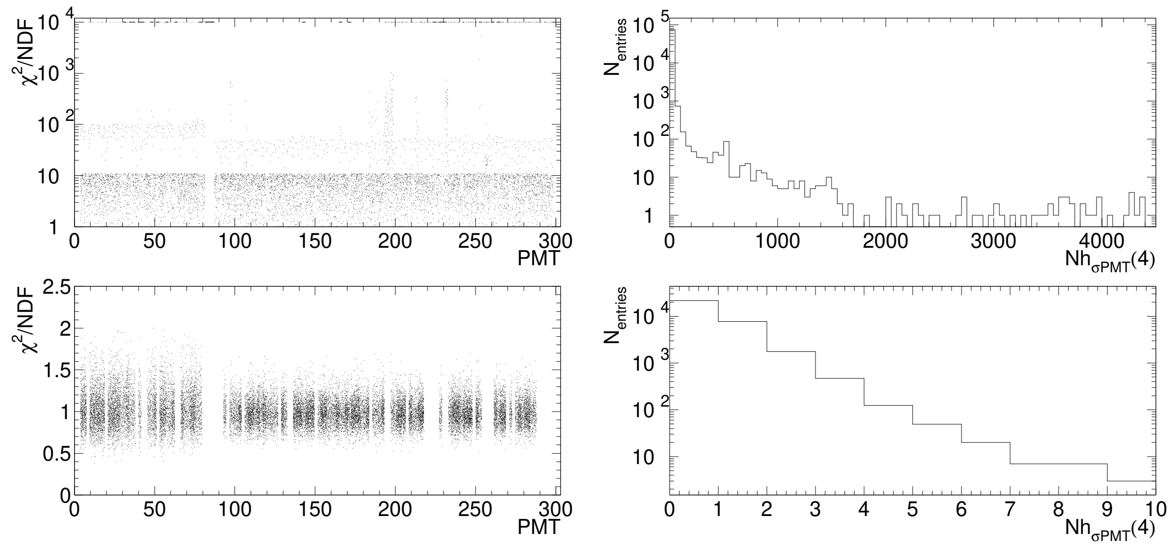

Figure 8.39: (Left) χ^2/ndf values for all files as a function of PMT number. On the top the behavior of the χ^2/ndf values without any cuts is shown. The result for the selected PMTs only is illustrated on the bottom, also without any cut application. (Right) Distribution of the variable $Nh_{\sigma_{PMT}}(4)$ for all PMTs and for all files. The histogram on the top represent the distribution where no cuts were applied, whereas the histogram on the bottom is the resulting distribution for the selected PMTs only, also without any cuts.

II) The second constraint for the single PMTs is imposed to the χ^2/ndf values from the Gaussian fit of the counting rate distribution calculated for each file. The large value of χ^2/ndf around 10000 shown in Fig.8.39 left (on the top) has to be connected with periods, in which the detector was "out of control" and most of all PMTs were badly influenced. For this reason applying a reasonable cut

on $\chi^2/ndf < 2$ for all PMTs, less than 5% of all events were rejected, (see Fig.8.39 left on the bottom). Notice the marked difference between the AMANDA B4 PMTs (1-80) and the remaining, where the χ^2/ndf for the first has a larger value than for the latter. Although the AMANDA B4 PMTs behave better than the PMTs of strings 5-10 due to their lower value of noise rate ($\sim$ 300 Hz poorer statistics against $\sim$ 1100 Hz), the more noisy PMTs (87-302) are more Gaussian.
III) As a last constraint imposed upon the single PMTs, a new variable was defined as follows: $Nh_{\sigma_{PMT}}(i)$ defines the total number of events, where the counting rate R_{PMT} in 10 sec intervals of a PMT exceeds a given 'i' number of standard deviations during the periods of a year. For instance it can be demanded that the counting rate of a PMT should not exceed 4 standard deviations more than 10 times in all files. Fig.8.39 right shows the distribution of $Nh_{\sigma_{PMT}}(4)$ on the top, and on the bottom for the selected PMTs only. The distribution of counting rate excesses exhibits an exponential behavior.

8.4 Final Cleaning

To reach the final cleaning a *PMT-FILE selection* algorithm was used, which was already successfully applied to clean data for muon analysis [Bou99]. This cleaning algorithm needs as input a table with the following information: (1) file number; (2) PMT number; (3) PMT quality. As defined in the previous section, a PMT is considered to be of "Quality = 1", if all three constrains (I) $180 < \langle R_{PMT}\rangle < 400$ or $800 < \langle R_{PMT}\rangle < 1400$, II) $\chi^2/ndf < 2$ and III) $Nh_{\sigma_{PMT}}(4) < 10$) are satisfied at the same time, otherwise the PMT is of "Quality = 0". Fig.8.40 left ("Figure of merit") represents a matrix of number of PMT and files, where the single "black points" indicate the Quality = 1 for a given PMT in a particular file. The remaining white regions represent either bad periods or "bad" PMTs, which are denoted with Quality = 0. The large number of black points

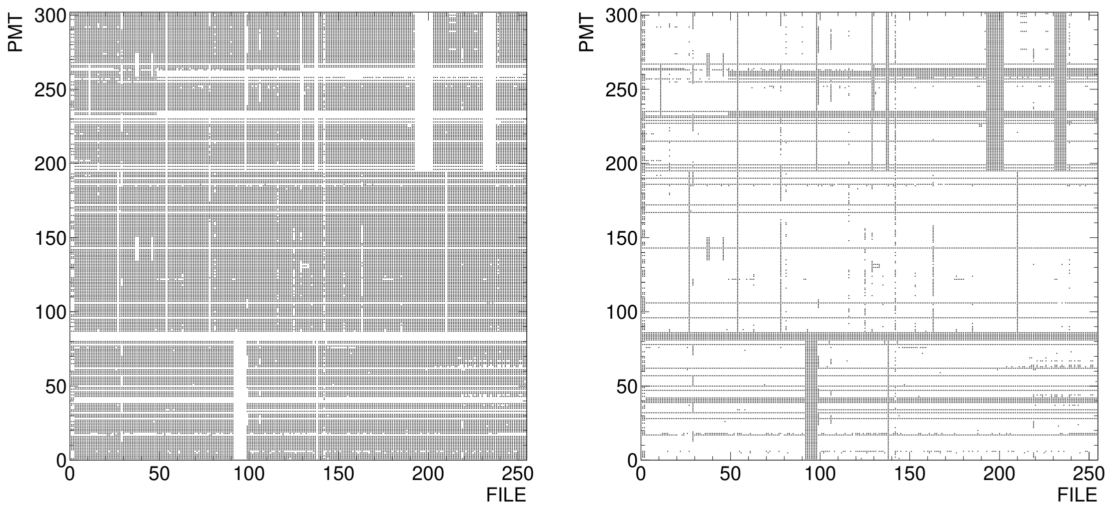

Figure 8.40: The "Figure of merit" as a matrix of the PMT number (302 rows) and files (255 columns). The "Quality = 1" for a given PMT in a particular file is denoted through black points whereas white points with the meaning "Quality = 0" indicate either bad periods or "bad" PMTs (left). (Right) Negative representation of "figure of merit". Here can be seen more clearly the periods of bad behavior of the detector denoted in this case with black points.

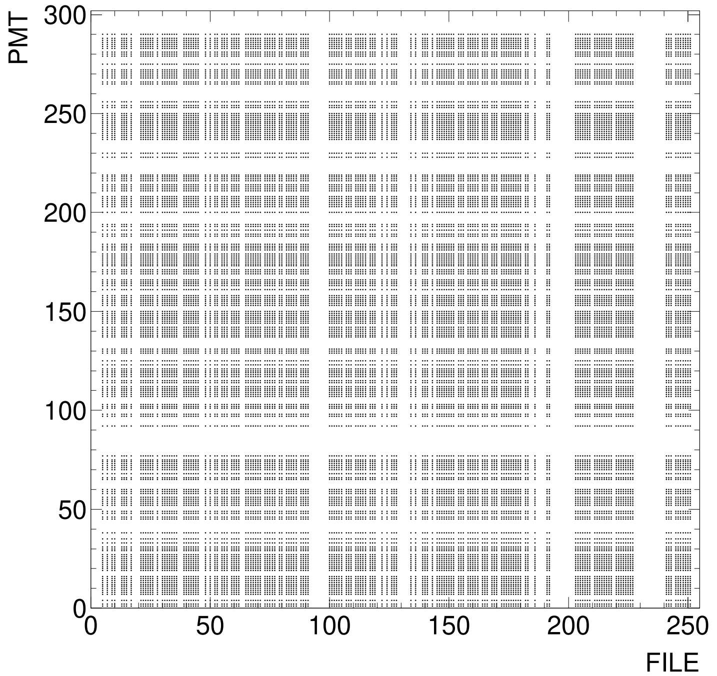

Figure 8.41: The “Figure of merit” as output of the PMT-FILE selection algorithm after the final cleaning. The remaining black points are the extracted sample of stable files and PMTs.

in the “Figure of merit” represents PMTs which satisfied the three constraints discussed above during stable periods. The prominent vertical white regions indicate three bad periods, where distinct parts of the detector were not working. The two bad periods on the top right concern the last strings (8, 9, 10) of the detector AMANDA B10, which where out. The first 4 strings of AMANDA B4, were not read out during the periods around file 95. The long white horizontal line in the “Figure of merit” represents 6 PMTs (81-86), which are always turned off.

The corresponding negative representation of the “Figure of merit” is given in Fig.8.40 right. The goal is to clean the “black points” in the negative “Figure of merit” in a reasonable way, so as to leave a constant number of stable PMTs throughout the year. The final cleaning is devised applying the PMT-FILE algorithm which removes “bad” PMTs and files in three different steps [Bou]:

(1) Compute the sum of each row and each column in the negative “Figure of merit”, i.e. calculate the sum of all black points in each row and column.

(2) Find the “worst” of all rows and all columns, this means find out the row/column with the largest number of black points. Then remove it (the whole row/column) from the table.

(3) If all PMTs are stable in exactly the same set of files, then stop the cleaning process, otherwise go to point (1) and repeat the cycle.

The resulting graph of the “Figure of merit” after cycle convergence is shown in Fig.8.41, where the worse parts due to an unstable file or PMTs are completely removed. The corresponding negative picture is totally empty. It can be seen that the algorithm reasonably prefers to remove all worse files around the values 95, 200 and 240, instead of touching the corresponding PMTs. The algorithm rejects adjacent PMTs in strings around PMTs 40, 230 and completely the last 10 PMTs.

After this final cleaning, 170 PMTs from strings 1-10 (51 PMTs strings 1-4) and 185 files were left for 1997, whereas 170 PMTs (53 PMTs from strings 1-4) and 205 files were left for 1998. This amounts to a total live-time of $\sim$ 220 days. Notice that runs have different lengths and the corresponding removed files, which are the bad ones, presented a short run length. The same number of PMTs for the SN off-line analysis of both 97 and 98 data is not casual. The explanation is that this chosen sample of "good" PMTs is a sample which contains very stable PMTs demonstrating the same statistical feature for long term periods (see also Fig.8.38). This will be a crucial information for a future on-line Supernova monitoring, which needs of course a reliable sample of "good" PMTs. The important aspect of a development of an on-line Supernova trigger algorithm will be studied below in section 16. The different rejection steps for the data and OM sample 97 & 98 are summarized in Tab:8.2, A list of the "good" selected OMs for SN data 97 and 98 can be found in App. B, whereas a list of problematic OMs can be found in App. C.

Rejection Steps	Data 97	Data 98	Data 97	Data 98
	FILEs	FILEs	OMs	OMs
available	318	299	302	302
missing time info.	63	48	-	-
pre-cleaning	23	28	117	119
"bad" χ^2 of $S_{tot.}$	3	8	-	-
algorithm rejection	44	10	15	13
used in analysis	185	205	170	170

Table 8.2: Summary of the different rejection steps for 97 & 98 data and OM sample

9 Monte Carlo

9.1 Introduction

To simulate supernova events in the AMANDA detector, two different issues have to be considered:

1. Simulation of dark noise background.
2. Simulation of the supernova signal on top of that background.

In this section the techniques which are used to generate both the background events and the supernova signal are explained, where the latter has to take into account all parameters which can influence the detection efficiency. As first consideration one can approximate the distribution of the background events R_{back} as a Gaussian with mean $\langle R_{back}\rangle$ and standard deviation $\sigma_{back} = \sqrt{10 \text{ sec } \langle R_{back}\rangle}$. Thus, to simulate background, a generator of normal distributed variables combined with the statistical information from the data was used.
Subsequently two different approaches to simulate a supernova signal will be described. The first considers a supernova event without the constraints of the detection efficiency, i.e. supernova events *ad hoc* generated on top of the background distribution. The second approach is more rigorous and consistent, since it will take into account not only the reduced detection efficiency due to the fixed counting rate of 10 sec intervals (see par.12.2), but also the expected supernova signal from the Galactic star distribution (see par.13.1) and from the inevitable Gaussian smearing of the effective signal.

9.2 Dark Noise Background and Supernova Signal Simulation

Here, the statistical information from the data, which describes the behavior of the dark noise background, can be integrated into the simulation. The mean value of the counting rate distribution $\langle R_{back} \rangle$ for each individual PMT and the corresponding standard deviation $\sigma_{R_{back}}$ from a Gaussian fit was considered as input parameter for the statistical information. As mentioned above (see Sec.7.4.1), this standard deviation does not follow Poisson statistics: $\sigma_{obs} > \sqrt{10 \text{ sec} \langle R_{back} \rangle}$. These statistical values were calculated from a chosen (long) run of data 97 within a stable period of the detector.

To simulate a supernova on top of dark noise background, the Eq.5.25 was used. From Eq:5.25 the expected number of photo-electron $N_{\rm 1pe}$, which would increase the dark noise counting rate of a single PMT, is inversely proportional to the square of the distance to the supernova. For a supernova like SN 1987A at $\sim$ 8 kpc, close to the Galactic center, the counting rate excess is estimated to be $N_{\rm 1pe} \sim 100$ in an interval of 10 sec. This information is used as input parameter for the simulation, so that the background distribution combined with the supernova signal can be written as follows

$$\underbrace{\left(y(x) \cdot \sigma_{R_{back}} + \langle R_{back} \rangle \right)}_{dark\ noise\ background} + \underbrace{\left(y(x) \cdot \frac{\sqrt{N_{\rm 1pe}}}{\Delta t} + \frac{N_{\rm 1pe}}{\Delta t} \right)}_{supernova\ signal} \tag{9.28}$$

where $y(x)$ is the generated normally distributed variable with zero mean and unit variance, and Δt is the regarded time interval, in our case 10 sec.

The first expression in brackets has to be interpreted as the dark noise background distribution which describes the observed data, whereas the second indicates the simulated supernova events. From this expression can be seen that the generated supernovae are Gaussian distributed around the average value of $N_{\rm 1pe}/\Delta t$. For the Monte Carlo comparison with data see, Sec.11.5 and 11.6.

10 Methods of Analysis

10.1 Introduction

The idea of the analysis described in this chapter is to conserve the information in the data containing a potential SN burst of a time scale of the order of 10 sec and suppress external influences of a larger time scale of several hours up to days and other irregular fluctuations which could induce SN fake events. For this aim two basic methods have been used:

1. a moving average (MA) method;
2. a Maximum-Likelihood method.

The moving average is in essence a filter, which can correct for trends or seasonal effects, maintaining at the same time the intrinsic information of importance for the analysis.

The Maximum-Likelihood method is used especially to reject possible fake events, which can be confused with a supernova event. Both these principles are discussed in detail in the following sections. The principles of the methods developed for this off-line SN analysis are outlined, and the data which have been used are briefly discussed. To analyze the data and to understand its behavior, a *Main Analysis* program was used, which yields the crucial information to extract the analysis results.

10.2 Steps of the Off-line SN Analysis

The different steps of the off-line SN analysis, which are depicted schematically in Fig.10.42, can be summarized as follows. (1) The complete SNMP data sample taken at South Pole during the Austral Winter seasons 97 & 98 were recorded on DAT tapes, which were shipped back at the end of each year. These contain binary files, in which the counting rate information in 500 msec intervals is saved for all individual PMTs (see Sec.6.3). In addition the absolute time for each event with a time resolution of the order of 1 sec is also recorded.
A reader for SN data was used to convert the binary files into a preliminary HBOOK-file version. The reader not only translates the format of the files, but also sums 20 adjacent 500 msec intervals in order to form counting rate of 10 sec intervals. The decision to use fixed 10 sec intervals was taken, because the time duration of a typical supernova burst is expected to be of that order. To study the statistical information of the data in detail, the HBOOK-files were then converted

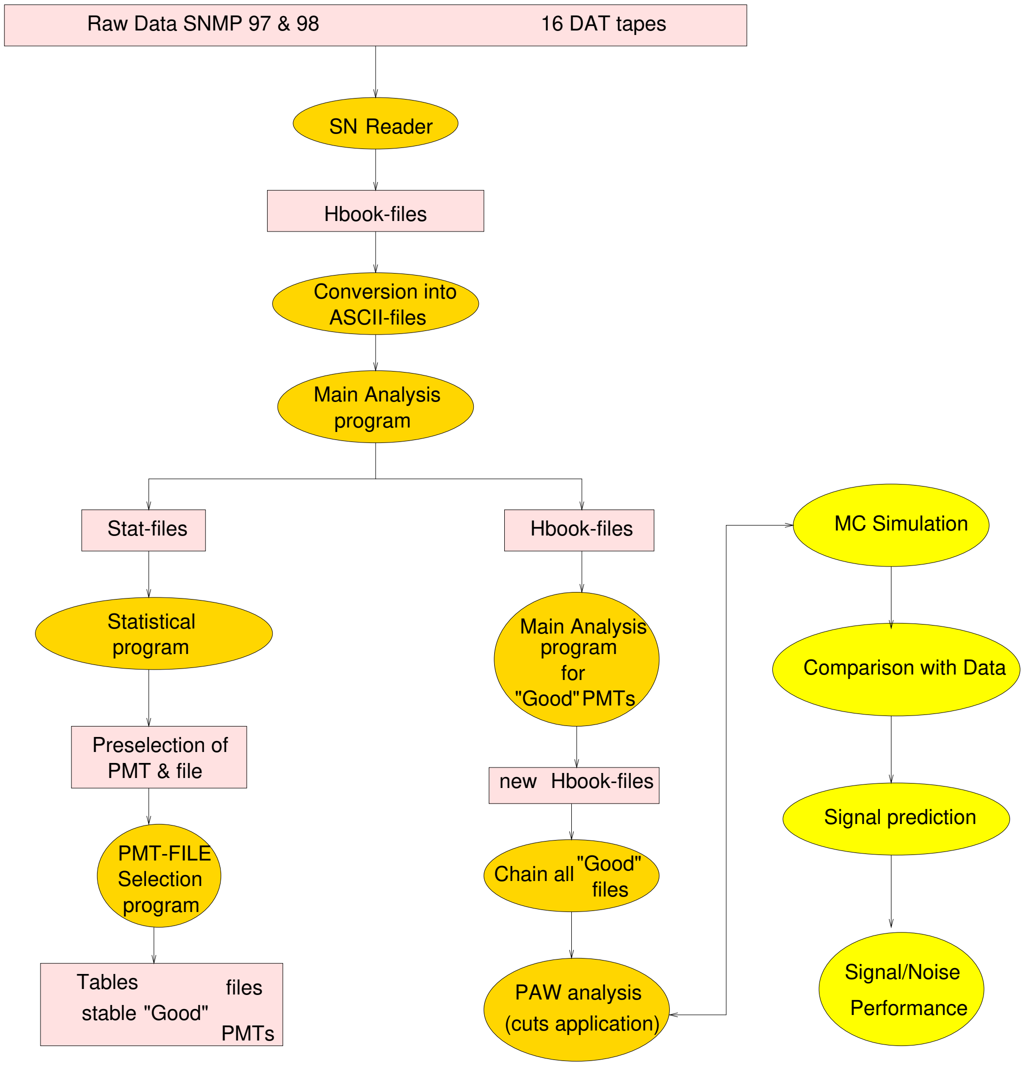

Figure 10.42: Steps of the off-line SN analysis for data 97 & 98. Raw data are converted with a SN reader. Three important tools (programs) have been developed for the analysis: 1. Main Analysis program; 2. Statistics program; 3. PMT-FILE Selection program. The HBOOK output files were computed in PAW to obtain the ultimate results. Monte Carlo algorithms were also developed for the comparison with data and signal prediction.

into ASCII files, which are the input of the Main Analysis program. The Main Analysis program makes use also of the selected table of stable PMTs illustrated in App.B. The output of the program consists in HBOOK [Bun95] files containing Ntuples, which have been computed in PAW (Physics Analysis Workstation) [Cou95] for the final analysis step. For every file Gaussian fits are made both for each PMT and for summed rate distributions and additional statistical information is stored in statistics files. These statistics files are further the input of the statistics program used for the understanding of the data behavior at the first level and for data cleaning.

10.3 Trends and Seasonal Effects of the Data

To understand the principle of the moving average used for the SN analysis, it is useful to consider the counting rate observations as a function of the time, or better as a time series.
The aim is to conserve the SN information of such a time series and suppress external influences, as trends, seasonal effects, discontinuities and other irregular fluctuations. Such disturbances can be summarized as follows.
(1) Seasonal effects correlated with temperature, wind and other atmospheric variables.
(2) A long-term change in average can be defined as a trend. Nevertheless the expression "long-term trend" has to be taken with care, since usually the trend identification can be subjective, depending on the duration of the data available [Cha82, BD96].
(3) Other irregular fluctuations which contain neither periodic nor long-term effects, but with a rather short time duration, are usually observations with sudden changes in average (e.g. high voltage problems can give rise to those).
Assuming a Gaussian behavior of the observed counting rate, one would expect a stationary time series for the counting rate as a function of time. Stationary time series are defined to be observations, which indicate no trends, no changes in the variance and no periodical fluctuations. Thus, the external effects which make the expected time series non-stationary have to be removed.

10.4 Moving Average (MA)

To achieve this aim, the moving average (MA) was subtracted from the measurements. The moving average is the average of the counting rate during a certain time window (TW), which can be e.g. centered around the considered 10 sec time bin. Fig.10.43 shows the behavior of the moving average schematically (solid line) for counting rate data as a function of time. Given a fixed TW which contains a bin sample centered on the considered time event, the MA is just the average value calculated over all included bins (included also the central bin). For the next event the average will be calculated over the same number of time bins but shifted by one bin, and so on. This is a symmetric moving average MA_{sym} used for the off-line SN analysis with the choice of a time window of 1000 sec, i.e. 100 bins. However, the method of MA_{sym} is working only if it is possible to look both at preceding and following events stored in a memory buffer with respect to a defined time event. For this reason it is obvious that such a method can not be applied for a real-time supernova monitoring, which will be discussed in Sec.16.
Fig.10.44 left illustrates the MA_{sym} principle. It shows the summed counting rate for the selected PMTs S_{tot} as a function of time (dots), where the smooth line represents the calculated moving average. The example in Fig.10.44 was chosen on purpose, to show the resulting suppression of the prominent peak and other non-desired fluctuations. To reach a more effective suppression of trends and fluctuations, the filter of MA_{sym} was not only applied to the summed counting rate S_{tot}, but also to each single PMT rate x_i. The resulting suppression can be achieved calculating

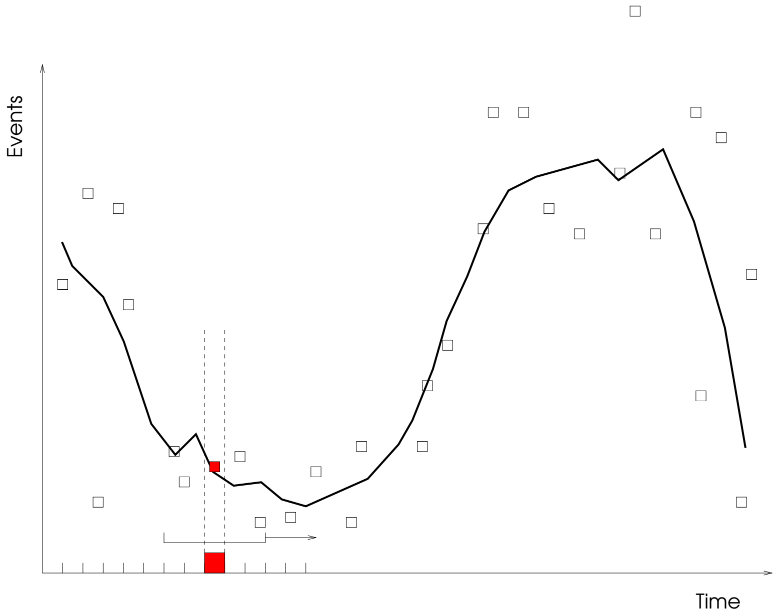

Figure 10.43: Schematic representation of the principle of the symmetric moving average MA_{sym} here with a time window (TW) of 5 events, for the analysis TW was chosen of 1000 sec. The squares indicate the measurements and the solid line the calculated MA_{sym}.

the residual deviation RES of the counting rate from the moving average MA_{sym}, both for each individual PMT and for their sum, which is defined as follows

$$\begin{aligned} RES(x_i(t)) &= x_i(t) - MA_{sym}(x_i(t)) \qquad for\ each\ PMT \\ RES(S_{tot}(t)) &= S_{tot}(t) - MA_{sym}(S_{tot}(t)) \qquad for\ the\ SUM \end{aligned} \tag{10.29}$$

Fig.10.44 right shows $RES + \langle S_{tot} \rangle$, i.e. the summed residual, shifted by the average value of the summed counting rate in order to simplify the representation and the comparison with the picture on the left. Note the efficiency of the filter $MA_{sym}(S_{tot}(t))$ which reduces short-time trends and fluctuations leaving the expected Gaussian behavior of the data, due to the appropriate choice of the TW-length. Their distributions (their projections on the y-axis), both before and after the subtraction of MA_{sym} can be seen in Fig.10.45. Due to large fluctuations, the distribution on the left is not Gaussian. In this case the data would be not usable for the analysis. However, MA_{sym} corrects the fluctuations in satisfying way, providing the desired Gaussian behavior of the background.
The filter provided by MA_{sym} would not cut away a SN event, as shown in Fig.10.46, since the large statistics enclosed in the TW of 1000 sec is not affected by an excess in counts during 10 sec only. Fig.10.47 illustrates the situation for a stable file where S_{tot} as a function of time does not show at a first glance any particular trend or other disturbance. Its projection on the $y-$axis has a Gaussian behavior, nevertheless the MA indicates a periodic effect with a period of $\sim$ 4000 sec. The filtered results after computing $RES(S_{tot}(t))$ are shown in Fig.10.48, where the periodic fluctuations are gone. It is interesting to see how the application of MA_{sym} behaves when sudden discontinuities occur like in Fig.10.49. An analysis could be very problematic with such features, if the data were not filtered in advance and it would be also unreasonable to remove completely the whole file, only to avoid such disturbances. In fact this file was used for the analysis after the application of $RES(S_{tot}(t))$. However also at that level the data are still affected by the

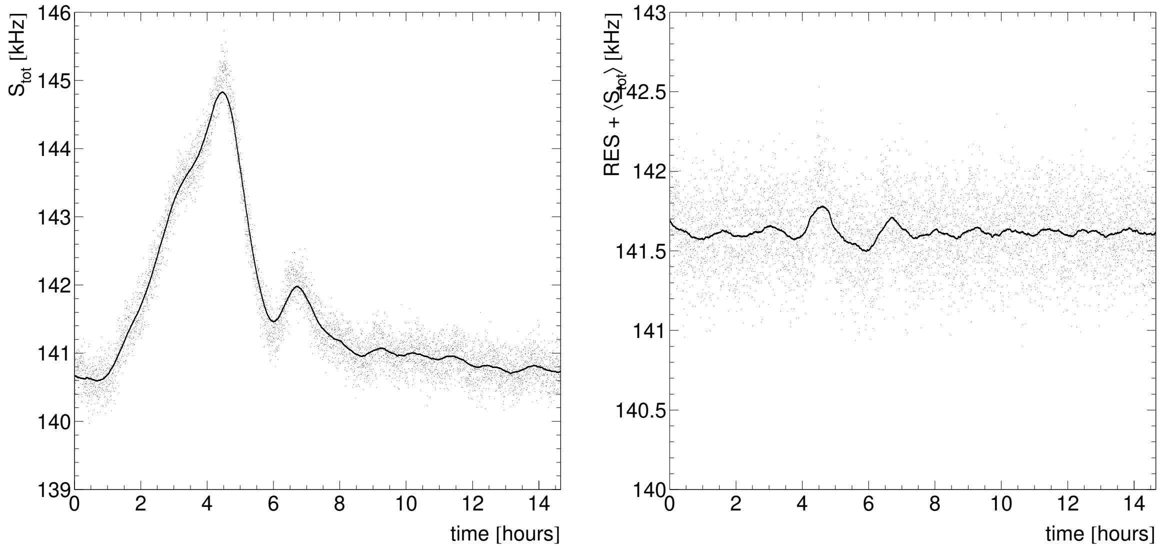

Figure 10.44: (Left) Summed counting rate $S_{tot.}$ (kHz) versus time (hours). Each dot in the dense cluster indicates one $S_{tot.}$ event and the solid line represents the calculated MA_{sym} with a TW of 1000 sec. The moving average MA_{sym} follows the long time behavior of the data. (Right) $RES + \langle S_{tot} \rangle$ summed residual shifted by the mean value $\langle S_{tot} \rangle$ the line represents its MA_{sym}.

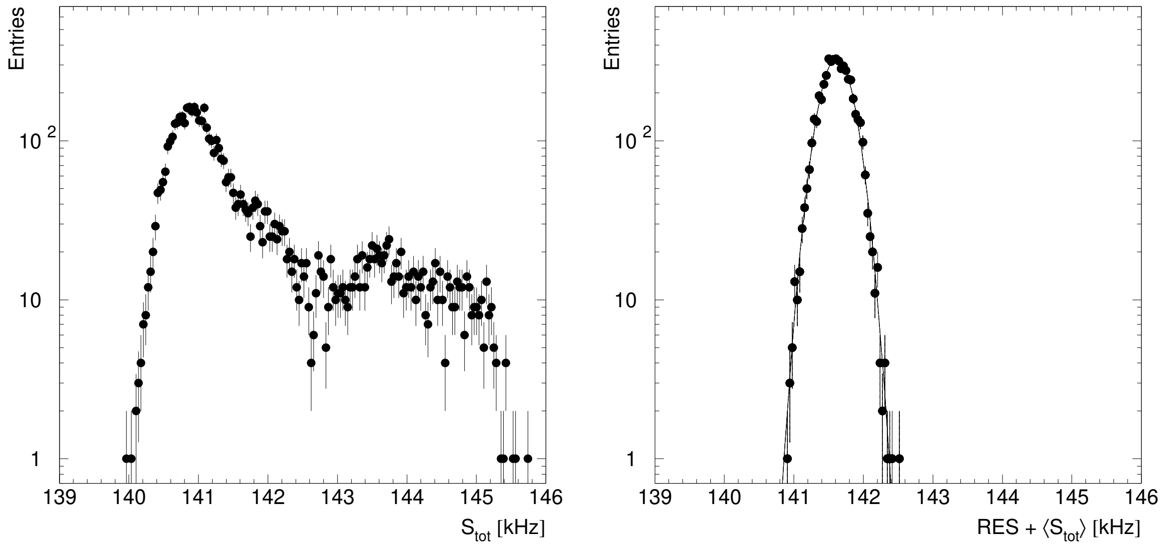

Figure 10.45: (Left) S_{tot} distribution for the same data file. (Right) $RES + \langle S_{tot} \rangle$ distribution as result after the subtraction of MA_{sym}. The Gaussian fit gives a $\chi^2/ndf = 1.2$.

discontinuity, as shown in Fig.10.50. This excess in the summed counting rate will be completely removed through the application of cuts on the Likelihood function $\mathcal{L}$ (or on the χ^2/ndf), which rejects events which are not Gaussian. The discussion about the Maximum-Likelihood method and the χ^2/ndf function is the topic of the next section.

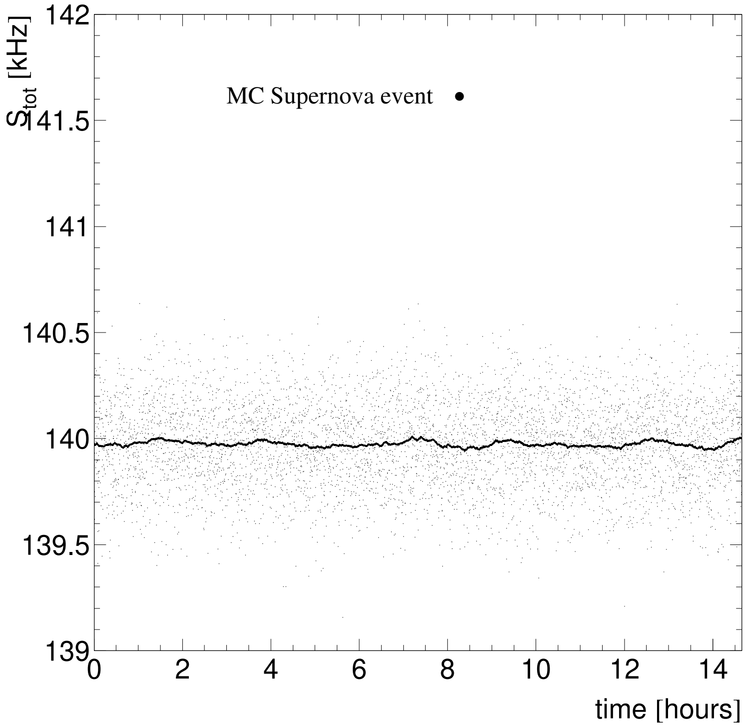

Figure 10.46: $S_{tot.}$ as a function of time for a MC file. In this example a supernova event at a distance of 8 kpc was generated. The MA_{sym} remains stable following the background.

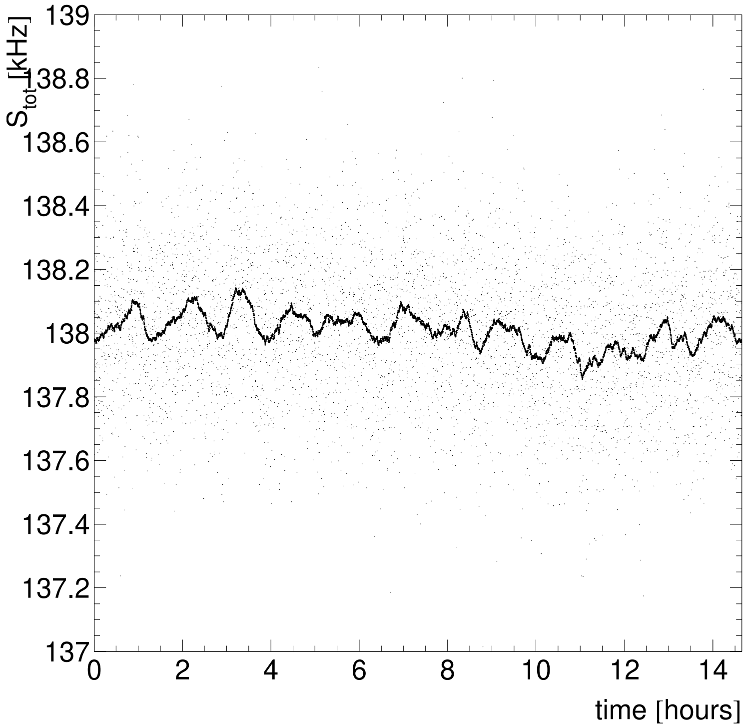

Figure 10.47: $S_{tot.}$ versus time for an example of a stable file. The MA_{sym} has a periodic fluctuation with a period $\sim$ 4000 sec.

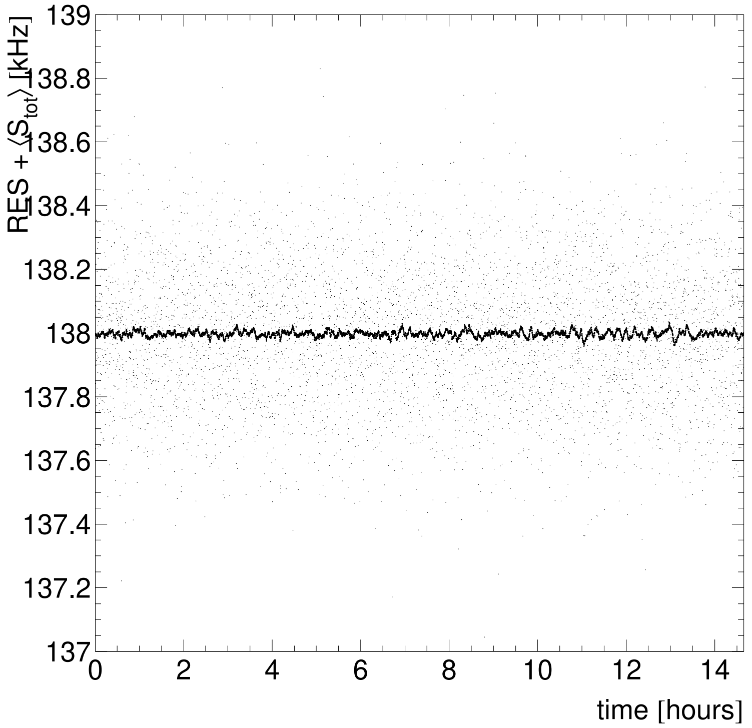

Figure 10.48: Shifted RES versus time. Here the periodic fluctuation in Fig.10.47 is completely removed.

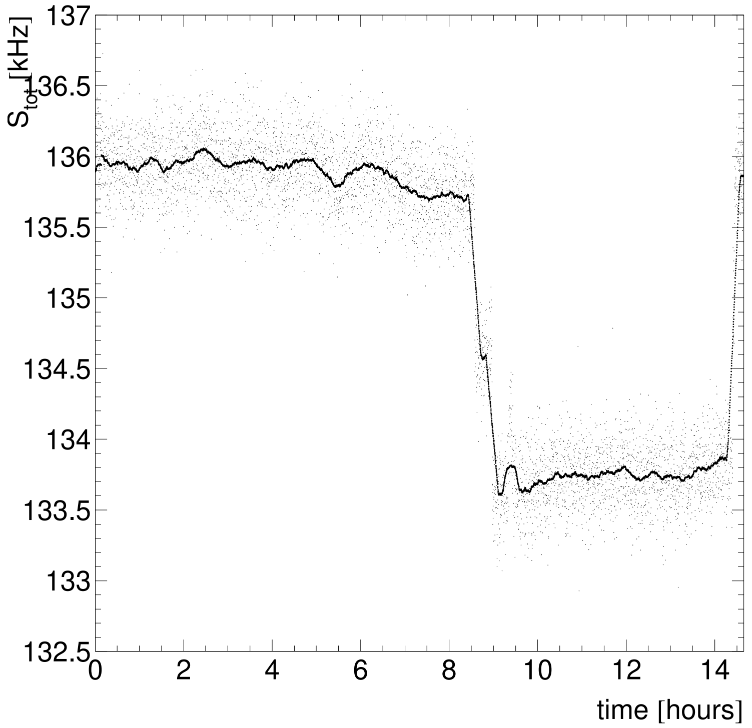

Figure 10.49: Time evolution of S_{tot} for a case of sudden discontinuity.

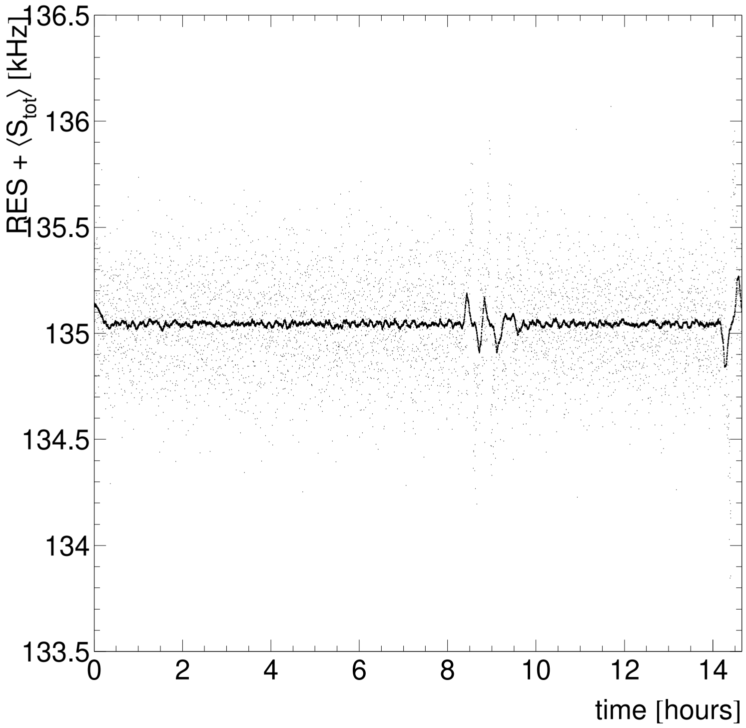

Figure 10.50: Shifted RES versus time. The action of the MA_{sym} removed almost completely the discontinuity permitting to use the file.

10.5 The Maximum-Likelihood Method

There are three classes of events to be distinguished:

1. dark noise background
2. a supernova signal on top of dark noise (i.e. our signal events)
3. all other types of noise (electronics, cross-talk, etc.) disturbing the normal dark noise behavior

The first and second classes can be easily separated by cutting on the value of the summed counting rate S_{tot} (assuming that all PMTs are equivalent) [HJZ94]:

$$S_{tot} = \sum_{i=1}^{N_{\mathrm{PMT}}} N_i^{counts} \tag{10.30}$$

The third class is the problematic one, since it can yield an excess in S_{tot}, which is due to a few unstable channels, rather than to an overall increase of the noise in the detector.
With the aim to remove these improbable supernova candidates, the likelihood of each event can be set up as [Bou]:

$$\mathcal{L}(x_i|\mu_i, \sigma_i, \Delta\mu) = \prod_{i=1}^{N_{\mathrm{PMT}}} \frac{1}{\sqrt{2\pi}\sigma_i} \exp\left[-\frac{(x_i - \mu_i - \Delta\mu)^2}{2\sigma_i^2}\right] \tag{10.31}$$

where x_i is the measured noise of each PMT and μ_i its expectation value –the moving average $MA_{sym}(x_i(t))$ will be used as an approximation. Thus $(x_i - \mu_i)$ is equivalent to the deviation from the moving average and σ_i is the standard deviation for that PMT, assuming a Gaussian behavior. $\Delta\mu$ is the expected excess in the number of counts, if there were a signal (e.g. 100 counts in 10 sec, or 10 Hz per PMT for a supernova at 8 kpc). Instead of the likelihood $\mathcal{L}$ one can use the χ^2 function:

$$\chi^2 = \sum_{i=1}^{N_{\mathrm{PMT}}} \left(\frac{x_i - \mu_i - \Delta\mu}{\sigma_i} \right)^2 \tag{10.32}$$

If excesses are due to a coherent increase of the rate of all channels (as for classes (1) and (2)), $\mathcal{L}$ is expected to be large (or small χ^2 value) for any value of $\Delta\mu$. On the other hand, for events of class (3), often characterized by single outliers or a group of outliers in counting rate, $\mathcal{L}$ is expected to be small or χ^2 large. In this case χ^2 can thus be used to reject such events. The behavior of χ^2/ndf and its fit to the SN 97 data is shown in Fig.11.51, where ndf corresponds to the number of PMTs, N_{PMT} (see Eq.10.32). In the case of classes (1) and (2), the situation is equivalent to repeating a rate measurement N_{PMT} times in order to derive the mean value of $\Delta\mu$. For pure dark noise only one expects $\langle \Delta\mu \rangle = 0$ with standard deviation $\sigma_{\Delta\mu} = \sigma_{PMT}/\sqrt{N_{\mathrm{PMT}}}$.
By minimizing Eq. 10.32, we can solve for $\Delta\mu$:

$$\Delta\mu = \frac{1}{\sum_{i=1}^{N_{\mathrm{PMT}}} 1/\sigma_i^2} \sum_{i=1}^{N_{\mathrm{PMT}}} \frac{1}{\sigma_i} \left(\frac{x_i - \mu_i}{\sigma_i} \right) \tag{10.33}$$

The different characteristics of the individual PMTs are taken into account with the different values of σ_i. The rate excess $\Delta\mu$ is actually measured, which can be used to estimate the distance to the SN, using the prediction for the signal strength made in the following equation (see also Sec.5.4)

$$\Delta\mu = 100 \left(\frac{8\ \mathrm{kpc}}{d} \right)^2 counts \tag{10.34}$$

per OM for a supernova close to the Galactic center, where d is distance in kpc from the supernova to Earth.

11 Analysis Results

11.1 Introduction

Three main programs have been developed which were essential tools for the off-line SN analysis (see also Fig.10.42):
(1) the Main Analysis program produces Ntuples for the PAW analysis;
(2) the statistics program serves for the statistical analysis of each single PMT;
(3) the PMT-FILE Selection program performs data cleaning.
The output of HBOOK-files have been analyzed with PAW, where the chosen cuts were applied to obtain the analysis results. Monte Carlo algorithms have also been developed to predict the SN signal and background and to study the Signal/Noise performance.

11.2 Choice of Efficient Cuts

The residual deviation RES and the fitted $\Delta\mu$ value are the most efficient variables, since they contain the information on the expected excess of the counting rate due to a SN event. To separate the expected SN signal from the dark noise background and noisy disturbances of various nature, efficient cuts on these variables must be applied. The Likelihood function $\mathcal{L}$ will assume a good/large value, if the dark noise background and the Supernova signal on top of it would show a Gaussian behavior. Sudden large fluctuations which are not Gaussian, should give a worse/small value for the Likelihood function $\mathcal{L}$ (large χ^2)

In order to reject noisy events and keep the interesting ones, one rejects high values of χ^2. A fit to the χ^2 distribution of 170 stable PMTs is shown in Fig.11.51 both in logarithmic and linear representation. The fit was computed with the chi-square distribution with ν degrees of freedom

$$f(x,\nu) = \frac{1}{2^{\frac{1}{2}\nu}\Gamma(\frac{1}{2}\nu)} x^{\frac{1}{2}\nu-1} \exp^{-\frac{1}{2}x} \qquad 0 \leq x \leq \infty;\ \nu > 0. \tag{11.35}$$

where Γ is the gamma function, for which $\Gamma(\frac{1}{2}) = \sqrt{\pi}$. The chi-square distribution has a mean value ν and variance 2ν, so that we would expect the degrees of freedom $\nu = 170$. However, al-

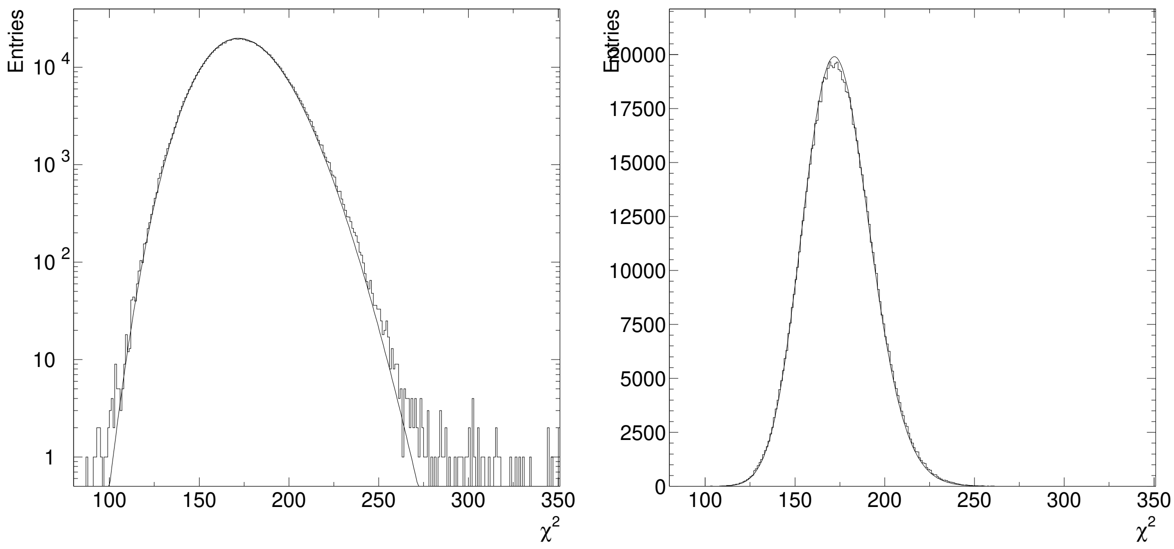

Figure 11.51: Distribution of the χ^2 function according to Eq.10.32, in logarithmic and linear scale. Calculated mean value $\nu = 173.998 \pm 0.002$, with a total number of entries=928783. See the text for further discussion.

though the χ^2 function is fitted rather well, the expected ν does not coincide exactly with the fitted $\nu \sim 174$. Apart from the fact that some "bad" files might have slipped through the data-cleaning procedure, a possible explanation for this disagreement is that the mean value considered for each PMT is the moving average (MA_{sym}), which is correlated to each measurement. A MA_{sym} computed with a larger number of bins should be able to correct for this, with the limitation that over large time periods, trends and slow fluctuations will lower the quality of the MA_{sym}. A simple statistical consideration makes clear that using 100 bins (1000 sec) was not the best choice. In fact the statistical error of the RES, with good approximation, depends inversely on the square root of the number of bins chosen for the TW used to calculate the MA_{sym}, i.e. $\sigma_{RES} \backsim \sigma_{PMT}/\sqrt{TW_{bins}}$.

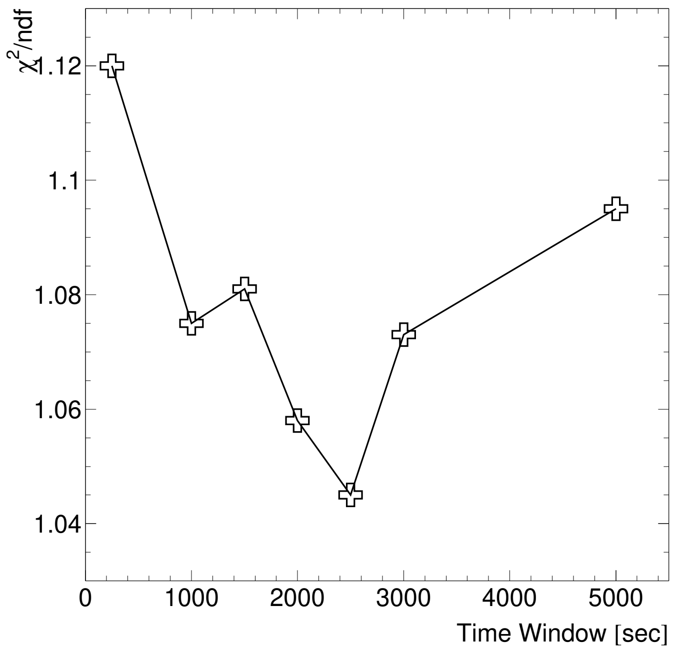

Figure 11.52: χ^2/ndf values from Gaussian fit for the RES distribution versus TW length. Notice that due to statistical reasons the most meaningful choice for TW_{bins} is 250, i.e. 2500 sec.

On the other hand, a too large TW is also not efficient, because it does not remove short-term trends.
A detailed investigation of the "best" time window to chose is given in Fig.11.52, where the χ^2/ndf values from Gaussian fit to the RES distribution versus TW length are plotted. This suggests that the most appropriate value for the moving average time window should be 2500 sec, or 250 bins. The χ^2/ndf value for the smallest TW of 250 sec, or 25 bins, is the largest.

11.3 Behaviour of the Summed Noise (RES and $\Delta\mu$) before Cuts

For the understanding of the behavior of the two variables residual deviation RES and excess in the counting rate $\Delta\mu$, it is useful to plot χ^2/ndf as a function of RES and $\Delta\mu$ as shown in Fig.11.53. Since PMTs of the first 4 strings have much lower noise, results are shown for two PMTs sample: strings 1-4 (51 PMTs) and strings 1-10 (170 PMTs). The ellipse on the bottom of each picture is compatible with the dark noise background of the considered array. Most of the ellipses lay below $\chi^2/ndf \sim 2$. Notice the few points which spread from the bottom left to the top right. These excesses in the counting rate show large values of RES and $\Delta\mu$, and more important large/(bad) values of the χ^2/ndf function. Such excesses can be expected to occur if noisy disturbances due to electronics or other effects of various nature appear, where only a small number of PMTs are suddenly excited. Such events are not interesting for physics and therefore must be cut away. Of course if a supernova occurs during such disturbances, there are no ways to distinguish it. In this case the Likelihood would cut away bad events and "unfortunately" the supernova as well. Nevertheless such periods where the detector is "out of control", are not frequent and their duration is very short, $O(10\ \mathrm{sec})$.
The box drawn in each picture marks the zone where supernova event candidates would be ex-

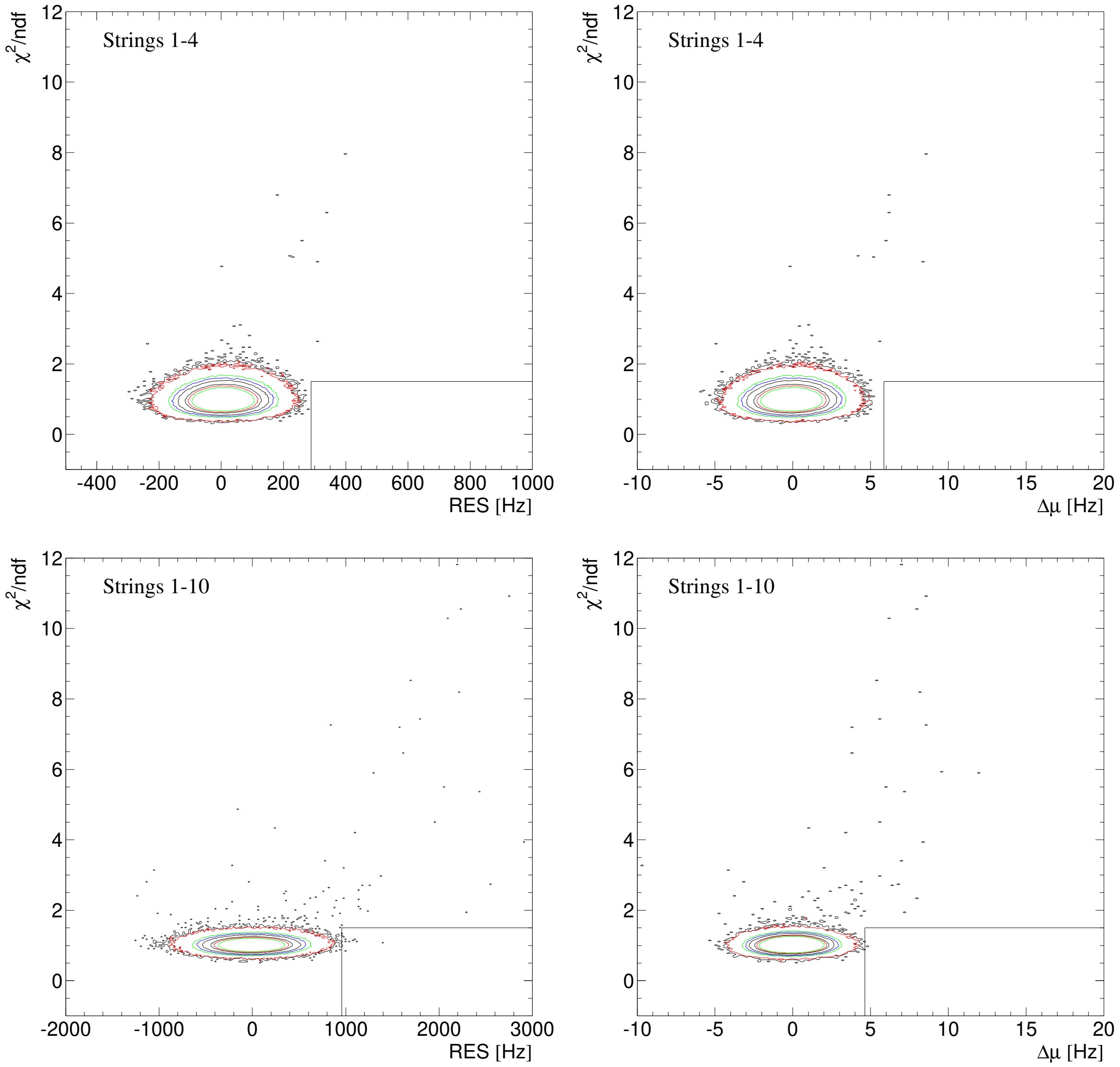

Figure 11.53: Contour plots of χ^2/ndf as a function of residual deviation RES and $\Delta\mu$ (pictures left and right respectively). The first two plots on the top show the results for strings 1-4 (51 PMTs), whereas the two ones on the bottom strings 1-10 (170 PMTs) for data 97 only. The "ellipse" in all pictures represents the dark noise background. The box indicated on the bottom right encloses the zone where candidates for supernova events would be expected due to an excess in the counting rate. Here no cuts have been yet applied, nevertheless the box limits corresponds to the cut on the $\chi^2/ndf < 1.5$, which will discussed in the next section.

pected due to an excess in counting rate in almost all PMTs and at same time a *good/small* value of the χ^2 function. The plot χ^2/ndf versus RES shows several SN candidates inside the box only for strings 1-10. Here the cut values for the box were set to $\chi^2/ndf < 1.5$ and $RES < 958$ Hz which corresponds to an expected SN signal *at* a distance of 8 kpc. Many events are there indicating the "bad" quality of the RES variable to separate potential SN candidates.

The plot χ^2/ndf versus $\Delta\mu$ shows one SN candidate inside the box only for strings 1-10 setting the cut on $\Delta\mu < 4.63$ Hz which corresponds to an expected SN signal *at* a distance of 8.8 kpc (see following section). However, this potential candidate will not further considered as a potential SN neutrino bursts event, since it is required that such an excess must be present for the same event also in the remaining three box both for the variable $\Delta\mu$ and for the smaller strings 1-4 array.

11.4 Results and Cut on the χ^2/ndf Function

The distributions of RES and $\Delta\mu$ before any cut is applied on the χ^2/ndf function can be seen in Fig.11.54 both for strings 1-4 and strings 1-10. Each picture shows a huge dark noise peak. The sample of good PMTs shows a clear Gaussian behavior for the whole year 97. This proves that the selected PMTs are very stable. The few points far from the background distribution indicate noise with large fluctuations, which correspond to the spreading points on Fig.11.53.
The distributions of string 1-4 show only a few of these events, whereas the distributions of strings 1-10 have a long tail, which indicates that the more noisy PMTs of strings 5-10 lead to higher fluctuations. As anticipated, the cut on $\chi^2/ndf < 1.5$ is efficient to remove completely these large fluctuations, leaving a very stable dark noise background distribution (see Fig.11.55). Notice that this cut is more efficient for $\Delta\mu$ than for the RES variable, since for $\Delta\mu$ the differences between PMTs are treated in a statistically more correct way ($\Delta\mu$ is the weighted mean of the observed counting rates). Indeed, after the cut the RES distribution for strings 1-10, are not completely cleaned from "bad" events, which is still showing a distinct candidate. Furthermore the width of the RES distribution depends on the number of PMTs as $\sigma_{RES} \propto \sqrt{N_{\mathrm{PMTs}}}$, since $\sigma_{RES} \propto \sigma_{RMS}$ considering the fluctuation of the noise for the whole array (see Eq.5.26), while for $\Delta\mu$, $\sigma_{\Delta\mu} \propto 1/\sqrt{N_{\mathrm{PMTs}}}$. This explains the broader RES distribution compared with the $\Delta\mu$ distribution. The hardness of the cut is efficient for the $\Delta\mu$ variable, where the corresponding candidate does not appear as excess in the $\Delta\mu$ distribution but rather lies inside the background distribution.
The arrows for the RES distributions indicate the calculated limit prediction for signal events from a supernova like SN 1987A *at* 8 and 6 kpc for 90% detection efficiency. The meaning of these limits will be more clear below, when a rigorous definition of the SN signal *at* a given distance will be given (see Sec.12 and 13). The arrows for the $\Delta\mu$ distribution of strings 1-10 indicate the calculated limit prediction for a rate of one *fake event* per year from a supernova like SN 1987A *at* a distance of 8.8 kpc for 90% detection efficiency. The arrow for the $\Delta\mu$ distribution of strings 1-4 indicates a rate of one fake per year at a distance of 7.9 kpc for 90% detection efficiency.
We presented a first result of the off-line SN analysis 97 data for the strings 1-4 (51 PMTs) [Wis99], where the RES distribution showed a more stable behavior than for all strings 1-10. Considering the $\Delta\mu$ variable from the Likelihood method, the improvement of the results is evident for the combination of all 170 PMTs of strings 1-10 both in long term stability and in limit expectation. The Gaussian fit for the distributions of RES and $\Delta\mu$ show a χ^2/ndf value better than 1.2. After the final cut, the total live-time for the analysis 97 amounts to $\sim$ 107.5 days.

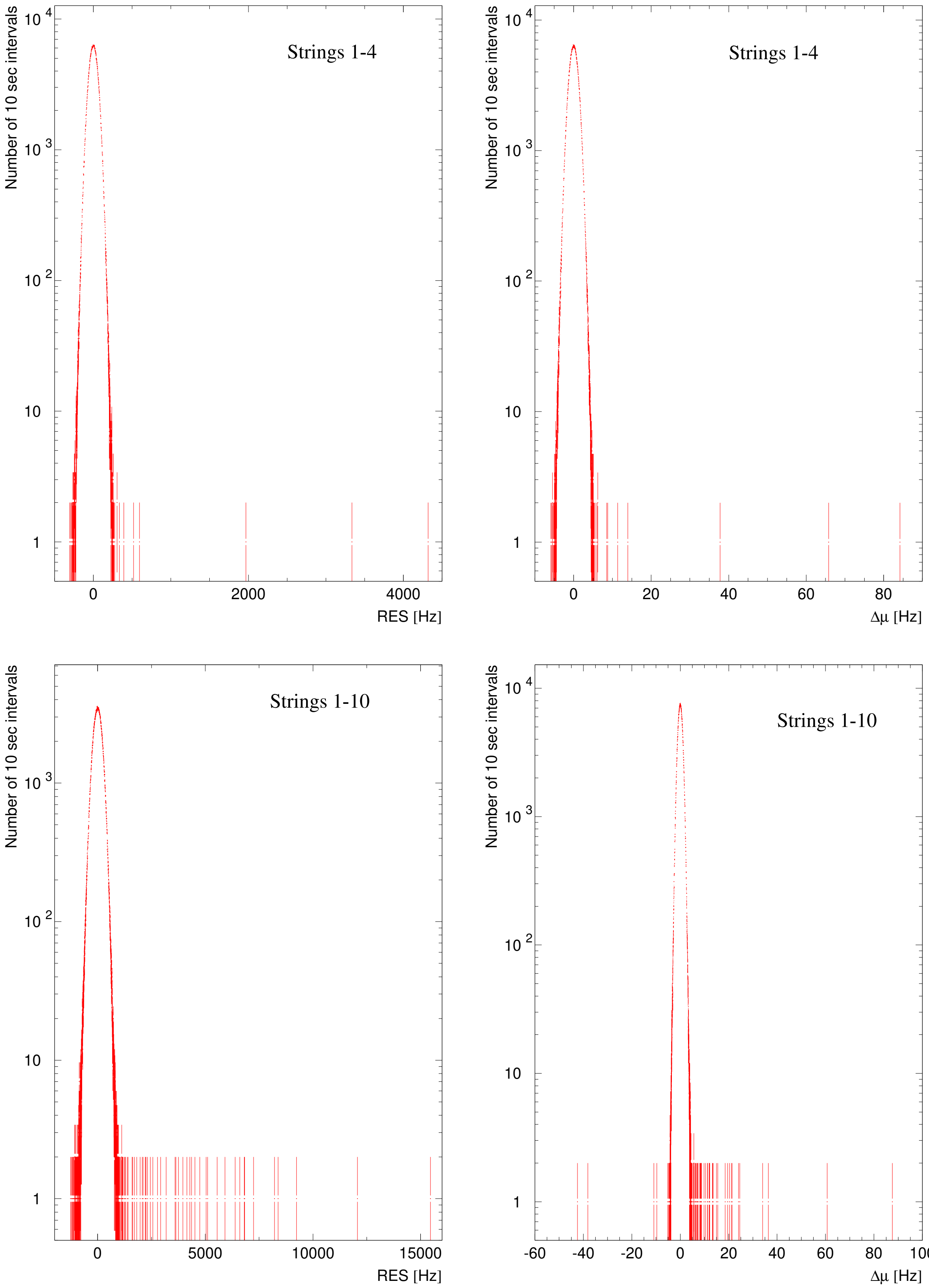

Figure 11.54: Distributions of RES and $\Delta\mu$ for strings 1-4 (top) and strings 1-10 (bottom) for 97 data. No cuts have been applied. The tail of events at the right of the background distribution indicate noise effects of few PMTs.

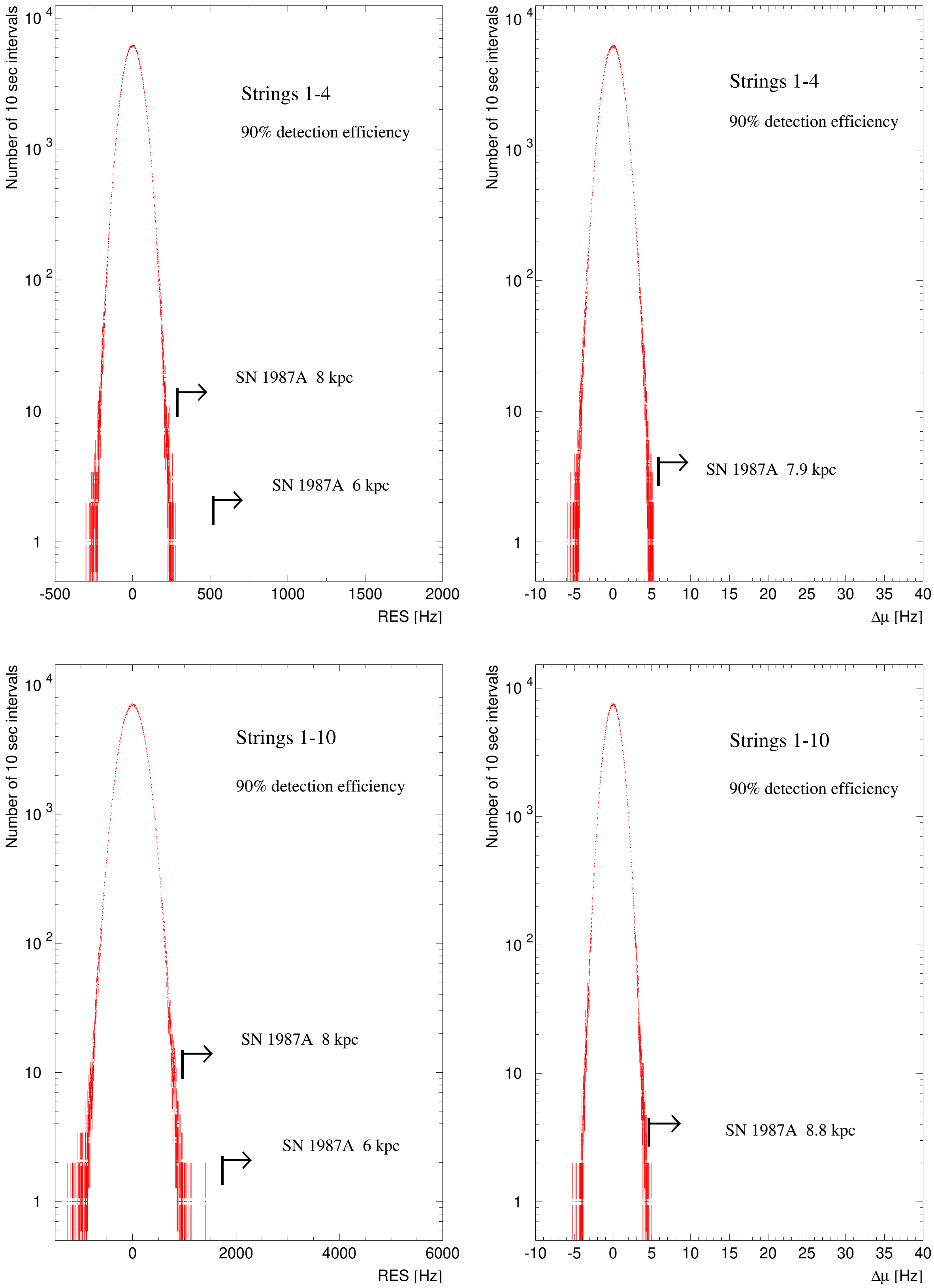

Figure 11.55: Distributions of RES and $\Delta\mu$ for strings 1-4 (top) and strings 1-10 (bottom) after the cut $\chi^2/ndf < 1.5$. The arrows for the two RES distributions indicate the cut limit for signal expectation of supernova *at* 8 and 6 kpc for 90 % detection efficiency. The arrow for the $\Delta\mu$ distribution of strings 1-10 indicates the cut limit for a rate of one *fake event* per year *at* a distance of 8.8 kpc for 90% detection efficiency. The cut limit for the $\Delta\mu$ distribution of strings 1-4 is set at 7.9 kpc.

11.5 Results for the Combined 97 & 98 Data

Once the results of the 97 data were obtained and understood, the off-line SN analysis of the 98 data was performed applying the same programs developed for the 97 analysis. The results do not differ very much from the 97 data, which indicates a constant quality of data during the period of two years. Indeed after the pre-cleaning for "good" files and PMTs, the resulting table of stable PMTs amounts exactly to 170 PMTs as in the analysis 97, where only 11 PMTs differ between the two sample of "good" PMTs 97 & 98. This information is of crucial importance for a future on-line Supernova monitoring, since one can rely on a fixed PMTs table without requiring an additional selection (see Sec.16).
Furthermore, both the average of the counting rate and its standard deviation of each stable PMT were found close to 1997 values: $\langle R_{\mathrm{PMT}} \rangle \sim 300$ and ~ 1100 Hz, and $\sigma_{\mathrm{PMT}} \sim 7$ and ~ 18 Hz for strings 1-4 and 1-10, respectively (see Sec.7.2 and 8.3). So one can conclude that the most important information from the off-line analysis 98 is the stable behavior both of the data, and especially of the same sample of "good" PMTs of data 97. The total live-time of the analyzed data 98 amounts to ~ 111.7 days. The $\Delta\mu$ distribution for the combined results of SN analysis 97 & 98 can be seen in Fig.11.56. A total live-time of 219.7 days have been analyzed after the application of all cuts (pre-cleaning, cleaning, and $\chi^2/ndf < 1.5$).
On the basis of this data, the results for AMANDA-B10 can be summarized as follows: the arrow indicates the calculated limit prediction for a rate of one *fake event* per year with a 90% efficency for a SN 1987A-like supernova *at* a distance of 8.8 kpc. As it will be discussed below, the calculation for this cut limit takes into account only the stars in the Galaxy which lie *at* a given distance neglecting the rest of the stars *within* this distance. Thus to estimate the capability of AMANDA to cover part of the stars in the Galaxy, this information will be taken into account.
A more detailed understanding of the electronics background is needed to fully investigate the two events that lie just above the limits.

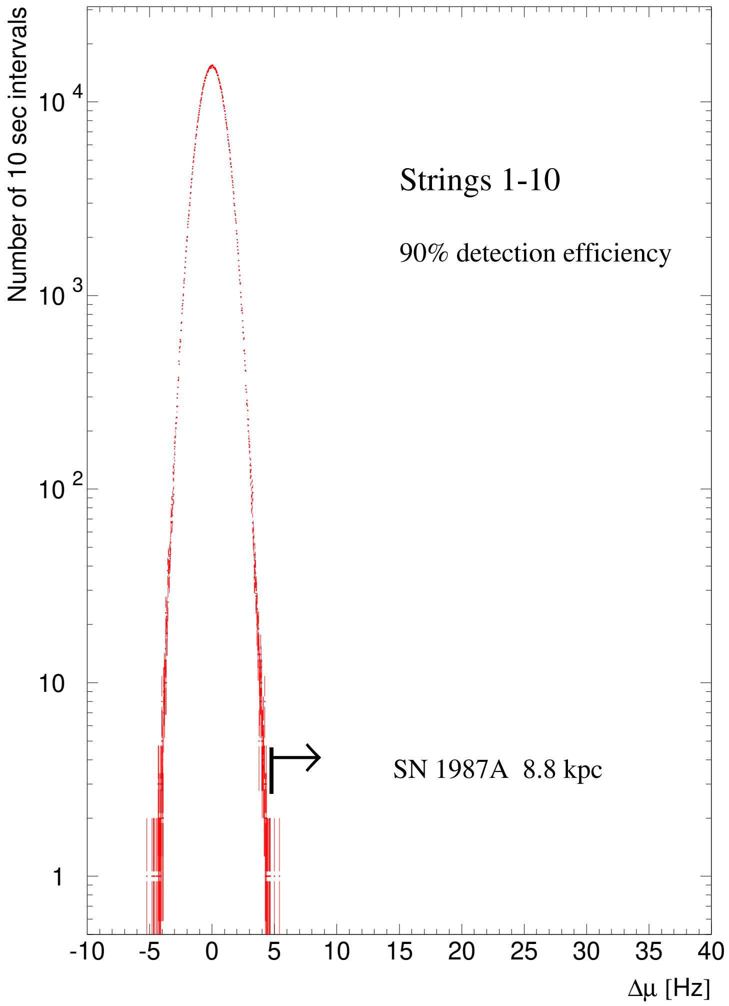

Figure 11.56: Distribution of $\Delta\mu$ for the combined 97 & 98 data. After all cuts a total live-time of 219.7 days have been accumulated. The arrow signs the cut limit for a rate of one *fake event* per year a distance of 8.8 kpc.

11.6 Monte Carlo Comparison

A supernova signal was generated on top of a MC background distribution using the method described in Sec.9.2, i.e. one would consider 100% detection efficiency for the time observation windows. Fig.11.57 shows the MC contour plots of the χ^2/ndf versus RES and $\Delta\mu$ and their distributions. In both pictures the supernova signal can be easily distinguished from the background distribution. A supernova was generated every 1000 sec for a total time of $\sim$ 15 hours. The Monte Carlo simulates a supernova of SN 1987A type close to the Galactic center ($\sim$ 8 kpc), which should induce an excess of $\sim$ 100 counts or $\sim$ 10 Hz in counting rate. Assuming a 100 % efficiency, the signal would sit around the value $RES \sim 1700$ Hz, as the plot shows. The expected $\Delta\mu$ excess due to a supernova does not depend on the number of PMTs $N_{\rm PMT}$. In fact it is sitting around the value $\Delta\mu \sim 10$ Hz, which corresponds to the expected counting rate increase per PMT, only the width of its distribution depends on $N_{\rm PMT}$, $\sigma_{\Delta\mu} \propto 1/\sqrt{N_{\rm PMT}}$.

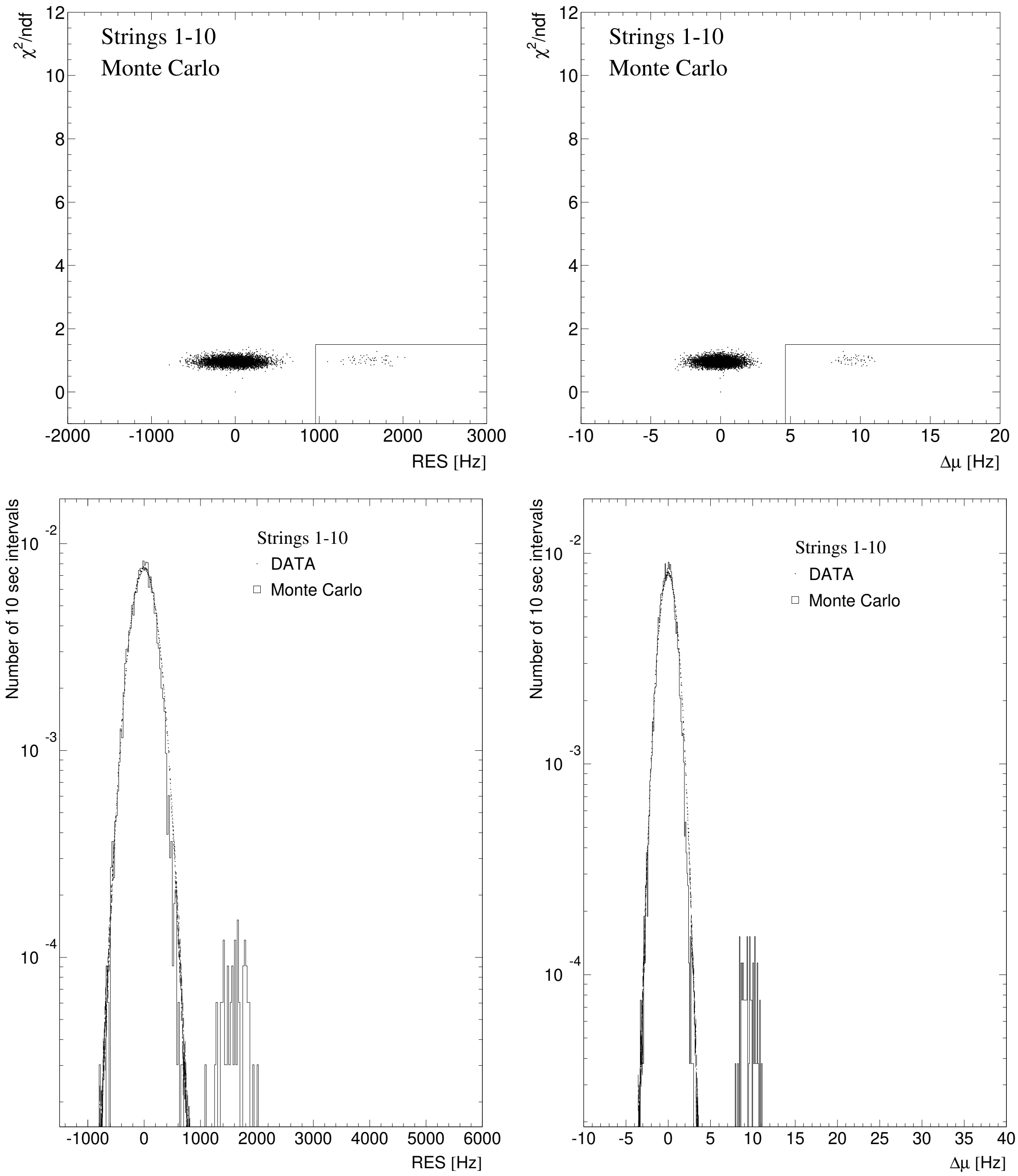

Figure 11.57: (Upper) Contour plots of the χ^2/ndf versus RES and $\Delta\mu$. The larger cluster represents the dark noise background while the smaller one the SN signal (compare with Fig.:11.53). (Lower) RES and $\Delta\mu$ distribution for data and for MC. Note the SN signal separated from the background distribution (see also Fig.11.55). The data distribution were rescaled for a better comparison.

12 Limits and Signal Prediction

12.1 Predicted Event Rate from Neutrino Signal

There are different theoretical models, which predict the expected neutrino signal (see also Sec.2.6). Here a simple model computed by Beacom and Vogel [BV99] was used. The time dependence of the event rate consists of an initial exponential rise with a short time scale ($\tau_1 \backsim 30$ msec) followed by a slower exponential decay with time scale ($\tau_2 \backsim 3$ sec). Fig.12.58 shows the time profile of the expected event rate. Since the adopted counting rate time interval of 10 sec does not resolve the front, a zero risetime ($\tau_1 = 0$) was considered here. Therefore the corresponding normalized event rate can be written as follows

$$f(t) = \frac{1}{\tau_2} \exp\left[-\frac{(t-t_0)}{\tau_2}\right], t > t_0 \tag{12.36}$$

where t_0 is the time of the Supernova burst onset.

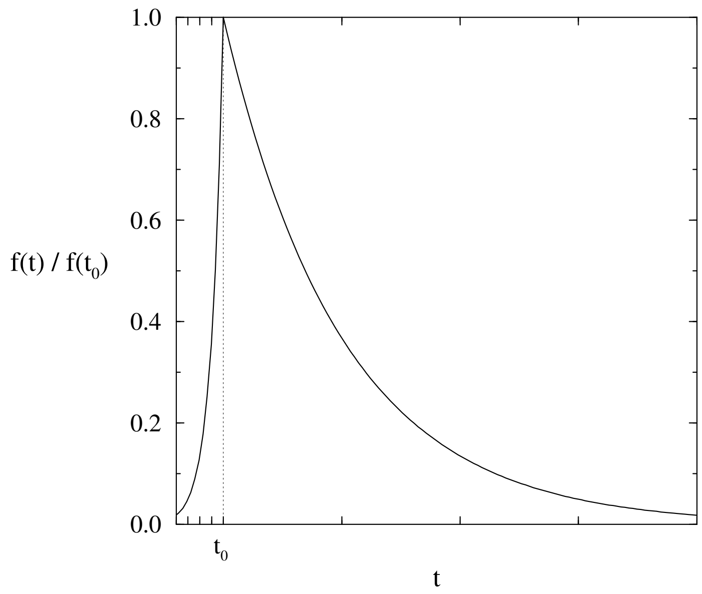

Figure 12.58: Time evolution of the normalized event rate. Notice that 10 sec intervals are not sensitive to the initial exponential rise with time constant τ_1. Therefore we assume a zero risetime. To the right of t_0 there is an exponential decay with time constant τ_2. The tick on the $t-$axis are in units of the respective time constants τ_1 and τ_2. Picture from [BV99].

12.2 The Current 10 sec Sampling Time Interval

The 97 & 98 data have been analyzed with a fixed time interval of 10 sec. This is at the same time an advantage and a disadvantage. The advantage is that the size of the data available from the initial 500 msec sampling time have been reduced by 20, which implied faster analysis results. The fixed time window of 10 sec does not necessarily match the supernova signal, and on the other hand is too long to follow the time evolution of the signal (which would be a more powerful approach). This is due to the fact that the time of the observation windows and the supernova onset are independent variables (see Fig.12.59). The expected supernova signal of 10 sec is artificially distributed over two adjacent 10 sec intervals, so that this signal can be in part lost if one regards only the information locked up in one sampling.
Therefore the detection probability in this case must be calculated taking into account the fact that for each 10 sec time sampling a minimum of ~ 0.5 up to a maximum of 1 of the relative supernova signal can be detected.

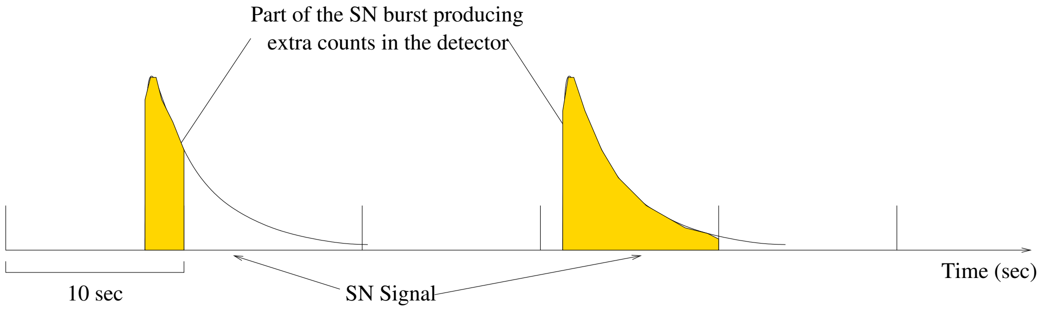

Figure 12.59: Schematic relationship between the fixed location of the observed time window and the occurrence of the supernova onset. This allows us only to be sensitive up to a minimum of 0.5 of the relative SN signal in a given interval.

12.3 Limit Prediction

To calculate the expected detection probability, i.e. the expected relative SN signal at 90% detection efficiency in dependence on the fixed time interval, a Monte Carlo was used [Bou]. It was assumed that the expected time dependence of the event rate follows Eq.12.36. Assuming an excess of 10 Hz in counting rate per PMT (SN at 8 kpc), this excess can be rescaled for supernovae at different distances.
As input parameters the $\sigma_{\Delta\mu}$ and the N_{PMT} are needed, thus the expected excess of the combined signal plus background is calculated in the following way

$$\sigma_{TOT} = \sqrt{\sigma^2_{Back} + \sigma^2_{Sig}} = \sqrt{\left(\frac{\sigma_{PMT}}{\sqrt{N_{PMT}}}\right)^2 + \left(\sqrt{\frac{\langle\Delta\mu\rangle}{N_{PMT}}}\right)^2} \qquad (12.37)$$

considering background and signal statistically independent.
σ_{PMT} and N_{PMT} are the standard deviation for each PMT and the number of PMTs of the detector, respectively. The expected RMS for the $\Delta\mu$ background distribution is $\sigma_{back} = \sigma_{PMT}/\sqrt{N_{PMT}}$, and $\sqrt{\langle\Delta\mu\rangle}/\sqrt{N_{PMT}}$ is the contribution of the signal. With the help of a Monte Carlo calculation the limit predictions can be computed in three distinct steps:

1. Generation of supernova signal following Eq.:12.36
2. The signal has to be smeared with an expected RMS according to Eq.12.37
3. Calculation of the expected relative supernova signal at 90 % detection efficiency taking into account that the observed time window (10 sec) and the supernova onset are independent variables.

Fig.12.60 shows the signal for the $\Delta\mu$ distribution for four different distances. The calculation was performed taking into account a Gaussian smearing of the signal, the inefficiency of fixed 10 sec intervals, and only stars at a given distance $\pm$ 0.1 kpc. The solid line represents the expected signal $\Delta\mu$ value for an efficiency of 90% which indicates the 90% c.l. The fixed interval leads to a sensitivity reduction down to 57% of that for the ideal case, where the signal is made to fall exactly into the 10 sec window.

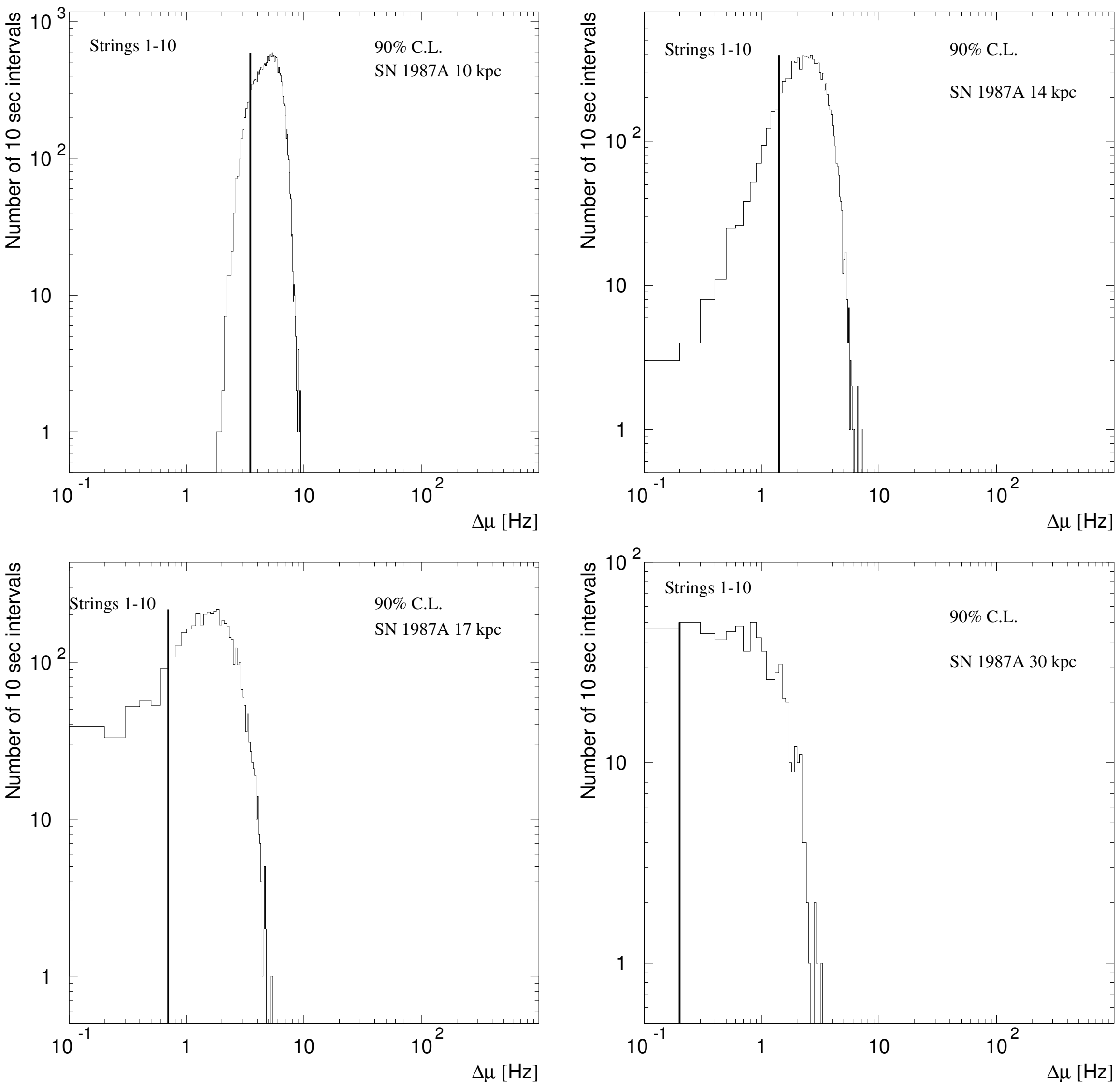

Figure 12.60: Expected signal for $\Delta\mu$ distributions *at* a given distance at 90% c.l. (solid line) according with definition (1) in Sec.13.2. The fixed time window respect to the SN onset occurrence is taken into account. (compare with Fig.13.63).

13 Signal-to-Noise Performance

AMANDA will be operated in a supernova network and should be able to confirm other observations. This aim allows a false alarm rate of typically one per week. In this chapter, the question of signal-to-noise (S/N) rate, where signal is a true SN-event and noise a false event will be discussed. We will see that S/N $=1$ is better than what one needs when the detector is operated in a network. The results give a good feeling for how the performance of the detector improves with an increasing number of PMTs and with decreasing noise rates.

13.1 Star Distribution in the Galaxy

To calculate the ratio S/N ratio, one has to answer two questions:

1. What is the fraction of supernovae in the Galaxy within the visibility range of our detector?
2. How often do stellar collapses occur?

Notice that actual Supernovae (optically bright) must not be confused with the occurrence of stellar collapses. Stellar collapses are optically faint, but potential neutrino "bombs", since neutrinos carry away almost the total energy (Type Ib and II), while optically bright Supernovae (Type Ia) are not important neutrinos producers. To answer the first question, the results of the Galaxy model computed by Bahcall and Soneira have been used [BS80], which describe the expected distribution of stars in our Galaxy. The star density in the Galactic disk, ρ_d is expected to be:

$$\rho_d(x, z, M) \approx \exp[-z/H(M) - (x - r_0)/h] \tag{13.38}$$

where r and M are the distance from the Sun and the mass of the star, respectively. The variables z and x are the transversal and perpendicular coordinates in the Galactic plane. r_0 is the distance of the Sun from the Galactic center, $H = 352$ pc the scale height and $h = 3.5$ kpc the scale length [BS80].

A more elaborated version of the model in Eq.13.38 describes the expected fraction $F(r)$ of potential SN progenitor stars in the Galactic plane, that lie within a distance r of the Sun [BP83], as is shown in Fig.13.61 left. The fraction $F(r)$ is the probability distribution within a given distance of stellar collapses in the Milky Way. This answers the first question. The scatter plot in Fig.13.62 gives an idea how the approximation with the exponential function in Eq.13.38 for the stellar distribution in our Galaxy looks, neglecting the perpendicular contribution ($z = 0$). The derivative of $F(r)$ is shown in Fig.13.61 right. It is the star density distribution starting from the location of the Sun, as illustrated schematically in Fig.13.62. The huge peak around distance 9 kpc represents the dense cluster of stars enclosed in the Galactic bulge. However the central bulge has a diameter of

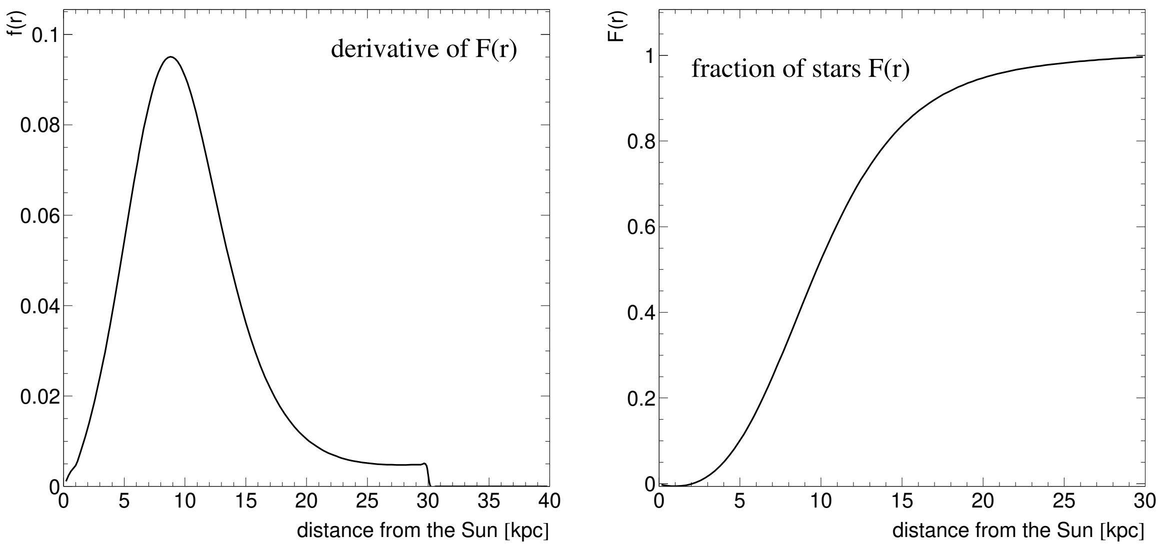

Figure 13.61: (Left) Derivative function of the fraction of stars $F(r)$ within a distance from the Sun in the Galactic plane. The zero correspond to the Sun position and the huge peak represents the high star density within the Galaxy bulge. (Right) Fraction of Galactic stars $F(r)$ for the distance in kpc according with the model by Bahcall & Piran [BP83]. From that distribution it is easy to see that 90% of stars are enclosed within 17 kpc.

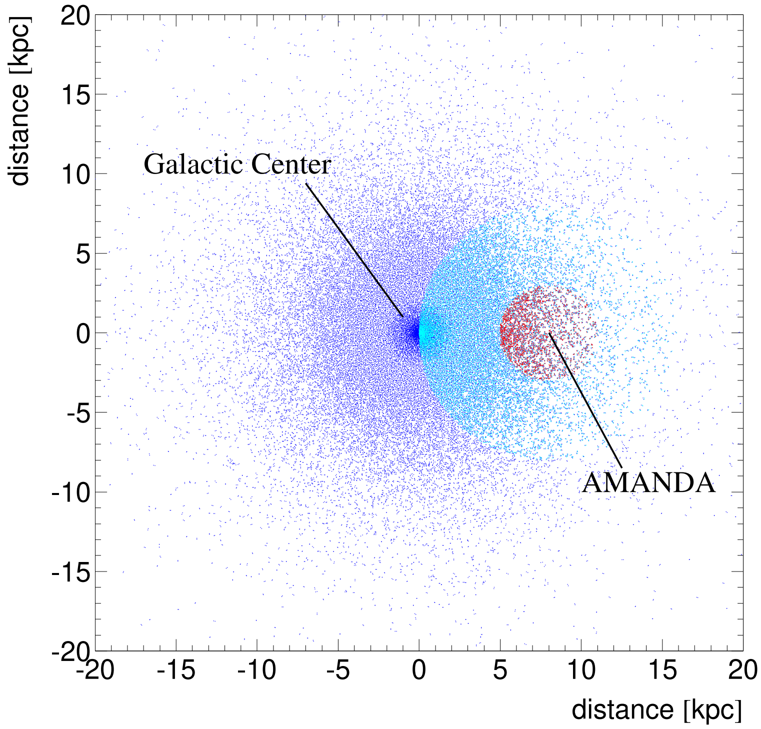

Figure 13.62: Schematic scatter plot of star distribution in the Galaxy. The distribution was generated with a MC following Eq.13.38. Visibility radii of 3 and 8 kpc around AMANDA are indicated.

2 kpc only (4% of the diameter of the Galaxy) [CO96], more than 20% of all stars are contained in its spheroid. The function decreases fast up to 17 kpc then drops at the edge of the Galaxy at ~ 30 kpc from the Sun.
The question about the frequency of stellar collapses is more difficult to answer due to the large uncertainty in the input data of different models. Some estimates for the rate of Galactic Type II supernova are in the range of 1 per 30 years to 1 per 80 years [Bah89]. A recent estimate [TLS94] gives a rate of 1 SN per 47 ± 15 years, (2.1 ± 0.7 per century, see also Sec.2.8). The most conservative estimates are 1 SN/11 years [Bah89] and 1 SN/100 years [Suz94].

13.2 Signal-to-Noise and Final Results

At this point it is important to clarify the detector performance with two rigorous definitions:

1. AMANDA has a visibility radius of 8.8 kpc, since this is the distance which corresponds to a cut on $\Delta\mu$ when one requires that the fake rate should be one per year (see Fig.11.56).

2. AMANDA is sensitive *within* a distance of 10 kpc to 50% of the stars in the Galaxy with a S/N$\geq$ 1 when for SN signal "all" stars from 0 to 10 kpc are taken into account according to the fraction of stars in our Galaxy given in Fig.13.61.

The strict meaning of these two different definitions can be better understood comparing the figures 12.60 and 13.63. The limits calculated for SN signal *at* a given distance at 90% c.l. shown in Fig.12.60 correspond to definition (1), and with the same definition the limits for the rate of one

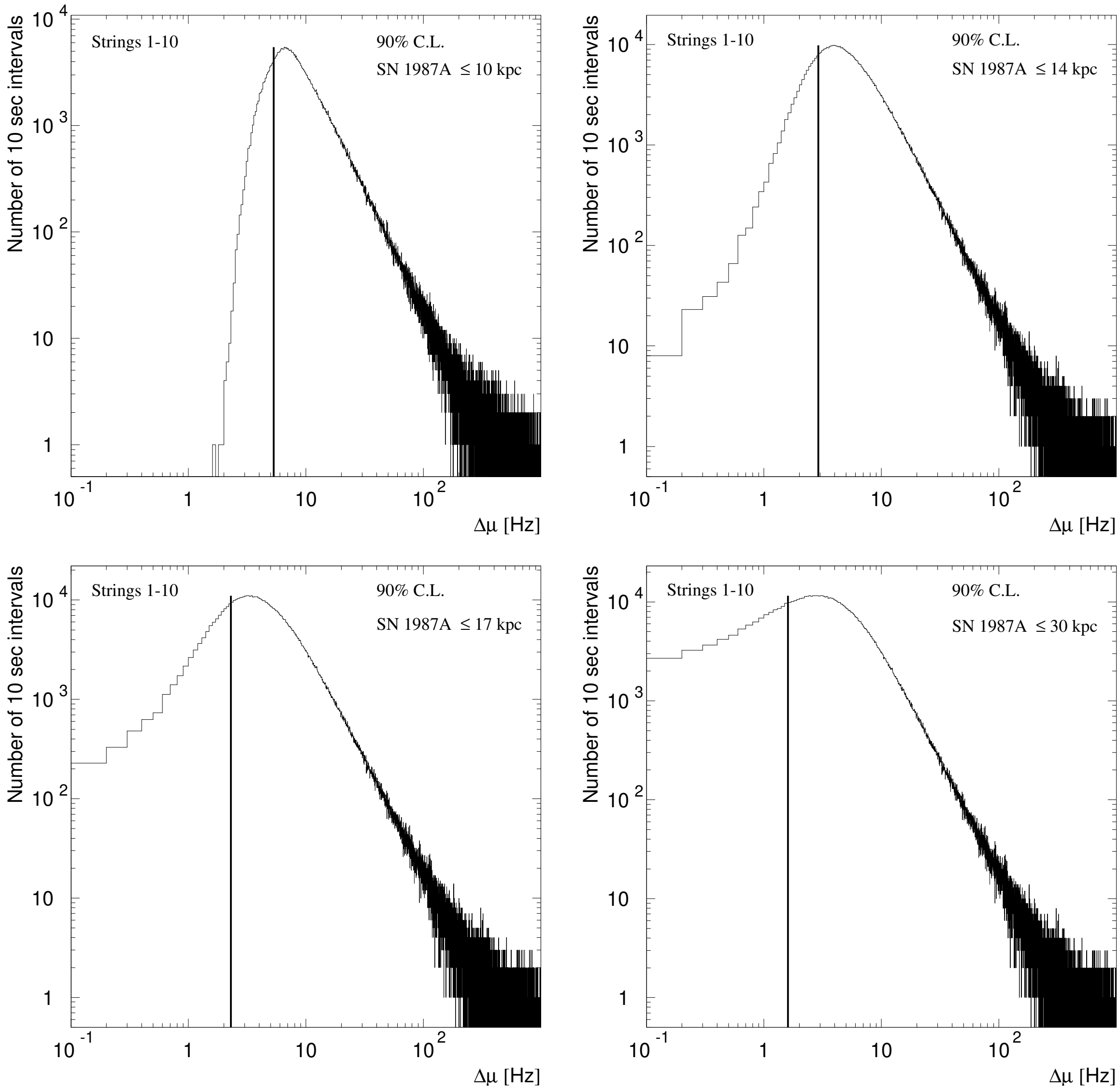

Figure 13.63: Expected signal for $\Delta\mu$ distributions *within* a given distance at 90% c.l. (solid line) according with definition (2). The dominant contribution to the signal is given by the closer stars as show the long tail of each distribution, note that the x-axis is in logarithmic scale (compare with Fig.12.60).

fake event per year given in Fig.11.55 were calculated. Fig.13.63 show the limits calculated for a SN signal *within* a given distance at 90% c.l. corresponding to definition (2).
It is important to note that the closer stars within a given distance give the most important contribution to the signal, as shown by the long tail in each distribution in Fig.13.63. According to definition (2) the ratio S/N can be calculated as follows.
Signal S is the frequency of gravitational stellar collapses according with the fraction of stars in our Galaxy given in Fig.13.61, assuming 1 SN per century.
Noise N is the number of fake events per century for a 1987A-like SN within a given distance.
Fig.13.64 shows the ratio S/N as a function of the distance from the Sun in kpc, for strings 1-4 (51 PMTs) and strings 1-10 (170 PMTs). Strings 1-10 are able to cover 50% of the stars in the Galaxy (within 9.8 kpc) with a S/N$\geq$ 1, whereas strings 1-4 cover 39% of the Galaxy (within 8.6 kpc) with a S/N$\geq$ 1. The increment of more than 10% of the stars with a difference in the visibility range of

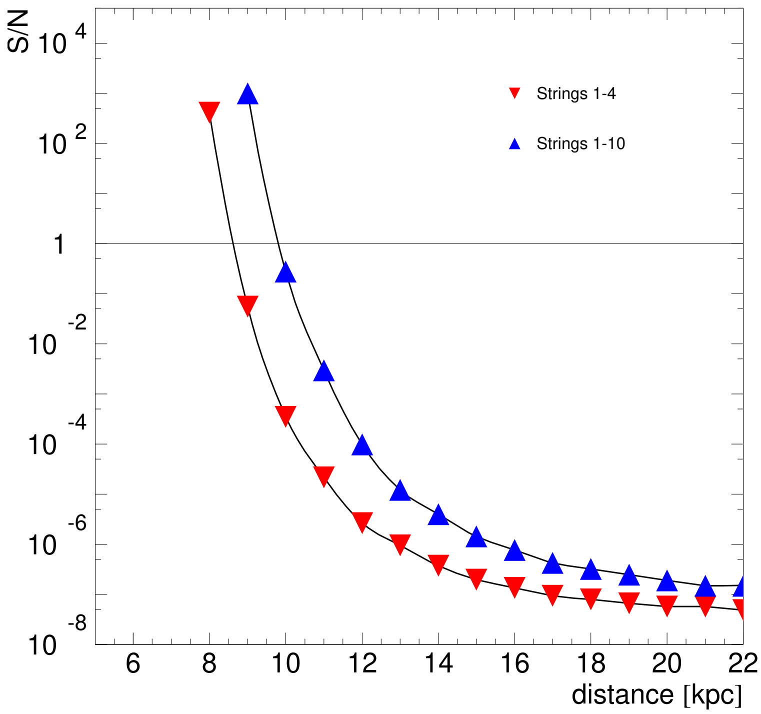

Figure 13.64: Ratio S/N as a function of distance from the Sun for strings 1-4 (S/N $\geq$ 1 within 8.6 kpc, i.e. 39% of the Galaxy) and strings 1-10 (S/N $\geq$ 1 within 9.8 kpc, i.e. 50% of the Galaxy) S/N= 1 corresponds to a cut at $\Delta\mu = 5.5$ Hz for AMANDA-B10.

$\sim$ 1 kpc between the two detectors is due to the very steep behavior of the curve in Fig.12.60 in the range of 7 and 14 kpc, where the density of stars is the highest.
Fig.13.65 left shows the ratio S/N as a function of the distance for other hypothetical detector configurations with 250, 500, 700 and 800 PMTs, assuming 300 Hz dark noise rate. Fig.13.65 right shows the same array configurations, but with the only difference that here a dark noise rate of 1100 Hz was considered. From the plots can be seen, that an array upgraded with 800 PMTs of noise rate at 300 Hz is able to cover the entire Galaxy, whereas a corresponding array with PMTs with 1100 Hz noise rate can hardly reach 13 kpc, i.e. 70% of the Galaxy. Increasing the number of PMTs by a factor four (i.e. 3200 PMTs with 1100 Hz noise rate), the performance of such an array could reach a distance within 22.8 kpc, whereas an array with 4000 could survey within a distance of 27.8 kpc. The S/N performance of each detector version depends on

1. the assumed Galactic collapse rate,
2. the frequency of fake events.

For the first point, the range of the different collapse rate estimates mentioned above ($D_{Galaxy} \backsim 1/11$ yr, $1/47$ yr or $1/100$ yr) influences the S/N performance only slightly. In fact considering the strings 1-10 detector, S/N = 1 would correspond to 9.8, 10.1 and 10.5 kpc for a collapse rate of 1 every 100, 47 and 11 years respectively. The reason for this small difference can be understood directly from Fig.13.64. The different collapse rates will result in a small shift of all curves upwards, and since they are very steep, the corresponding horizontal shift is small.
The second point, is the topic of the next section.

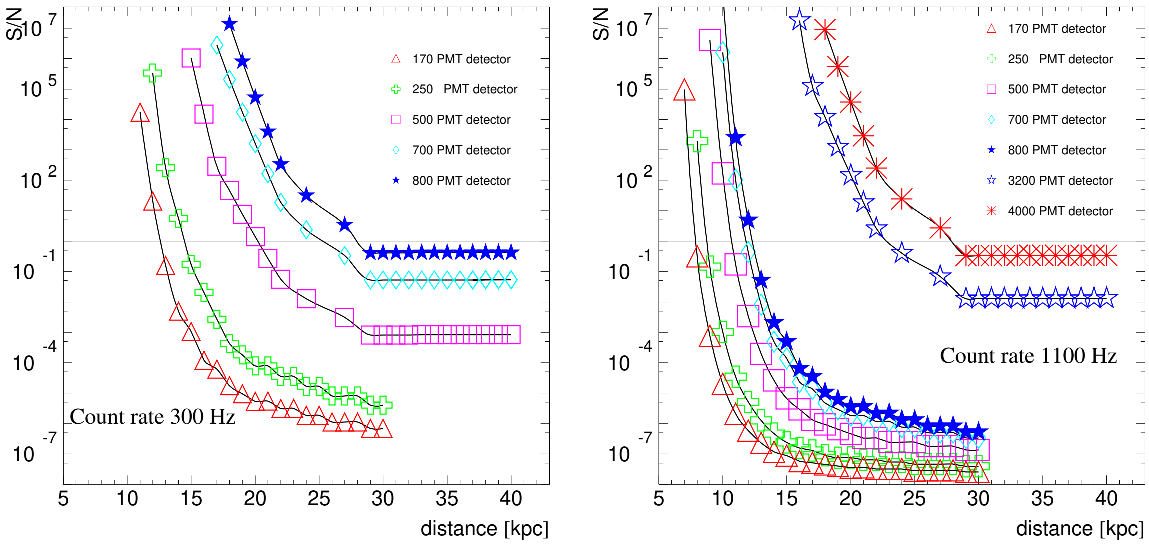

Figure 13.65: S/N versus distance for larger detector versions. Signal: 1 Galactic SN per century; Noise: number of fake events (per century) in dependence on each detector version. (Left) Predictions for arrays assuming a count rate of $\sim$ 300 Hz, (Right) predictions for the same number of PMTs assuming a count rate of $\sim$ 1100 Hz.

13.3 Detector Performance

Fig.13.66 shows the expected number of PMTs which are required for S/N$\geq$ 1 as a function of visibility distance. The difference in the noise rate affects directly the quality and the performance of the detectors. Whereas a low-noise detector like strings1-4 would need roughly 400 PMTs to cover 90 % of the whole Galaxy, and therefore to reach 90% of probability to see the next Galactic stellar collapse, a detector constructed with PMTs with a noise rate of $\sim$ 1100 Hz like strings 5-10 would need more than 1500 PMTs to achieve the same performance.

A future upgrade of AMANDA with roughly 800 low noise OMs could monitor distances up to $\sim$ 28 kpc which is enough to cover the entire Galaxy. Fig.13.66 proves that for very close distances the performance of the detector increases quickly with the number of PMTs. In fact the number of PMTs needed for a fixed S/N ratio scales roughly with the distance to the fourth power. This assertion is based on the fact that the signal is proportional to the number of PMTs ($S \propto N_{PMTs}$) and the noise to their square root ($N \propto \sqrt{N_{PMTs}}$). Furthermore the signal is also inversely proportional to the square of the distance ($S \propto d^{-2}$). So writing S/N= $1 \propto \frac{N_{\rm PMT}}{\sqrt{N_{\rm PMT}} \cdot d^2}$ gives $N_{PMTs} \propto d^4$. The curve saturates at large distances due to the finite size of the Galaxy.

13.4 Conclusion and Discussion

Although the rate of stellar collapses is not very well known, it affects the relative performance of the different detector versions only marginally. The effect of dark noise is important, a counting rate of $\sim$ 1100 Hz in each optical module reduces the performance of the same detector with a PMT rate of $\sim$ 300 Hz by more than a factor four.

Presently with the 170 stable PMTs of strings 1-10 the search for neutrino bursts extends to over 50% of the stars in the Galaxy (i.e. *within* 9.8 kpc with a S/N $\geq$ 1). A future upgrade of AMANDA to a 800 PMT detector would reach a distance of $\sim$ 28 kpc covering the whole Galaxy, if its optical

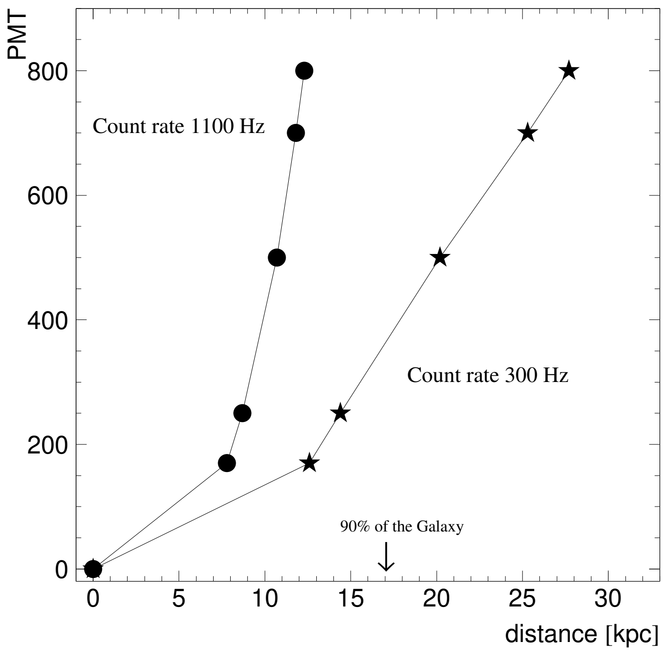

Figure 13.66: Predicted PMT number as a function of distance for a constant S/N= 1. The two curves represent arrays with PMTs like strings 1-4 ($\sim$ 300 Hz) and strings 1-10 ($\sim$ 1100 Hz).

modules would have a noise rate of $\sim$ 300 Hz.

14 Upper Limit on the SN Rate in the Galaxy

Upper limits on the rate of Galactic stellar collapse are available from several of these experiments. To estimate the 90% confidence level upper limit for Galactic supernova rate Φ, the following expression can be used

$$\Phi = \frac{\mu_{Poi}}{\Delta t} \cdot \frac{1}{\epsilon \cdot \eta} \tag{14.39}$$

where $\mu_{Poi} = 2.3$ is the mean value of the Poisson probability distribution at 90% c.l. to detect zero events. Δt is the corresponding live-time of each single experiment, and ϵ and η represent the detection efficiency and the percentage of the Galactic visibility (see also Fig.13.61).
On the basis of the 220 live-time days 1997 & 1998 the AMANDA upper limit on the rate of gravitational stellar collapses for 90% c.l. is

$$\Phi_{AMANDA} < 8.59 \; events \cdot year^{-1} \tag{14.40}$$

At the beginning of the nineties the best available limit was provided by the Baksan Underground Neutrino Observatory, a scintillation detector which operated for a total live-time of 5.5 years without seeing supernova candidates [Bah89]. Recently the LVD collaboration published a new upper limit during 2033 days of operation providing $\Phi < 0.4\ \mathrm{yr}^{-1}$ [LVD99]. Note that the AMANDA result for Φ is worse compared to other experiments. However scaling these limits to the large live-time of the LVD experiment (see third row in Tab.14.3), the result of AMANDA is only a factor 2 away from LVD, Super-K and Baksan:

$$\Phi_{AMANDA_{scaled}} < 0.93 \; events \cdot year^{-1} \tag{14.41}$$

Considering that since 1984 [Man97], at least one detector observing the whole Galaxy was operating with 100% detection efficiency, a compilation of all data should yield a limit of about $\Phi < 0.15$ yr^{-1}. Such a compilation, however, is beyond the scope of this work.
Tab.14.3 summarizes the published information for MACRO [Ahl92], LVD [LVD99], Kamiokande [Suz93], SuperKamiokande [Fuk98], Baksan [Bah89] and the present AMANDA results.

Performance	AMANDA	MACRO	LVD	Super-K Kamiokande	Baksan
Φ (yr^{-1})	8.59	-	0.40	0.54	0.42
Live-Time Δt (yr)	0.60	2.1	5.57	4.26	5.5
scaled Φ (yr^{-1})	0.93	-	0.40	0.41	0.41
max. distance (kpc)	9.8	11	30	40	30
Detection eff. ϵ (%)	90	73	80	100	100
Gal. visibility η	0.50	0.62	1	1	1

Table 14.3: Upper limits Φ and corresponding performance of different experiments during the period of their published SN off-line analysis.

Assuming 10 years live-time of AMANDA at $\epsilon = 90\%$ and $\eta = 0.50$, and considering the frequency of Galactic core collapse supernovae (Type II and Ib) recently estimated [TLS94], (2.1 ± 0.7 per century), the probability that AMANDA could observe a supernova is 9% .
In Tab. 14.4 and 14.5 are summarized the different techniques in use for SN detection and the capabilities of different SN neutrino detectors.

Detector type	Material	Energy	Time	Point	Flavor
scintillator	C,H	y	y	n	$\bar{\nu}_e$
water Cherenkov	H_2O	y	y	y	$\bar{\nu}_e$
heavy water	D_2O	NC:n CC:y	y y	n y	all $\nu_e, \bar{\nu}_e$
long string water Cherenkov	H_2O	n	y	n	$\bar{\nu}_e$
liquid argon	Ar	y	y	y	ν_e
high Z/neutron	NaCl, Pb, Fe	n	y	n	all
radio-chemical	^{37}Cl, ^{127}I, ^{71}Ga	n	n	n	ν_e

Table 14.4: Different SN detector types. Table from [Sch99].

Detector	Type	Mass (kton)	Location	# events at 10 kpc
Super-K	water Cherenkov.	32	Japan	4400
MACRO	scint.	0.6	Italy	150
LVD	scint.	0.7	Italy	170
SNO	H_2O D_2O	1.7 1	Canada	350 430
AMANDA	long string	$M_{eff} \sim$ 0.41/PMT	Antarctica	64 per PMT

Table 14.5: Capabilities of supernova neutrino detectors, following [Hab99]. The 64 events/PMT by AMANDA have to be interpreted as excess over the dark noise background of the PMT. Note that the visibility distance is not proportional to the detector mass, see Tab.14.3

15 Integration in a World Wide Supernova Network

15.1 Supernova Early Warning System (SNEWS)

SNEWS (SuperNova Early Warning System) is an international project of several detectors located around the world able to detect Galactic supernova explosions. The main purpose of SNEWS is to observe the neutrino burst from a Galactic gravitational core collapse in advance to its incoming photon burst. As discussed in Sec. 2.5.8, theoretical models of gravitational core collapse predict that neutrinos are able to escape from the inner dense core due to their small cross section, while photons are trapped within the star for hours up to one day [Bur90]. The SNEWS project will search for coincidences of the supernova signal providing by different detectors (see Tab. 14.4). A

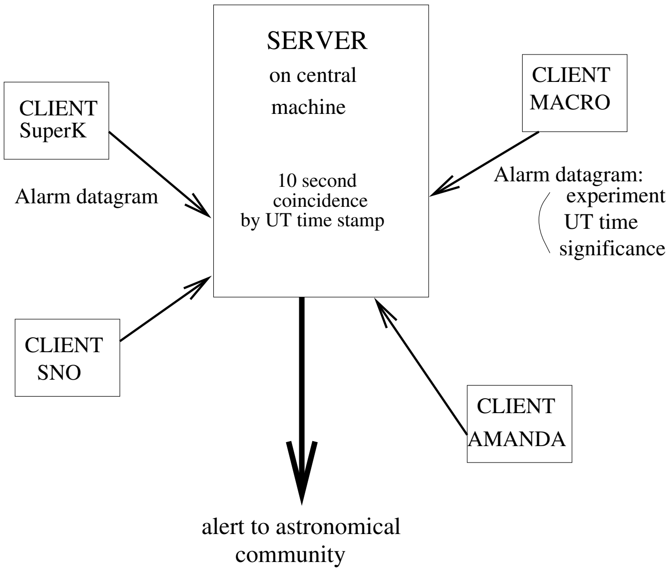

Figure 15.67: Schema for combining the information of different experiments, and sending an early alert to the astronomical community. Figure from [HSV98].

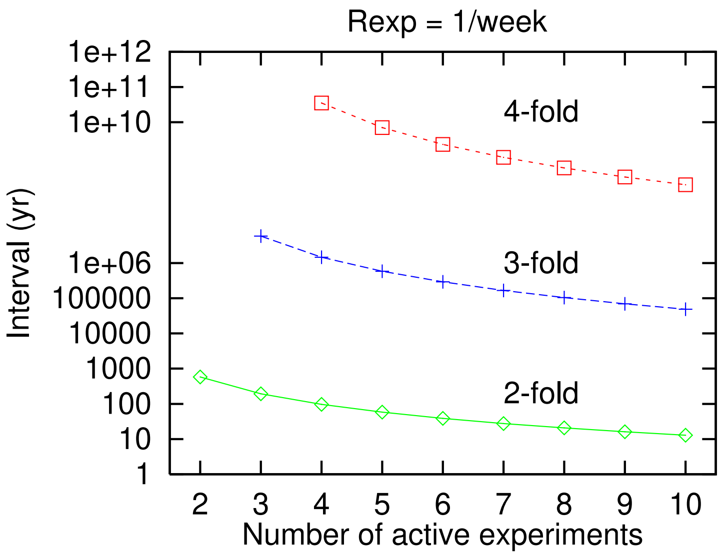

Figure 15.68: Average time between accidental coincidence alarms in different experiments as a function of number of online experiments. Here was assumed: (1) same alarm rate for all experiments; (2) Alarm Poisson distributed; (3) No correlation between different experiments; (4) supernova monitoring without interruption. Figure from [Hab99]

supernova network combining different experiments has several advantages compared to individual detection monitoring:
(1) More sensitivity to weak SN signals; (2) Suppression of Non-Poissonian background present in each single detector; (3) Automated alert decision without human control [HSV98]. At the moment only MACRO [Amb98], SuperK [OYI$^+$94] and LVD [Hab99] have online supernova monitors and are connected to the SNEWS network (see also Tab. 15.6).
A fundamental task is to maintain a very low rate of false alarms sent to the astronomical community. Considering 1 false alarm per century as an acceptable rate, one can estimate how low the

Detector	Alarm interval	Est. resp. time	Network connection	Time stamp	Status
Super-K	1-2 wk	40 min	good	$<$msec	online in SNEWS
MACRO	2-3 wk	20 min	good	$<$msec	online in SNEWS
LVD	10 d	short	good	$<$msec	online in SNEWS
SNO	-	short	good	$<$msec	running
AMANDA	$<$1 century (9.8 kpc)	short	50% coverage	0.5 sec	running

Table 15.6: Current monitoring capabilities of AMANDA and other experiments. The first three experiments are both online monitors and provider of SNEWS input, whereas SNO and AMANDA are running and will become soon online monitors. “Alarm interval”: time interval that occurs between two consecutive false supernova alarms due to the background of each experiment. “Estimated response time”: time interval which occurs between the actual supernova explosion and the sending of the alarm to the central server machine. (Info. of other exp. from [Sch98]).

false alarm rate has to be for each single detector [HSV98]. In Fig.15.68 a coincidence within a 10 sec time window and an individual alarm rate of $R_{exp} = 1$/week for each experiment was assumed. From Fig.13.64 we saw that the current status of AMANDA is able to see Galactic supernovae within a distance of 9.8 kpc for an expected false alarm rate less than 1 per century. For AMANDA the network connection is reduced by satellite time coverage on the South Pole (presently 50%).

15.2 Localization of a Supernova

There are two different methods to achieve a backtracking to a supernova.

1. The angular dependence of the forward-peaked neutrino-electron scattering.
2. The triangulation between at least two detectors separated by a distance d.

For the first case, the angular distribution of the reaction products of Eq.2.15 is directly correlated to the incoming neutrino direction (see also Par.2.9.2). Assuming that the one-sigma angular width of the Cherenkov cone is $\delta\alpha \backsim 25^\circ$ [BV99], then the uncertainty of the direction can be estimated as

$$\delta\theta \backsim \frac{\delta\alpha}{\sqrt{N_S}} \tag{15.42}$$

where θ and N_S are the best value-fit for the direction angle and the total number of detected events respectively. Detectors which can give a good angular resolution through the elastic νe^- scattering are SK and SNO. Their pointing accuracy are estimated to be $\delta\theta \backsim 5^\circ$ and $\delta\theta \backsim 20^\circ$ for an expected number of events $N_S \backsim 320$ for SK and $N_S \backsim 25$ for SNO respectively [Bea98, BV99]. The AMANDA detector, because of its larger threshold energy, cannot detect individual events and can yield neither energy nor angular distribution from such reactions. However, AMANDA might be useful for triangulation method.

The principle of triangulation is to point back to a supernova using the relative arrival time at different detectors. This requires a network of detectors and accurate time resolution. The angle between the base line (A-B axis, in Fig.15.69) of the two detectors and the supernova can be determined measuring the arrival time delay Δt of the neutrino signal and d as follows

$$cos\theta = \frac{c\,\cdot\,\Delta t}{d} \tag{15.43}$$

The corresponding error in the registration time $\delta(\Delta t) \equiv \delta t$ will affect directly the determination of the angle with an error $\delta(cos\theta) = c\,\cdot\,\delta t/d$. Therefore in order to achieve a reasonable pointing accuracy from the triangulation, one must have $\delta t << d/c$. The equivalent triangulation error can be written as follows [BKG92]

$$\delta\theta \sim \left(\frac{\delta t(10\text{ kpc})}{2\text{ msec}}\right)\left(\frac{40\text{ msec}}{d/c}\right)\left(\frac{D}{10\text{ kpc}}\right)^2 \frac{1}{2sin\theta} \tag{15.44}$$

where D is the distance to the supernova and $\delta t(10\text{ kpc})$ is the registration error for a source at 10 kpc estimated to be of $\sim$ 2 msec. From this expression Eq:15.44, a supernova at $D = 10$ kpc and $\theta = 60^\circ$ will be located with a width for the band on the sky of $\delta\theta \sim 6^\circ$ between SK and SNO and $\delta\theta \sim 24^\circ$ between SK and MACRO, considering their relative distance (SK-SNO and SK-MACRO) $d \approx 30$ msec [BKG92, HV98, HSV98].

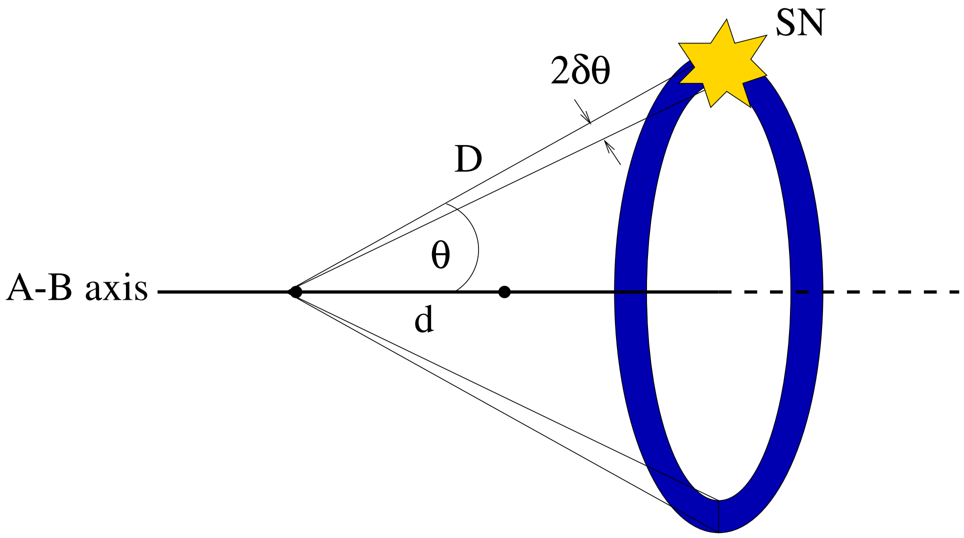

Figure 15.69: Principle to determine the direction of a supernova through the absolute timing of the neutrino signal detected in two experiments (A & B) given by the dots. Two detectors define a cone along their axis (A-B axis) with the angular opening $cos\theta$ and thickness $2 \cdot \delta(cos\theta)$, where the supernova could lie [Bea98, Hab99]. For two detectors separated by a distance d the arrival time of the neutrino signal will be delayed by Δt.

The method of the triangulation would be more efficient with a larger number of detectors. Indeed three detectors define a plane, where two non-degenerate solutions, each as "charge image" of the other, can be determined [Vag98]. To remove the ambiguity of the second charge image solution a fourth detector is needed, determining an unique point/region in the sky. Notice that the unique contribution of AMANDA located in in the southern hemisphere allows through the overlap of the allowed regions to define unambiguously a region in the sky at 90% C.L. within which the supernova could be located (see Fig.15.70).
If all detectors would be located in the northern hemisphere, triangulation for many SN directions would be problematic [Bur98b]. For this reason the AMANDA detector located at the South Pole will play a crucial role in the network. For this AMANDA's time resolution has to achieve the order of ~ 1 msec. This might be possible with the new SN electronics, which will be implemented in the season 1999/2000.
Current opinions about the viability of triangulation are still in disagreement with each other. A recent calculation is rather pessimistic concerning the possibility of triangulation with a network of different detectors [Bea98, BV99] and clearly favors neutrino-electron scattering with the best pointing precision. The triangulation suffer from the limited statistics at the leading edge which influences strongly the error δt. Thus, the corresponding error of the triangulation was estimated to be of the order $\delta(cos\theta) \backsim 0.5$.

16 Amanda Supernova Trigger Algorithm (ASTA)

16.1 The Principle and Goals

The main goal of a supernova alert algorithm for the AMANDA detector is to trigger on supernova events, and at the same time to suppress "bad" events, which could be confused with a supernova.

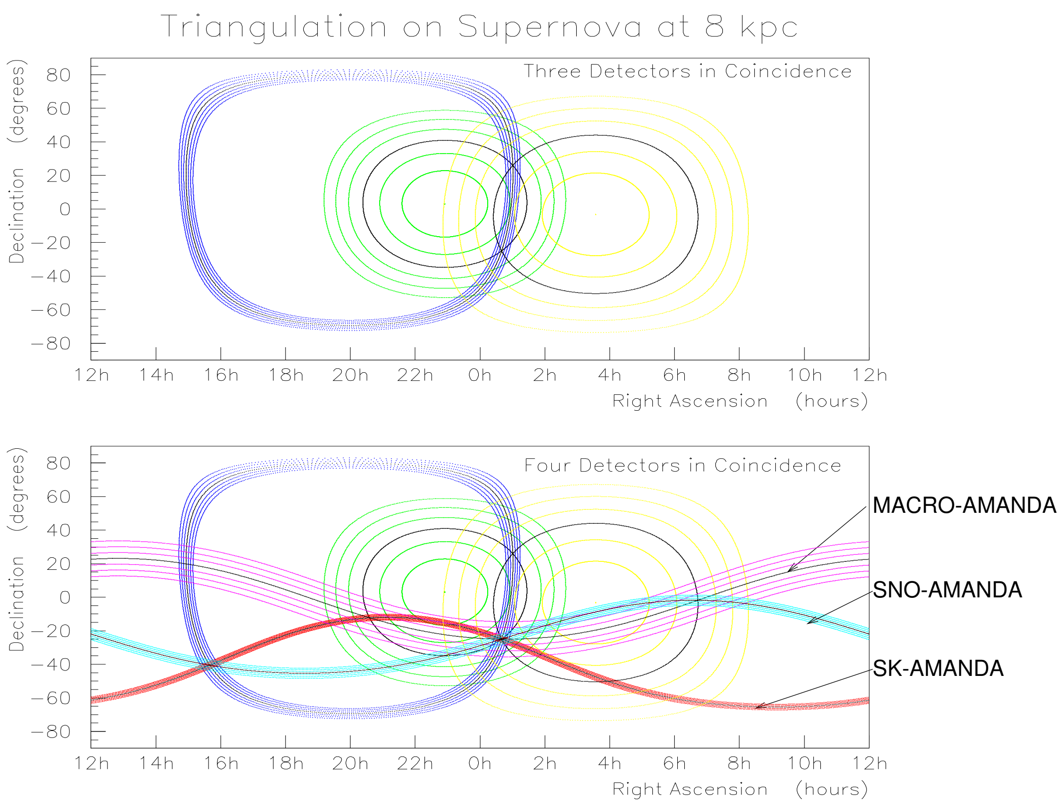

Figure 15.70: Numerical simulation of a supernova at 8 kpc (SN position 25.0°S latitude and 10.0°E longitude). The neutrino wave will pass through the detectors, and its timing signal and resolutions are used to draw "allowed regions" at 90 % C. L. (Top) Three detectors coincidence (SK, MACRO and SNO) all located in the northern hemisphere. (Bottom) four detectors coincidence (SK, MACRO, SNO, AMANDA) with AMANDA in the southern hemisphere. Figure from [HV98].

These events showing high noise rate excess can be due to unexpected activities such as calibration using laser light, or unexplained correlated noise in several channels.

Furthermore, it must be made sure that no real supernova event will be suppressed. In addition to sending a SN alarm, the algorithm can also estimate the strength of the signal and the distance at which the supernova occurred.

To test and develop the algorithm, only the 98 data were used. This decision was taken to test the stability of the given sample of PMTs judged "good" in the 97 data (see App.B). The table of good PMTs (in total 170) and their statistical behavior (counting rate average $\langle R_{back} \rangle$ and its standard deviation σ_{PMT} calculated using a stable run of $\sim$ 5 days) is the same, that was used for the off-line 97 analysis.

The results will also give an idea about the stability of a constant number of PMTs for the array which can detect a supernova. In addition to that, the possibility of achieving a so-called "on-line" PMT selection ($N_{\mathrm{PMT}}^{on-line}$ algorithm) was studied, where one updates the table of "good" PMTs, every time interval.

16.2 Algorithm Steps

The important steps of the ASTA algorithm can be summarized as follows (see also Fig.16.71):

1. The data come from a large file in which the information of $\sim$ 6 days of lifetime 98 is merged. This file simulates the future data flow coming from the SN DAQ.

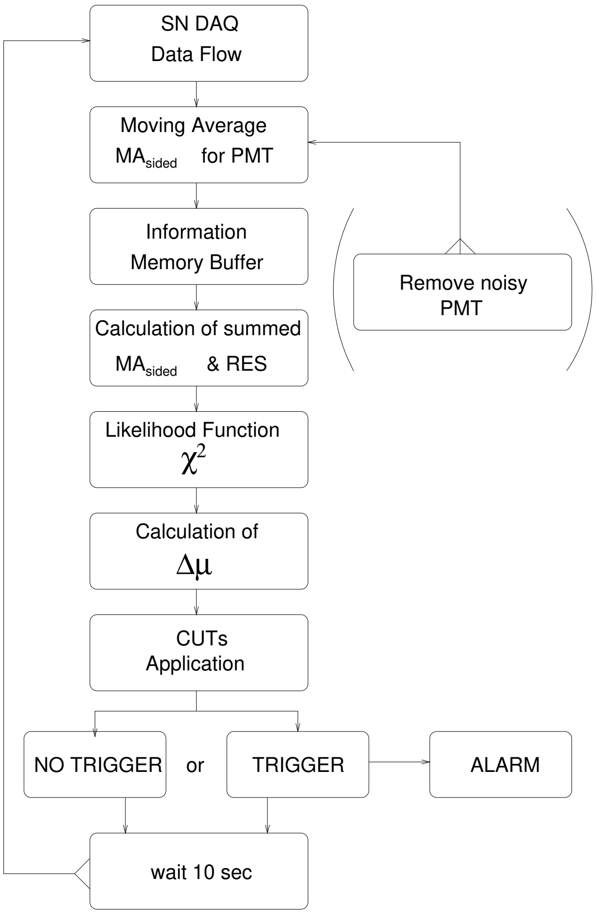

Figure 16.71: Main steps run through by the ASTA algorithm. Each event checked for by the algorithm is the 10 sec combined counting rate interval of 170 selected PMTs only. See text for details.

2. At each time interval (here 10 sec), a left-sided moving average (MA_{sided}) with a TW of 1000 sec and residual deviation of that counting rate (RES) from the moving average are calculated for each PMT.
3. This information is put into a memory buffer, where the RES of the single PMTs is stored, as well as their MA_{sided}.
4. The summed residual deviation $RES(S_{tot})$ over all selected PMTs from the $MA_{sided}(S_{tot})$ of the sum is calculated, also with a TW of 1000 sec.
5. The next step is to fit the event. The χ^2/ndf for each event is calculated. In our case the *ndf* is the number of selected PMTs.
6. From the χ^2 function, the best estimate of $\Delta\mu$ is calculated. It represents the most probable excess in the number of counts for each event.
7. At this point, the algorithm has all the needed information and the cuts can be applied in the following way:
(a) Cut on $\chi^2/ndf < 1.3$, which should conserve 99.8 % of all the events.
(b) Cut on $\Delta\mu > 5$ Hz, which will remove pure dark noise background events.
(c) Cut on the summed residual $RES > 0$ Hz, which takes away large fluctuations of MA_{sided} due to the sudden jumps in S_{tot}.
If no events pass the cuts, the algorithm will consider the next time interval. If an event should

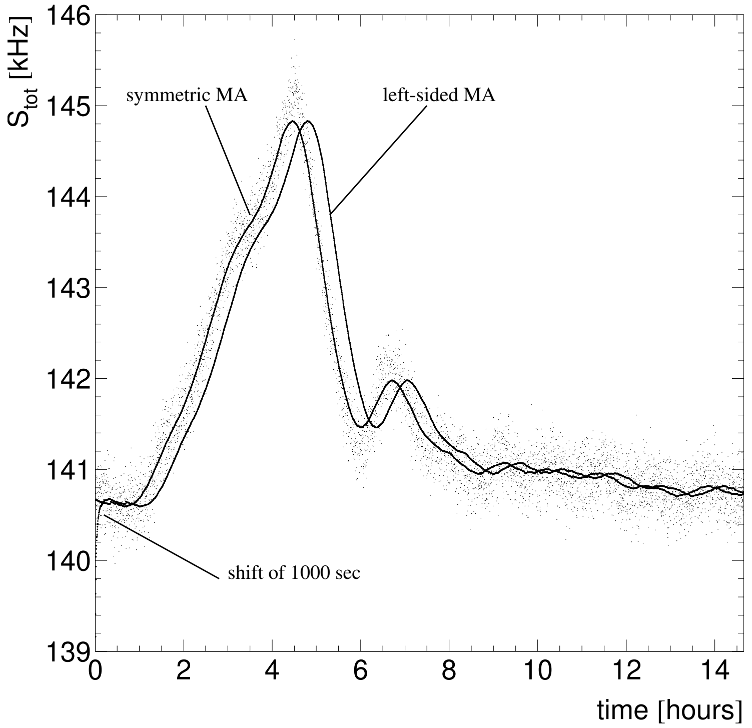

Figure 16.72: Summed counting rate S_{tot} versus time. The two moving average behaviors, both the MA_{sym} and MA_{sided} are indicated. Notice that the MA_{sided} at the beginning of the calculation (the first 1000 sec) does not follow the S_{tot} behavior. Notice also the shift between the two moving averages.

pass all three cuts, an alarm will be sent and the details of the event will be written to disk. The motivation for the cuts is given in the subsections below.
Fig.16.72 shows the main difference between the symmetric moving average MA_{sym}, used in the SN off-line analysis, and the left-sided MA_{sided}, appropriate for the ASTA algorithm. Notice that MA_{sided} is roughly shifted by 1000 sec with respect to MA_{sym} and S_{tot}.This induces a retarded response of MA_{sided} when S_{tot} suddenly jumps to high values resulting to large negative drop of the RES.

16.3 “Bad Runs” Data Sample

16.3.1 No Cuts

The first sample considered is a collection of runs of 1998 data which are known to have a very unstable behavior, covering $\sim$ 6 days of lifetime. These files were selected ad hoc, because they were rejected in advance in the off line SN analysis due to their extremely bad quality.
Their instability can be seen in Fig.16.73 where the behavior of several variables as a function of time is shown, time zero indicating the beginning of the calculation. The first plot is showing $S^{302}_{tot.}$, which represents the combined counting rate of all PMTs (302 “bad” + “good”). Its large fluctuations indicate the very bad quality of the chosen files. The second plot shows $S_{tot.}$ for the 170 selected PMTs. Here the step seen in $S^{302}_{tot.}$ is gone, indicating that this behavior was due to mainly “bad” rejected PMTs. The third plot shows RES, representing the deviation between $S_{tot.}$ and MA_{sided}. The high values of the χ^2/ndf function (fourth plot) shows the spots of the very

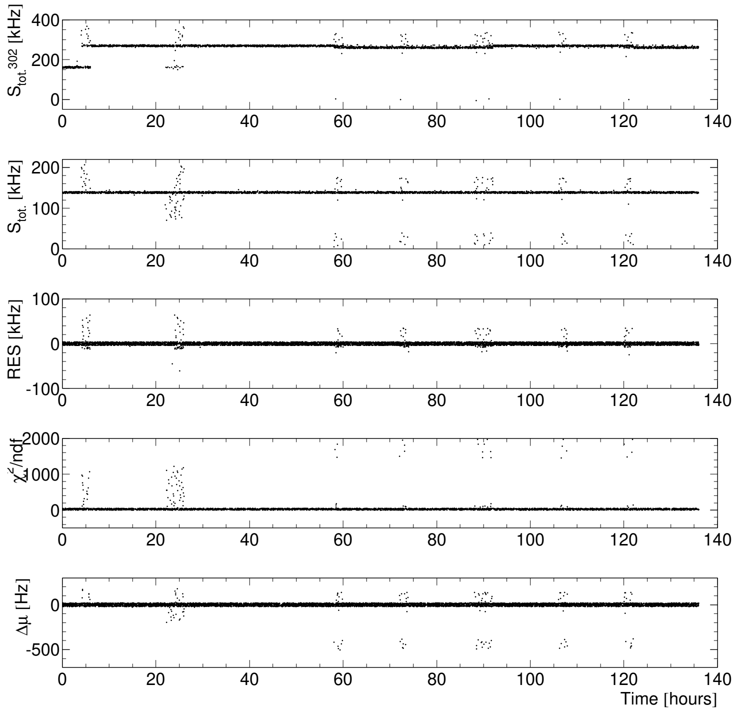

Figure 16.73: Several variables ($S_{tot.}^{302}, S_{tot.}, RES, \chi^2/ndf, \Delta\mu$) as a function of time (hours). Here are shown examples of very unstable periods for $\sim$ 6 days lifetime. The large scale of the y-axis is due to the spreading of some spots where the detector is out-of-control. Here no cuts were applied.

noisy events. The last plot shows the behavior of $\Delta\mu$, which represents the most probable value for the rate excess of good PMTs.

16.3.2 On-Line Selection of "Good" PMTs

The the plots in Fig.16.73 have been produced using the table of 170 stable PMTs of data 97. By putting constraints on the behavior of the noise rate for each PMT at each time interval, it is possible to achieve a so-called "*on-line*" PMT selection ($N_{\mathrm{PMT}}^{on-line}$). For this selection, two cuts were used. PMTs are excluded when they show:
(1) a noise rate R_{back} fluctuation larger then 3 σ_{PMT} from their moving average MA_{sided};
(2) R_{back} fluctuation larger then 5 σ_{PMT} from their mean value $\langle R_{back}\rangle$.
The time profile of $N_{\mathrm{PMT}}^{on-line}$ applying these two cuts, can be seen in Fig.16.74 (upper). The lower plot shows the $N_{\mathrm{PMT}}^{on-line}$ distribution, where three peaks can be distinguished. The highest peak at $\sim 165-170$ PMTs shows that, for most of the time, a large number of PMTs was kept. The central peak at $\sim$ 100 PMTs corresponds to the drop of $S_{tot.}^{302}$ at the beginning of the first 10 hours, and the smaller around $\sim$ 0 PMTs represents the very noisy spots where almost all PMTs were removed.
As we will see below, the $N_{\mathrm{PMT}}^{on-line}$ method triggers on fake events and cuts away real SN events. Since it is expected that a Supernova event will produce an increased number of counts. A very close Supernova would generate a larger number of counts in 10 sec. An estimated Supernova close to the Galactic center $\sim$ 8 kpc gives $\sim$ 100 counts per PMT in 10 sec, (10 Hz) while a Supernova at $\sim$ 1 kpc gives $\sim$ 6400 counts (640 Hz). Now translating this information for the expected fluctuation of each PMT, which usually has a standard deviation σ_{PMT} $\sim$ 8 Hz, the

expected Supernova at ~ 1 kpc would give a significant fluctuation of $\sim 80\ \sigma_{\rm PMT}$ for each PMT, whereas our cuts were set at $R_{back} - MA_{sided} < 3\ \sigma_{\rm PMT}$ and $R_{back} - \langle R_{back} \rangle < 5\ \sigma_{\rm PMT}$ cutting already SN signal at distance ≤ 4.2 kpc (a SN at 8 kpc would give a fluctuation of $\sim 1.4\ \sigma_{\rm PMT}$). From here on, the $N_{\rm PMT}^{on-line}$ algorithm will not be investigated further, only the ASTA algorithm with a constant number of PMTs will be considered.

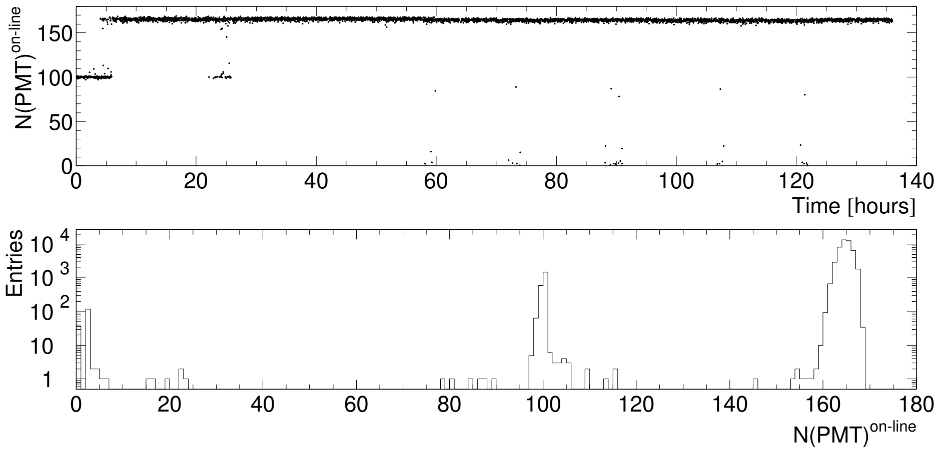

Figure 16.74: (Upper) Number of on-line selected PMTs $N_{\rm PMT}^{on-line}$ versus time. The go-down of $N_{\rm PMT}^{on-line}$ in distinct spots is clearly correlated to the high values of χ^2/ndf. The drop of $N_{\rm PMT}^{on-line} \sim 100$ to that of $S_{tot.}^{302}$ at the beginning of the file. (Lower) Distribution of $N_{\rm PMT}^{on-line}$ (in log-scale). The largest peak around 165 PMTs indicates that for most of the time, a large number of PMTs was maintained.

16.4 Effects of the Cuts Application

The results for ASTA after the cut on $\chi^2/ndf < 1.3$ can be seen in Fig.16.75. Note that after this cut, 99.8 % of all pure dark noise as well as potential SN-events should be conserved. The variable $S_{tot.}^{302}$ still has a drop at the beginning of the plot. Nevertheless, the result for $S_{tot.}$ is better now, since its larger deviations of noise rate are cut away.

In the third plot, the negative values of RES are interesting, since they can induce unexpected fake events, if one removes PMTs in the algorithm. A stable behavior of the $\Delta\mu$ variable after the cut on $\chi^2/ndf < 1.3$ can be seen in the last plot. The variables RES and $\Delta\mu$ represent the deviation of the summed noise rate from the MA and of course they are correlated, but $\Delta\mu$ is in addition a weighted mean of the noise deviation of all individual PMTs, which could result positive with respect to negative values of RES. The cut on the fitted $\Delta\mu$ ($\Delta\mu > 5$ Hz) intends to remove pure dark noise events (Fig.16.76). Here, one can see the hardness of this cut, since out of ~ 50000 events only 5 survive. The last cut on $RES > 0$ Hz rejects these five events.

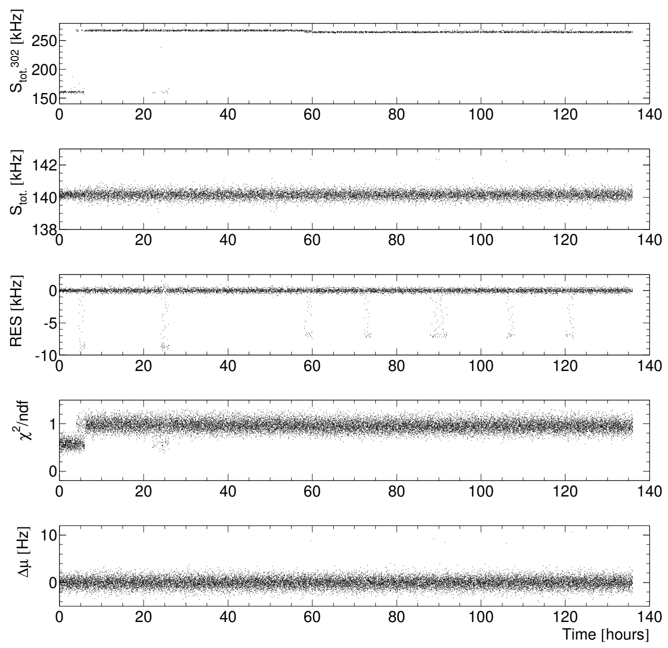

Figure 16.75: First cut: $\chi^2/ndf < 1.3$. Same variables versus time as in Fig.16.73 after cut. $S^{302}_{tot.}$ is still presenting spread spots due to the sample of "bad" PMTs. The other variables show a quite stable behavior except some negative spots of RES values.

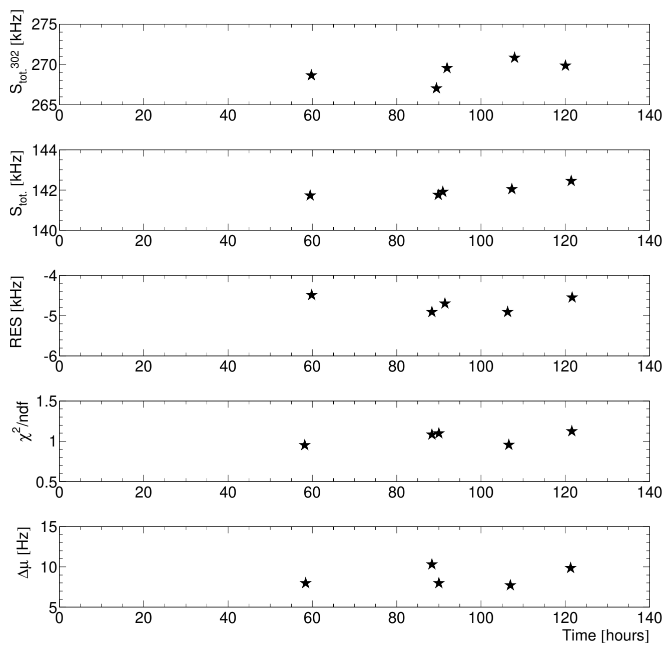

Figure 16.76: Second cut: $\Delta\mu > 5$. Same variable as in the previous picture. The dark noise background is completely removed, only still 5 events remain after this cut. Note the negative values of RES which allow us to remove definitively all remaining fakes events.

16.5 Results

Final results can be seen in Fig.16.77 as the trigger response as a function of time both for ASTA and for the $N_{\rm PMT}^{on-line}$ algorithm. The value $Trigger = 0$ represents events which do not pass one of the three cuts discussed in Sec.16.4, whereas $Trigger = 1$ indicates events which pass all three cuts. The first plot shows only 1 trigger recorded by ASTA after the following cuts: (A) $\chi^2/ndf < 1.5$, (B) $\Delta\mu > 5$ Hz, (C) $RES > 0$ Hz. The cut on $\chi^2/ndf < 1.5$ is the same applied in the SN off-line analysis. No triggers survive, in the second plot, after the same cuts, with the only difference that here $\chi^2/ndf < 1.3$. The lower two plots show the results for the version of $N_{\rm PMT}^{on-line}$ algorithm with the constraint that more than 100 PMTs be kept. There are many triggers during only 6 days of lifetime. This suggests that the PMTs removed on-line are essential to diagnostic bad events and to reject them. Such PMTs are normally stable, they become unstable only due to disturbances in parts of the detector. This demonstrates the higher reliability and robustness of ASTA compared to a possible version of a $N_{\rm PMT}^{on-line}$ algorithm.

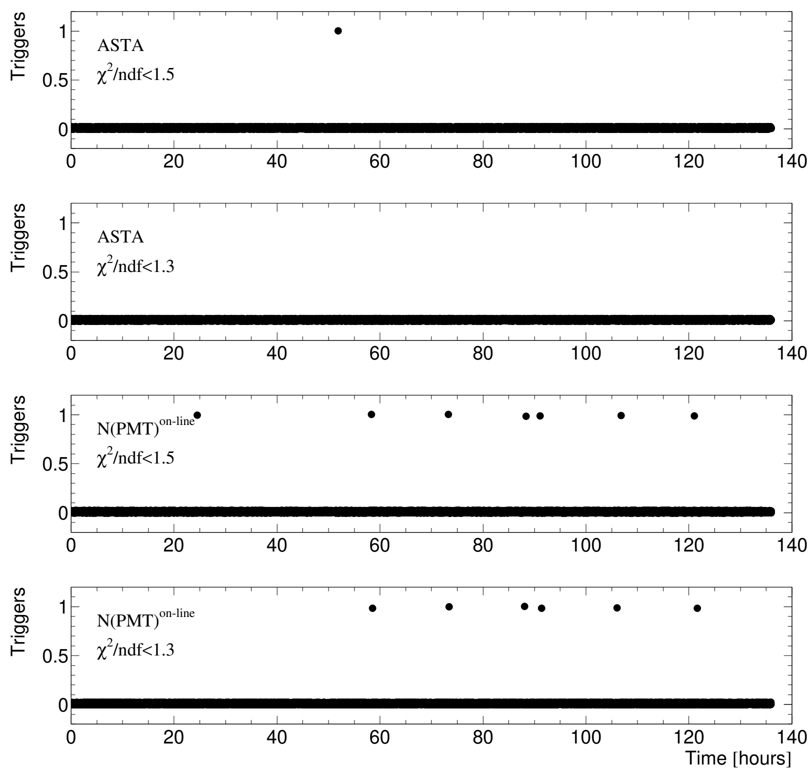

Figure 16.77: (Upper) Triggers versus time for ASTA algorithm with the constant number of 170 PMTs, (lower) the version of the $N_{\rm PMT}^{on-line}$ algorithm. ASTA gives a false alarm with the cut on $\chi^2/ndf < 1.5$, while no trigger at all are recorded with the cut on $\chi^2/ndf < 1.3$. A large number of false triggers are detected by the $N_{\rm PMT}^{on-line}$ algorithm both for $\chi^2/ndf < 1.5$ and $\chi^2/ndf < 1.3$.

Fig.16.78 shows the integrated number of triggers $\sum Triggers$ versus χ^2/ndf. The plot yields the actual value of the cut on $\chi^2/ndf < 1.3$ and estimates the frequency of false alarms as a function of any cut on χ^2/ndf. For example, a cut at $\chi^2/ndf < 2.$ would already give $\sum Triggers = 3$. Note that, even during periods where a few PMTs are removed (i.e. remaining $N_{\rm PMT}^{on-line} = 165$), ASTA is still working with $\chi^2 < 1.3$ and $\Delta\mu < 5$ Hz.

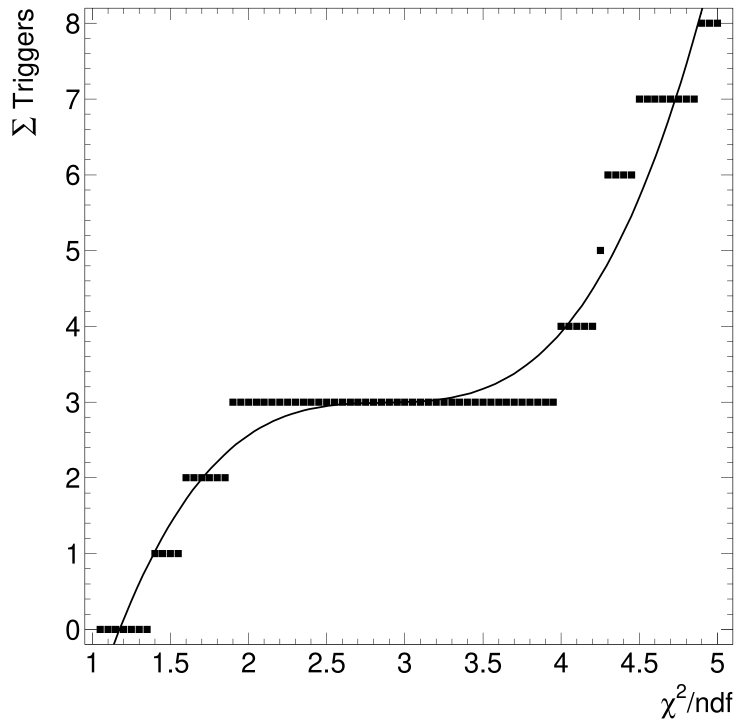

Figure 16.78: Number of triggers as a function of χ^2/ndf for ASTA (fit with a polynomial of third grade). Note that $Trigger = 0$ is expected applying a cut on χ^2 less than 1.3.

Table 16.7 shows some events, where the $N_{\mathrm{PMT}}^{on-line}$ algorithm detected a trigger. In total 6 $Triggers$ were recorded and 14 $Triggers$ if one would remove the constraint $N_{\mathrm{PMT}}^{on-line} > 100$. The reason for such false alarms was only due to the removal of some "unstable" PMTs with this algorithm during some periods. For these events, ASTA recorded large negative RES, while RES from the $N_{\mathrm{PMT}}^{on-line}$ algorithm is positive and gives a trigger. A possible explanation is that some activity producing light inside the detector was going on at that time. This would justify why some PMTs were turned off and why the level of noise in the remaining PMTs was high. It also explains why the RES for ASTA is negative.

$N_{\mathrm{PMT}}^{on-line}$	$\frac{\chi^2}{ndf}$ on-line	$\frac{\chi^2}{ndf}$ ASTA	$\Delta\mu$ (Hz) on-line	$\Delta\mu$ (Hz) ASTA	RES (Hz) on-line	RES (Hz) ASTA
84	1.25	4.00	17.04	28.28	2364.53	507.05
159	0.82	1.07	7.95	8.79	2090.05	-4689.13
161	0.84	1.01	8.32	9.07	2015.96	-4836.72
19	0.65	16.39	16.80	50.30	527.634	6509.53
161	1.03	1.05	7.90	8.18	2076.97	-4910.57

Table 16.7: Five of the 14 events triggered by the $N_{\mathrm{PMT}}^{on-line}$ algorithm. For a better comparison values of both ASTA and the $N_{\mathrm{PMT}}^{on-line}$ algorithm are listed. ASTA does not give any triggers due to conserving of some unstable PMTs which cause either high values of χ^2/ndf or large negative values of RES.

16.6 Monte Carlo Test

The results of the ASTA algorithm applied on a generated MC file (~15 hours) with simulated SNs every 1000 sec, are shown in Fig.16.79. The simulation was computed with the same algorithm as discussed in Sec.9. The first plot indicates clear triggers for such supernovae. All supernova events, which are distributed normally above the background distribution, pass all the cuts giving the alarm. The lower plots depicts the two background distributions ($\Delta\mu$ and RES) and the expected signal.

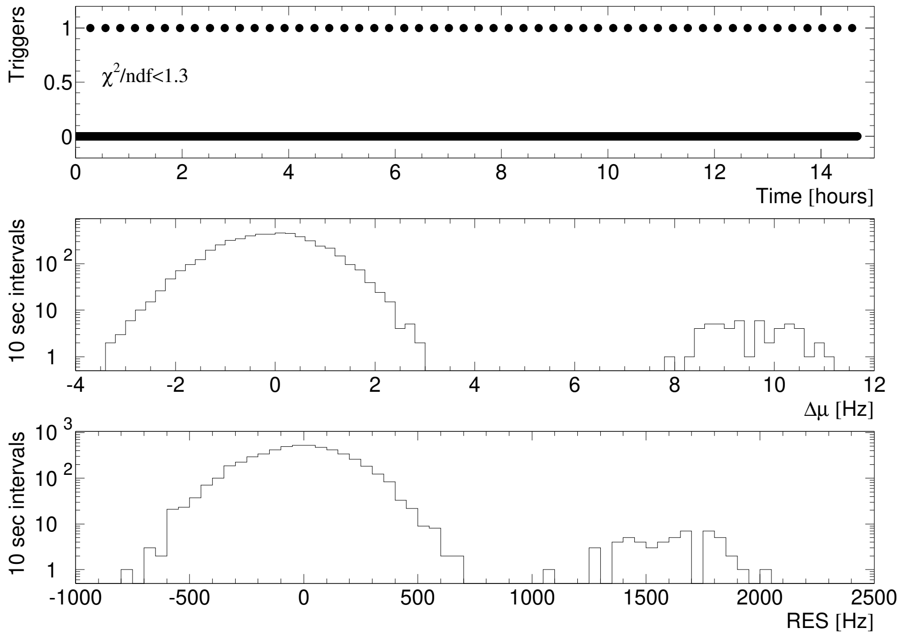

Figure 16.79: MC results of ASTA for simulated SN events in file of $\sim$ 15 hours. (Upper) $Triggers$ versus time, now the algorithm triggers all SN events. (Lower) Distribution of $\Delta\mu$ and RES where it is easy to distinguish the background from the SN signal.

16.7 Comparison with a Sample of Stable Runs

The behavior of the variables (S^{302}_{tot}, S_{tot}, RES, χ^2/ndf, $\Delta\mu$) for stable files is shown in Fig.16.80 (to be compared with Fig.16.73). This data is very stable, even without any cuts for a full time of $\sim$ 5 days. The graphs in Fig.16.81 show the results applying the cut $\chi^2/ndf < 1.3$. The few noisy events which were present before this cut, now disappear leaving a nice Gaussian behavior of the variables (S^{302}_{tot}, S_{tot}, $RES \mathrm{and} \Delta\mu$). Notice that now the RES variable is stable, showing no large negative values which would indicate instabilities in the combined counting rate S_{tot}.

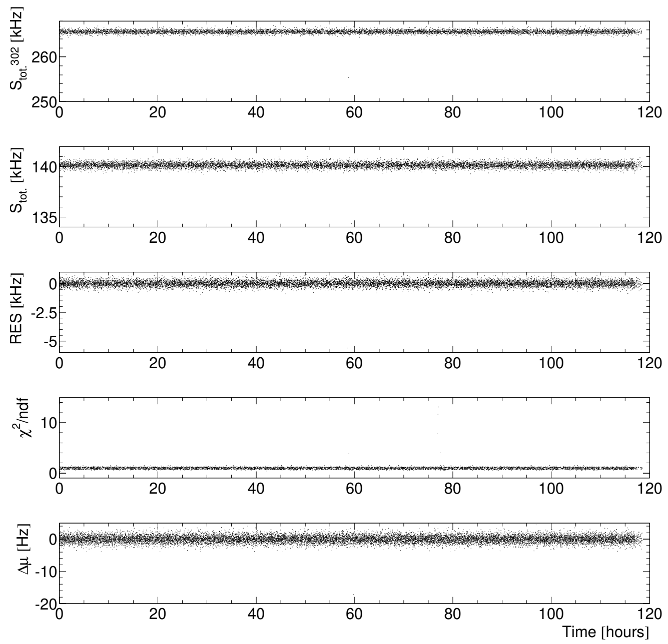

Figure 16.80: The variables $(S_{tot}^{302}, S_{tot.}, RES, \chi^2/ndf, \Delta\mu)$ plotted versus time for an example of $\sim$ 5 days lifetime of selected stable files. No cuts were applied.

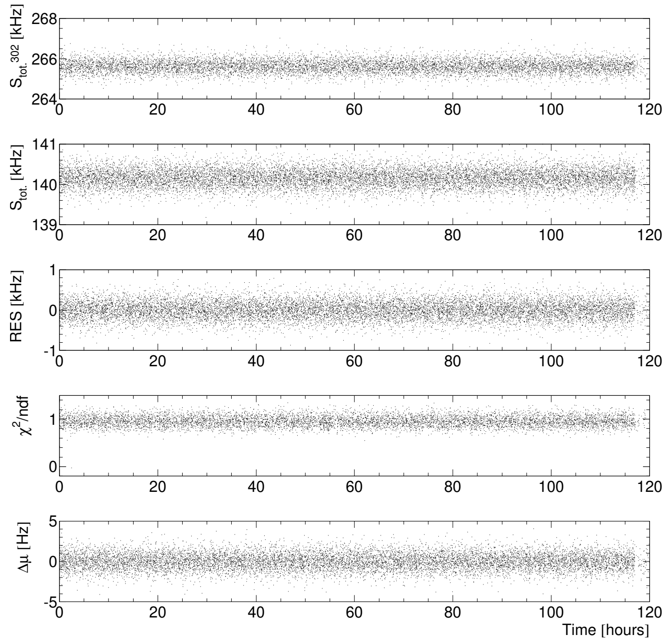

Figure 16.81: First cut: $\chi^2/ndf < 1.3$. Only few noisy spots were removed leaving a stable behavior of all variables.

16.8 Discussion and Conclusion

From this analysis it can be concluded that the ASTA algorithm works as required. Even during tests over very bad periods, the algorithm is reliable, giving no triggers. Testing the algorithm with generated Monte Carlo files, containing simulated supernova events, the algorithm responds in a satisfying way giving the desired triggers.
It must be emphasized that the version of the $N_{\mathrm{PMT}}^{on-line}$ algorithm does not work well, giving a high frequency of triggers, which are false alarms.
This suggest that the algorithm with a constant number of stable PMTs, which are well understood, can guarantee, at the current status, a supernova event alarm up to 8.8 kpc at 90% detection efficiency.
Assuming $\Delta\mu = 10$ Hz $\cdot\, (\frac{8 \text{ kpc}}{d})^2$, one can estimate the distance of a SN occurrence and roughly give its uncertainty. The dominant error in $\Delta\mu$ comes from the dark noise background, $\sigma_{\Delta\mu} = \sigma_{\mathrm{PMT}}/\sqrt{N_{\mathrm{PMT}}}$. Thus, the corresponding error for the distance would be $\sigma_d/d = \ 0.5 \ \cdot \sigma_{\Delta\mu}/\Delta\mu$, $\sigma_d = (8.0 \pm 0.22)$ kpc or (8.0 ± 0.55) kpc considering $N_{\mathrm{PMT}} = 170$ and assuming $\sigma_{\mathrm{PMT}} = 7$ or 18 Hz respectively. Of course the error due to the lack of precise knowledge of the supernova strength is much larger.
If one defines the *dead time* of a trigger algorithm as the percentage of time when it would not be able to signal a real SN, then it can be calculated in the following way. Applying all cuts, except those that remove pure dark noise events and SN events, i.e. applying $\chi^2/ndf < 1.3$ and $RES > -3\sigma_{RES} \approx 210$ Hz, the number of events N_{OK} is smaller than the total amount of events previous to cuts N_{TOT}. So the dead time percentage is $\eta = (N_{TOT} - N_{OK})/N_{TOT}$, where for the worst periods $\eta = 2.7\%$ and for normal/good periods $\eta = 0.2\%$. This result shows also that during the worst periods the detector is "out-of-control" only for a very short fraction time, which actually does not compromise the whole file. Using a *sliding* window of 10 sec instead of consecutive windows, the signal could be seen with a much higher efficiency. This could not be studied here, but leaves the prospect open to improve the performance of the trigger significantly.
A future implementation of ASTA in the SN DAQ for an on-line SN monitoring for AMANDA, would make a future AMANDA contribution in the SNEWS network possible The information that AMANDA would send if a $Trigger$ signal occurred can be summarized as follows: (1) Confirmation of a gravitational collapse up to 8.8 kpc; (2) Time of the occurred event with a current resolution of 0.5 sec; (3) Estimate of the strength of the signal $\Delta\mu$.

17 Conclusion

Results from this analysis demonstrate the capabilities of AMANDA to search for neutrino bursts from gravitational stellar collapse. A Main Analysis program has been developed, an essential tool for the supernova off-line analysis. A method to select stable PMTs and good quality runs has been developed yielding $\sim 77\%$ of all runs, and a sub-sample of 170 out of 302 PMTs with a difference of 11 PMTs only between the selected sample in 1997 and 98. Trends and discontinuities in the combined counting rate of all PMs were efficiently removed by moving average subtraction. In order to separate potential SN neutrino burst candidates from non-Gaussian excesses a Maximum-Likelihood method was applied which conserves 99.9% of all events.
No evidence for burst candidates has been found for a total live-time of 220 days. A fake event rate of one per year is expected to occur when setting the threshold to 90% detection efficiency for a SN at a distance of 8.8 kpc (AMANDA-B10 and at a distance (AMANDA-B4), respectively.
Monte Carlo calculations have been performed to make the comparison between the data results and the expectation from the supernova signal. The signal prediction taking into account 10 sec counting rate intervals leads to a reduction of the sensitivity down to 57% compared to the ideal case, where the signal is made to fall exactly in the 10 sec window. Based on the results of Bahcall and Piran [BP83] for the fraction of stars in our Galaxy, the performance of AMANDA can be estimated for a search for stellar collapses *within* a given distance from our Sun. AMANDA is surveying 50% of the Milky Way for a potential gravitational stellar collapse with a S/N$\geq$ 1, assuming a signal "S" of one collapse per century. Based on the 18 months of detector operation a calculation of an upper limit at 90% c.l. on the gravitational stellar collapse rate in our Galaxy yields 8.59 $events{\cdot}year^{-1}$. Scaling the 220 days of live-time of AMANDA to that of the LVD detector, this limit corresponds to 0.93 $events{\cdot}year^{-1}$. Assuming a ten year live-time and taking into account the coverage of 50% of the Galaxy with an efficiency of 90% , the probability that AMANDA would observe a Galactic supernova is 9% , if the frequency of a core collapse supernova is one per 47 years [TLS94].
A prediction for a detector upgrade to 250 PMTs of the same quality as those of AMANDA-B4 yields an increase of the visibility range up to 14 kpc (79% of the Galaxy) and an upgrade to 800 PMTs would cover the whole Galaxy. A real-time supernova detection algorithm, ASTA (AMANDA Supernova Trigger Algorithm) has been developed, demonstrating a good rejection power of false alarms and giving no triggers for a total of 11 days of data. This proves the stability of the selected subset of 170 PMTs. Monitoring would yield an expected alarm rate smaller than 1-2 per year. The performance of AMANDA with respect to SN detection could be increased by the following methods.
A future analysis using a sliding window of 10 sec would increase the sensitivity to detect potential supernova candidates. Furthermore the methods of analysis can be refined by trying to select a larger number of low noise PMTs of strings 1-4. Since the noise is the most dominant factor for the detector performances, it must be kept low. This aim can be achieved by choosing glass for the OMs with low ^{40}K content. The live-time of the detector operation could be increased with a more efficient run rejection, i.e. cutting only the "bad" periods within a given file. Non-Poissonian behavior of the counting rate has to be solved, since the visibility range depends on the width of the background distribution.
For this analysis the conservative information of the *faint* supernova 1987A was used, therefore one can conclude that for an average signal the performance and the response of the detector are probably better.

Acknowledgments

I would like to thank a lot of people.

First I have to thank and express my gratitude to Dr. Adam Bouchta with whom I have worked in close collaboration on this topic during the past year. Thanks also for long and fruitful discussions and for correcting this work.
I would like to thank Dr. Ralf Wischnewski for collaboration, in particular for his help with data handling and understanding of the data, Dr. Thorsten Thon for discussions about the hardware and Dr. Christian Spiering for supervision, for long discussions, proof reading and corrections.
I would also like to thank the whole AMANDA Zeuthen group, especially Dr. Paolo Desiati, Peter Nießen and Ole Streicher for their help and discussions.

I would like to extend my gratitude to Prof. Thomas Hebbeker at the Humboldt-Universität zu Berlin for discussions about this work and for taking the responsibility for my thesis.

I would like to thank my girl friend Birgitta Wehner for being always near me both in good and difficult moments.

Many thanks go to my parents Franco Silvestri and Annarosa Di Bernardo for their help and unfailing support during my studies.

References

[AAV87] E. N. Alekseev, L. N. Alexeyeva, and I. V. Krivosheina V. I. Volchenko, 1987.

[AF87] M. Aglietta et al. and Frejus-coll., 1987.

[Ahl92] S. Ahlen et al. *Search for Neutrino Bursts from Collapsing Stars with the MACRO Detector*. *Astropart. Phys.*, **1**:11, 1992.

[Amb98] M. Ambrosio et al. *Real Time Supernova Neutrino Burst Detection with MACRO*. *Astropart. Phys.*, **8**:123, 1998.

[And99] E. Andres et al. *The* AMANDA *Neutrino Telescope: Principle of Operation and First Results*. *astro-ph/9906203, DESY 99-073*, July 1999. ISSN 0418-9833, accepted in *Astropart. Phys.* 2 (2000).

[ANT97] The ANTARES collaboration. *ANTARES, towards a large scale high energy cosmic neutrino undersea detector*. *astro-ph/9707136*, 1997.

[Arn96] D. Arnett. *Supernovae and Nucleosynthesis*. Princeton University Press, New Jersey, 1996.

[Arn99] D. Arnett. *Explosive Nucleosynthesis: Prospects*. *astro-ph/9908171*, 1999.

[Ask95] P. Askebjer et al. *Optical Properties of the South Pole Ice at Depth between 0.8 and 1 kilometer*. *Science*, **267**:1147, 1995.

[Bah89] J. N. Bahcall. *Neutrino Astrophysics*. Cambridge University Press, 1989.

[BD96] P. J. Brockwell and R. A. Davis. *Introduction to Time Series and Forecasting*. Springer Verlag, New York Berlin Heidelberg, 1996.

[Bea98] J. Beacom. *Can we locate a SN with neutrinos? i. Triangulation, ii. Asymmetric reactions, in First International Workshop on the Supernova Early Alert Network*. Boston University, Bound photocopied transparencies, 1998.

[BHF95] A. Burrows, J. Hayes, and B. A. Fryxell. *On the Nature of Core-Collapse Supernova Explosions*. *Ap. J.*, **450**:830, 1995.

[Bio87] R. M. Bionta et al. *Observation of a Neutrino Burst in Coincidence with Supernove 1987A in the Large Magellanic Cloud*. *Phys. Rev. Lett.*, **58**(14):1494, 1987.

[Bir97] A. Biron et al. *Upgrade of* AMANDA B *towards* AMANDA-II, June 1997.

[BKG92] A. Burrows, D. Klein, and R. Gandhi. *The Future of Supernova Neutrino Detection*. *Phy. Rev. D*, **45**(10):3361, 1992.

[Bou] A. Bouchta. Private communication.

[Bou98] A. Bouchta. *Muon Analysis with the* AMANDA-B *Four-Strings Detector*. *Ph.D thesis, Stockholm University*, 1998. ISBN 91-7153-754-6.

[Bou99] A. Bouchta et al. *Seasonal Variation of the Muon Flux seen by* AMANDA. *Proceeding of the 26th International Cosmic Ray Conference (ICRC 99), Salt Lake City, UT*, August 1999. HE.3.2.11.

[BP83] J. N. Bahcall and T. Piran. *Stellar Collapses in the Galaxy*. *Ap.J.*, **267**:L77, 1983.

[Bru87] S. W. Bruenn. *Neutrinos from SN 1987A and Current Models of Stellar-Core Collapse*. *Phys. Rev. Lett.*, **59**(8):938, 1987.

[BS80] J. N. Bahcall and R. M. Soneira. *The Universe at Faint Magnitudes. I. Models for the Galaxy and the Predicted Star Counts*. *Ap.J.*, **44**:73, 1980.

[Bun95] J. Bunn et al. *HBOOK - Statistical Analysis and Histogramming*, cern program library entry **y250** edition, May 1995.

[Bur88] A. Burrows. *Supernova Neutrinos*. *Ap. J.*, **334**:891, 1988.

[Bur90] A. Burrows. *Neutrinos from Supernovae, in Supernovae*. New York: Springer Verlag, 1990.

[Bur98a] A. Burrows. *The Current Status of Core Collapse Supernova Theory, in First International Workshop on the Supernova Early Alert Network*. Boston University, Bound photocopied transparencies, 1998.

[Bur98b] A. Burrows. *Summary of discussion session I: the neutrino signal and triangulation*, 1998. `http://hep.bu.edu/~schol/workshop/workshop_summary.html`.

[BV99] J. F. Beacom and P. Vogel. *Can a supernova be detected by its neutrinos?* *Phys. Rev. D*, **60**(3):33007, 1999.

[BW85] H. A. Bethe and J. R. Wilson. *Revival of a Stalled Supernova Shock by Neutrino Heating*. *Ap. J.*, **295**:14, 1985.

[BZ34a] W. Baade and F. Zwicky. *Phys. Rev.*, **45**:138, 1934.

[BZ34b] W. Baade and F. Zwicky. *Proc. Nat. Acad. Sci.*, **20**:259, 1934.

[CB90] J. Cooperstein and E. A. Baron. *Supernovae: The Direct Mechanism and the Equation of State, in Supernovae*. New York: Springer Verlag, 1990.

[Cha31] S. Chandrasekhar. *The Maximum Mass of Ideal White Dwarfs*. *Ap. J.*, **74**(81c), 1931.

[Cha82] C. Chatfield. *Analyse von Zeitreihen*. BSG B. G. Teubner Verlagsgesellschaft, Leipzig, 1982.

[CO96] B. W. Carroll and D. A. Ostlie. *An Introduction to Modern Astrophysics*. Addison-Wesley Publishing Company, Inc., 1996.

[Cou95] O. Couet et al. *PAW - Physics Analysis Workstation. An Introductory Tutorial*, cern program library entry **q121** edition, February 1995.

[Fuk98] Y. Fukuda. *Observation of Supernova Neutrino at Super-Kamiokande, in First International Workshop on the Supernova Early Alert Network*. Boston University, Bound photocopied transparencies, 1998.

[Gro99] The Hipparcos Web Group. *Hipparcos Statistics*, 1999 . `http://astro.estec.esa.nl/Hipparcos/vis_ stat.html`.

[Gru93] C. Grupen. *Teilchendetektoren*. Wissenschaftsverlag Mannheim, Leipzig, Wien, Zurich, 1993.

[Hab99] A. Habig. *SNEWS: Supernova Early Warning System Poster shown at the 1999 Maryland October Astrophysics Conference Cosmic Explosions! conference*, 1999 . `http://hep.bu.edu/~snnet/`.

[Hax87] W. C. Haxton. *Nuclear Response of Water Cherenkov Detectors to Supernova and Solar Neutrinos*. *Phy. Rev. D*, **36**(8):2283, 1987.

[Hei98] J. Heise. *The Status of Supernova Readiness with SNO, in First International Workshop on the Supernova Early Alert Network*. Boston University, Bound photocopied transparencies, 1998.

[Hir87] K. S. Hirata et al. *Observation of a Neutrino Burst from the Supernova SN 1987A*. *Phys. Rev. Lett.*, **58**(14):1490, 1987.

[HJZ94] F. Halzen, J. E. Jacobsen, and E. Zas. *Possibility that High Energy Neutrino Telescopes could detect Supernovae*. *Phys. Rev. D*, **49**(4):1758, 1994.

[HJZ96] F. Halzen, J. E. Jacobsen, and E. Zas. *Ultra-Transparent Antartic Ice as a Supernova Detector*. *Phys. Rev. D*, **53**:7359, 1996.

[HM84] F. Halzen and A. D. Martin. *Quarks and Leptons : an Introduction Course in Modern Particle Physics*. John Wiley and Sons, 1984.

[HNW84] W. Hillebrandt, K. Nomoto, and R. G. Wolff. *Supernova Explosion of Massive Stars. The Mass Range 8 to 10 $M_\odot$*. *Ap. J.*, **133**:175, 1984.

[HSTW94] H. Heukenkamp, C. Spiering, T. Thon, and R. Wischnewski. *A Supernova/Monopole Trigger for* AMANDA-A, 1994.

[HSV98] A. Habig, K. Scholberg, and M. Vagins. *An Early Supernova Detection System. A more detailed writeup about the poster shown at the Neutrino '98 conference in Takayama* , 1998. `http://hep.bu.edu/~snnet/`.

[Hun99] S. Hundertmark. *Simulation und Analyse von Myonereignissen im* AMANDA-B4-*Neutrinoteleskop*. *Ph.D thesis, Humboldt-Universitaet zu Berlin*, 1999.

[HV98] A. Habig and K. Scholberg M. Vagins. *The International Early Supernova Alert System. Poster shown at the Neutrino '98 conference in Takayama* , 1998. `http://hep.bu.edu/~snnet/`.

[HW90] R. P. Harkness and J. C. Wheeler. *Classification of Supernovae, in Supernovae*. New York: Springer Verlag, 1990.

[Jac96] J. E. Jacobsen. *Simulating the Detection of Muon and Neutrinos in Deep Antartic Ice. Ph.D thesis, Univ. of Wisconsin-Madison*, 1996.

[JML85] A. Yahil J. M. Lattimer, A. Burrows. *Type II Supernova Energetics*. *Ap. J.*, **288**:644, 1985.

[Ken84] R. C. Kennicutt. *Constraints on the Mass of Supernova Progenitor*. *Ap. J.*, **277**:361, 1984.

[Kuz99] L. A. Kuzmichev et al. *The Lake Baikal Neutrino Telescope NT-200: First year of operation*. *Proceeding of the 26th International Cosmic Ray Conference (ICRC 99), Salt Lake City, UT*, August 1999. HE.4.2.04.

[KZ97] H. V. Klapdor-Kleingrothaus and K. Zuber. *Teilchenastrophysik*. B. G. Teubner, Stuttgart, 1997.

[Lan99] K. R. Lang. *Astrophysical Formulae*. Springer Verlag Berlin Heidelberg New York, 1999.

[Leo94] W. R. Leo. *Techniques for Nuclear and Particle Physics Experiments*. Springer-Verlag Berlin Heidelberg New York, 1994.

[Lon94] M. S. Longair. *High energy astrophysics, volume 2 Stars, the Galaxy and the interstellar medium*. Cambridge University Press, 1994.

[Low96] D. M. Lower. *Attenuation studies using* AMANDA *calibration sources*. *Amanda internal reporter*, 1996.

[LVD99] The LVD Collaboration. *Search for Neutrino Bursts from SN Collapse with the Large Volume Detector*. *Proceeding of the 26th International Cosmic Ray Conference (ICRC 99), Salt Lake City, UT*, August 1999. HE.4.2.08.

[Man97] A. K. Mann. *Shadow of a Star, The neutrino story of Supernova 1987A*. Freeman and Company, New York, 1997.

[May90] R. W. Mayle. *Neutrino Heating Supernovae, in Supernovae*. New York: Springer Verlag, 1990.

[MB81] D. Michalas and J. Binney. *Galactic astronomy: structure and kinematics*. W. H. Freeman and Co., New York, 1981.

[MB90] E. S. Myra and A. Burrows. *Neutrinos from Type II Supernovae: The First 100 Milliseconds*. *Ap. J.*, **364**:222, 1990.

[Mez98] A. Mezzacappa. *Status of Core Collapse Supernova Models and Implications for Neutrino Signature Predictions, in First International Workshop on the Supernova Early Alert Network*. Boston University, Bound photocopied transparencies, 1998.

[MW87] R. Mayle and J. R. Wilson. *Neutrinos from Gravitational Collapse*. *Ap. J.*, **318**:288, 1987.

[NES95] NESTOR. *proposal*, 1995. `http://www.uoa.gr/ nestor/`.

[OYI+94] Y. Oyama, M. Yamada, T. Ishida, T. Yamaguchi, and H. Yokoyama. *Supernova Real-Time Monitor System in Kamiokande*. *Nucl. Instr. Meth.*, **340**:612, 1994.

[Pry88] C. Pryor et al. *Detecting Thermal Neutrinos from Supernovae with DUMAND*. *Ap.J.*, **329**:335, 1988.

[RW97] A. Richards and K. Woschnagg. *South Pole deep ice properties at $\lambda = 337$ nm*. *AMANDA internal report*, 1997.

[SC42] M. Schoenberg and S. Chandrasekhar. *On the Evolution of the Main-Sequence Stars*. *Ap. J.*, **96**(2):161, 1942.

[Sch97] R. Schwarz. *Pole Logbook for SNMP and GRB runs 1997*, 1997.

[Sch98] K. Scholberg. *Summary of discussion session II: the inter-experiment coincidence First International Workshop on the Supernova Early Alert Network*, 1998. http://hep.bu.edu/~schol/workshop/workshop_ summary.html.

[Sch99] K. Scholberg. *SNEWS: The SuperNova Early Warning System*. *Conference proceedings paper of the 3rd Amaldi Conference on Gravitational Waves*, astro-ph/9911359, 1999.

[Spi] C. Spiering. Private communication.

[Spi99] C. Spiering. *Gain variations in* AMANDA *strings 11-13*, November 1999.

[Ste82] V. J. Stenger et al. *Status of DUMAND*. *Proceeding of the 1982 DUMAND Signal Processing Workshop*, February 1982.

[Suz93] Y. Suzuki. *Kamiokande Results on Solar Neutrinos and a Supernova Search*, volume ICRR-Report-294-93-6. ICRR, Univ. of Tokyo, Tanashi, Tokyo, 1993.

[Suz94] A. Suzuki. *Supernova Neutrinos, in Physics and Astrophysics of Neutrinos*. Springer Verlag, Tokyo Berlin Heidelberg New York, 1994.

[Tho] T. Thon. Private communication.

[Tho96] T. Thon. *The* AMANDA *Supernova/Monopole Trigger Electronics. User's Guide and Reference Upgraded Version 1995*, November 1996.

[Til97] S. Tilav et al. *First Look at* AMANDA-B *data*. *Proceeding of the 25th International Cosmic Ray Conference (ICRC 97), Durban South-Africa*, July,August 1997. HE.4.1.2.

[TLS94] G. A. Tammann, W. Loeffler, and A. Schroeder. *The Galactic Supernova Rate*. *Ap. J. Supp.*, **92**:487, 1994.

[Vag98] M. Vagins. *Triangulation with the International Supernova Network, in First International Workshop on the Supernova Early Alert Network*. Boston University, Bound photocopied transparencies, 1998.

[Wis95] R. Wischnewski et al. *A System to Search for Supernova Bursts with the* AMANDA *Detector*. *Proceeding of the 24th International Cosmic Ray Conference (ICRC 95), Rome*, Vol.**1**:658, 1995.

[Wis97] R. Wischnewski. *SN-Reader SOFF97*, 1997 .
`http://www.ifh.de/~wischnew/amanda/sn_ 97.html`.

[Wis99] R. Wischnewski et al. *Supernova Burst Analysis with the* AMANDA *Neutrino Telescope*. *Proceeding of the 26th International Cosmic Ray Conference (ICRC 99), Salt Lake City, UT*, August 1999. HE.4.2.07.

[Woo97] S. E. Woosley. *SN 1987A - Presupernova Evolution and the Progenitor Star*. *astro-ph/9705146*, 1997.

[Wor99] G. Worthey. *Astro 201: H-R Diagram*, 1999 .
`http://astro.sau.edu/~astro/html/lec-hr.html`.

[Wos99] K. Woschnagg et al. *Optical Properties of South Pole Ice at Depth from 140 to 2300 Meters*. *Proceeding of the 26th International Cosmic Ray Conference (ICRC 99), Salt Lake City, UT*, August 1999. HE.4.1.15.

[WW89] S. Woosley and T. Weaver. *The Great Supernova of 1987*. *Scientific American*, 1989.

[WW96] A. Weigert and H. J. Wendker. *Astronomie und Astrophysik*. VCH Weinheim, New York Basel Cambrige Tokyo, 1996.

Appendix

A Astrophysical Constants

- The absolute luminosity, L, of a thermal radiator or black body, of radius, R, and effective temperature, T_{eff}, is :

$$L = 4\pi\sigma R^2 T_{eff}^4 \text{ erg s}^{-1} \qquad \text{Stefan} - \text{Boltzmann law} \tag{A.45}$$

- The radiant flux, S, of a black body observed at a distance D, is :

$$S = L/(4\pi D^2) = \sigma R^2 T^4 / D^2 \text{ erg s}^{-1}\text{cm}^{-2}. \tag{A.46}$$

- The effective temperature of a black body T_{eff}, with a radiant flux S, is given as:

$$T_{eff} = (S/\sigma)^{-4} \text{ K} \tag{A.47}$$

- The distance at which the mean radius of the Earth's orbit about the Sun subtends a angle of one second of arc is defined parallax-second or parsec

$$\begin{aligned} &1\ pc = 3.0856 \cdot 10^{16}\text{m}; \\ &1\ pc \simeq 3 \cdot 10^{16}\text{m}; \\ &1\ kpc \simeq 3 \cdot 10^{19}\text{m}. \end{aligned} \tag{A.48}$$

- The distance that the light travels in one year, is called light-years:

$$\begin{aligned} &1 \text{ light} - \text{year} = 9.4605 \cdot 10^{15} \text{ m} \\ &1\ pc = 3.26 \text{ light} - \text{year} \end{aligned} \tag{A.49}$$

- The mean radius of the Earth's orbit about the Sun is defined the astronomical unit:

$$1\ AU = 1.49578 \cdot 10^{11} \text{ m}. \tag{A.50}$$

- Hubble showed, that the whole system of galaxies is not stationary but is expanding uniformly, so that the distance of a galaxy r from our own Galaxy is proportional to its velocity of recession v, away from it:

$$v = H_0 \cdot r \tag{A.51}$$

$$H_0 = 50 \text{ Km s}^{-1}\text{Mpc}^{-1} \text{ or } 80 \text{ Km s}^{-1}\text{Mpc}^{-1} \tag{A.52}$$

where H_0 is the Hubble's constant. Due to the difficulty of measuring accurate extragalactic distance, the Hubble's constant is often written:

$$H_0 = 100h \text{ Km s}^{-1}\text{Mpc}^{-1} \tag{A.53}$$

where the parameter h is to be chose, as preference by the reader.

- Solar mass:

$$M_\odot = 1.9891(4) \cdot 10^{33} \text{ g} \tag{A.54}$$

- Jupiter mass

$$M_{Jup} = 0.001 \ \ M_\odot \tag{A.55}$$

- Milky Way mass

$$M_{MilkyWay} = 10^{11} \ \ M_\odot \tag{A.56}$$

- Solar radius

$$R_\odot = 6.955 \cdot 10^{10} \ \ \mathrm{cm} \tag{A.57}$$

- Solar mean density

$$\rho_\odot = 1.41 \ \ \mathrm{g\ cm}^{-3} \tag{A.58}$$

- Solar constant

$$S_\odot = 1.368(4) \cdot 10^6 \ \ \mathrm{erg\ s}^{-1}\mathrm{cm}^{-2} \tag{A.59}$$

- Solar absolute luminosity

$$L_\odot = 4\pi(AU)^2 S_\odot = 3.85(1) \cdot 10^{33} \ \mathrm{erg\ s}^{-1} \tag{A.60}$$

B List of stable OMs

OM-Nr.	String-Nr.	Pos. on String	μ_{Rate} (Hz)	σ_{Rate} (Hz)
1	1	1	253	7
2	1	2	332	9
3	1	3	295	9
4	1	4	323	8
7	1	7	292	8
8	1	8	285	8
9	1	9	284	8
10	1	10	285	8
11	1	11	294	8
12	1	12	279	8
13	1	13	307	8
14	1	14	267	8
15	1	15	274	8
16	1	16	316	8
19	1	19	359	9
20	1	20	276	8
21	2	1	279	8
22	2	2	337	9
23	2	3	246	8
24	2	4	249	7
25	2	5	317	8
26	2	6	301	8
27	2	7	288	8
29	2	9	318	9
30	2	10	282	8
31	2	11	281	8
33	2	13	305	8
35	2	15	326	9
38	2	18	274	8
45	3	5	323	9
46	3	6	266	8
48	3	8	302	8
49	3	9	324	9
52	3	12	289	8
53	3	13	243	7
54	3	14	279	8
55	3	15	302	8
56	3	16	308	8

OM-Nr.	String-Nr.	Pos. on String	μ_{Rate} (Hz)	σ_{Rate} (Hz)
58	3	18	283	8
59	3	19	297	8
60	3	20	342	9
65	4	5	281	8
66	4	6	319	8
68	4	8	267	8
70	4	10	287	8
71	4	11	284	8
72	4	12	303	8
73	4	13	321	8
74	4	14	223	7
75	4	15	233	7
77	4	17	266	8
92	5	6	1177	19
97	5	11	989	17
98	5	12	1019	18
101	5	15	1126	18
102	5	16	1129	18
103	5	17	1127	19
107	5	21	1100	19
108	5	22	1149	19
109	5	23	1123	19
110	5	24	970	17
111	5	25	959	17
112	5	26	1114	19
114	5	28	1037	18
115	5	29	992	18
117	5	31	913	16
118	5	32	966	17
119	5	33	926	16
120	5	34	1076	18
121	5	35	888	16
123	6	1	1016	17
125	6	3	1247	20
129	6	7	1038	17
130	6	8	971	17
131	6	9	1058	18
137	6	15	918	16
138	6	16	1127	19
139	6	17	1022	17
140	6	18	1103	18
141	6	19	997	17
142	6	20	894	16
144	6	22	968	17

OM-Nr.	String-Nr.	Pos. on String	μ_{Rate} (Hz)	σ_{Rate} (Hz)
145	6	23	1074	18
146	6	24	1085	18
147	6	25	1074	18
148	6	26	990	17
149	6	27	938	16
150	6	28	998	18
153	6	31	1056	19
154	6	32	1183	19
155	6	33	1062	18
156	6	34	1005	17
157	6	35	988	17
158	6	36	888	16
161	7	3	1121	17
163	7	5	1163	19
164	7	6	1090	18
165	7	7	1054	18
166	7	8	1063	18
169	7	11	1157	19
170	7	12	1200	19
171	7	13	1054	18
173	7	15	1118	19
174	7	16	1154	19
175	7	17	1025	17
176	7	18	1146	18
177	7	19	1147	19
178	7	20	1070	17
179	7	21	1038	18
181	7	23	968	16
182	7	24	1164	19
183	7	25	940	17
184	7	26	1134	19
188	7	30	1018	17
189	7	31	1040	18
191	7	33	959	16
193	7	35	852	15
194	7	36	1084	18
200	8	6	1076	19
201	8	7	1098	18
203	8	9	1113	18
204	8	10	1122	19
205	8	11	1159	19
206	8	12	926	16
207	8	13	1062	18
208	8	14	872	16

OM-Nr.	String-Nr.	Pos. on String	μ_{Rate} (Hz)	σ_{Rate} (Hz)
211	8	17	1141	19
212	8	18	1183	19
213	8	19	1006	17
214	8	20	1241	19
216	8	22	1148	19
217	8	23	1160	19
218	8	24	1115	18
219	8	25	1156	18
230	8	36	1058	17
237	9	7	1134	19
238	9	8	1013	17
239	9	9	909	16
240	9	10	1112	19
241	9	11	997	17
242	9	12	998	17
243	9	13	1191	19
244	9	14	1072	18
245	9	15	1042	18
246	9	16	1018	17
247	9	17	1016	18
248	9	18	1193	20
249	9	19	983	17
250	9	20	1200	19
253	9	23	991	17
254	9	24	1109	18
256	9	26	1186	20
265	9	35	946	17
266	9	36	903	16
268	10	2	1052	18
269	10	3	1077	18
270	10	4	1000	17
271	10	5	1259	20
272	10	6	1049	18
275	10	9	1053	18
279	10	13	1105	19
280	10	14	1152	19
281	10	15	1187	19
283	10	17	1182	19
284	10	18	1178	19
285	10	19	1020	17
286	10	20	1069	17
287	10	21	906	17
288	10	22	1146	19
290	10	24	954	17

B.1 List of *Good* OMs 97 which become *Bad* in 98 and *vice versa*

OM-Nr.	String-Nr. 97	Pos. on String	OM-Nr.	String-Nr. 98	Pos. on String
3	1	3	37	2	17
16	1	16	43	3	3
49	3	9	44	3	4
71	4	11	51	3	11
72	4	12	63	4	3
92	5	6	64	4	4
117	5	31	67	4	7
201	8	7	202	8	8
249	9	19	228	8	34
280	10	14	251	9	21
290	10	24	252	9	22

B.2 List of OMs 97 rejected by the Cleaning Algorithm

OM-Nr.	String-Nr.	Pos. on String	μ_{Rate} (Hz)	σ_{Rate} (Hz)
37	2	17	252	7
42	3	2	626	14
43	3	3	313	9
44	3	4	274	8
51	3	11	245	7
63	4	3	276	8
64	4	4	351	10
67	4	7	324	9
69	4	9	312	9
76	4	16	185	6
202	8	8	1317	21
228	8	34	1046	18
251	9	21	1157	19
252	9	22	1150	19
289	10	23	1101	18

C List of Problematic OMs (Pre-Cleaning)

- (A) OMs which show a high noise rate with respect to the mean value of stable OMs
- (B) OMs which show an unstable behavior of the noise rate during long-term periods
- (C) OMs which show a low noise rate with respect to the mean value of stable OMs
- (D) OMs which are considered dead, i.e. with a zero average noise rate or extremely high
- (E) OMs which were turned off
- (F) OMs which which are considered bad for some reasons
- (G) OMs which were bad influenced because of disturbances from surface electronics

OM-Nr.	String-Nr.	Pos. on String	μ_{Rate} (Hz)	σ_{Rate} (Hz)	Why removed
5	1	5	332	12	A
6	1	6	338	12	A
17	1	17	335	23	A
18	1	18	-	12	A
28	2	8	-	-	D
32	2	12	-	-	D
34	2	14	298	8	F
36	2	16	994	21	A
39	2	19	-	-	D
40	2	20	-	-	F
41	3	1	704	16	A
47	3	7	-	-	F
50	3	10	-	-	F
57	3	17	-	-	D
61	4	1	1031	23	A
62	4	2	-	-	D
78	4	18	-	-	D
79	4	19	-	-	D
80	4	20	-	-	D
81	4	21	-	-	E
82	4	22	-	-	E
83	4	23	-	-	E
84	4	24	-	-	E
85	4	25	-	-	E
86	4	26	-	-	E
87	5	1	1019	17	B
88	5	2	1123	18	B
89	5	3	1193	19	B
90	5	4	1149	18	B

OM-Nr.	String-Nr.	Pos. on String	μ_{Rate} (Hz)	σ_{Rate} (Hz)	Why removed
91	5	5	1237	20	B
93	5	7	1007	17	B
94	5	8	1091	18	B
95	5	9	1035	18	B
96	5	10	12	1	D
99	5	13	1168	19	B
100	5	14	1025	17	B
104	5	18	1167	19	B
105	5	19	1039	18	B
106	5	20	33	2	C
113	5	27	1086	19	B
116	5	30	1091	18	B
122	5	36	1103	53	B
124	6	2	1106	19	B
126	6	4	1177	19	B
127	6	5	1144	18	B
128	6	6	1162	19	B
132	6	10	938	17	B
133	6	11	1164	19	B
134	6	12	1154	20	B
135	6	13	1010	17	B
136	6	14	929	17	B
143	6	21	-	-	F
151	6	29	1116	19	B
152	6	30	1196	20	B
159	7	1	1131	19	B
160	7	2	1141	19	B
162	7	4	1073	18	B
167	7	9	0.6	0.4	F
168	7	10	1088	17	B
172	7	14	-	-	F
180	7	22	1128	18	B
185	7	27	1125	20	B
186	7	28	-	-	B
187	7	29	1261	19	B
190	7	32	38	2	C
192	7	34	1136	18	B
195	8	1	6	0.4	C
196	8	2	1140	18	B
197	8	3	19	1	C
198	8	4	1136	18	B
199	8	5	4	0.7	C
209	8	15	1100	18	B
210	8	16	1161	19	B

OM-Nr.	String-Nr.	Pos. on String	μ_{Rate} (Hz)	σ_{Rate} (Hz)	Why removed
215	8	21	57	3	C
220	8	26	1106	18	B
221	8	27	1079	18	B
222	8	28	1004	18	B
223	8	29	1028	17	B
224	8	30	1170	19	B
225	8	31	1103	19	B
226	8	32	1156	19	B
227	8	33	-	-	C
229	8	35	1902	115	A
231	9	1	-	-	F
232	9	2	-	-	F
233	9	3	6147	-	A
234	9	4	9512	-	A
235	9	5	20	2	C
236	9	6	1006	17	B
255	9	25	8190	-	A
257	9	27	1569	25	A
258	9	28	1271	18	B
259	9	29	5720	48	A
260	9	30	7108	-	A
261	9	31	1879	24	A
262	9	32	1876	24	A
263	9	33	1162	19	B
264	9	34	941	16	B
267	10	1	-	-	F
273	10	7	1091	18	B
274	10	8	1113	18	B
276	10	10	1249	20	B
277	10	11	1013	17	B
278	10	12	1124	19	B
282	10	16	1017	17	B
291	10	25	993	17	F
292	10	26	811	14	C
293	10	27	1084	18	G
294	10	28	1003	18	G
295	10	29	1062	19	G
296	10	30	1084	18	G
297	10	31	1006	17	G
298	10	32	1289	19	G
299	10	33	1088	16	G
300	10	34	1165	18	G
301	10	35	1005	17	G
302	10	36	1239	19	G

Zusammenfassung

AMANDA ist ein Hochenergie-Neutrinoteleskop, das am geographischen Südpol aufgebaut wird. Das hauptsächliche Ziel von AMANDA ist die Suche nach hochenergetischen Neutrinos, um kosmische Phänomene bei höchsten Energien zu untersuchen und ein neues Fenster ins Universum zu öffnen.
Da Neutrinos ungeladene Teilchen sind, können sie astronomische Entfernungen geradlinig durchfliegen und uns verborgene Informationen des Kosmos übermitteln. Als Kandidaten für astronomische Neutrinoquellen werden unter anderem Aktive Galaktische Kerne (AGN) und die in ihrer Ursache noch ungeklärten Gammastrahlungs-Ausbrüche (GRBs) angenommen. Neutrinoteleskope werden in transparenten Medien wie Wasser oder Antarktis-Eis aufgebaut. Das Detektionsprinzip ist die Registrierung der Ankunftszeit des Cherenkovlichts, das von relativistischen geladenen Teilchen emittiert wird.
Obschon AMANDA für hochenergetische Neutrinos gedacht ist, ist der Detektor auch in der Lage, nach Neutrinoausbrüchen aus Supernovaexplosionen zu suchen.
Statt die Spur von hochenergetischen Muonen, die den Detektor durchfliegen, zu rekonstruieren, sucht man beim Nachweis von niederenergetischen Neutrinos aus Supernovae nach einem kohärenten Anwachsen der Rauschrate innerhalb einer Zeitspanne von 10 Sekunden. Das ist das Prinzip, nachdem mit AMANDA Supernova-Neutrinos gesucht werden.
In dieser Diplomarbeit wird zuerst eine detaillierte Einleitung über Sternentwicklung und die Supernovatheorie gegeben. Die Sternentwicklung findet in der sogenannten "Hauptsequenz" statt, wo die massivsten Sterne zu gravitationsbedingten Supernovaexplosionen führen können. Supernovae werden hauptschächlich durch ihre beobachtete Spektren und ihre Explosionmechanismen klassifiziert. Das Ende des Theoriekapitels ist dem Thema Neutrinoausbrüche aus "*core*"-kollabierenden Supernovae gewidmet, mit denen die überwältigende Energiemenge des Sterns freigegeben wird. Neutrinos aus einer Supernova wurde bisher lediglich aus der SN 1987A beobachtet.
Kapitel 3 beschreibt die Möglichkeit, Supernovaneutrinos mit AMANDA zu beobachten. Kapitel 4-6 fassen die Detektorcharakteristika, die gegenwärtigen Kentnisse der optischen Eigenschaften des Südpol-Eises und eine kurze Beschreibung über die Hardware der Supernova-Elektronik zusammen. Kapitel 7-8 beschäftigen sich mit den Daten-Bearbeitung, mit den Verständnis der Daten und mit dem beobachteten nicht-poissonschen Verhalten des Rauschens. Kapitel 9 gibt eine kurze Beschreibung der angewendeten Monte-Carlo-Methoden, die benutzt wurden, um das Rauschen und das erwartete Signal wiederzugeben. Kapitel 10-12 beschäftigen sich mit den Methoden, die für die Analyse angewendet wurden, und mit der Berechnung des erwarteten Signals, das von verschiedenen Faktoren beeinflusst werden kann. In Kapitel 13 werden die Detektorparameter, das Signal-zu-Rauschen-Verhältnis (S/N) in Abhängigkeit von der Galaktischen Sichtweite bestimmen, und die gegenwärtigen Monitorierungs-Fähigkeiten von AMANDA diskutiert. Vergleiche mit anderen Experimenten werden in Kapitel 14 beschrieben, und die obere Grenze für Galaktische Supernovakollapse gegeben. Im Kapitel 15 wird die Möglichkeit beschrieben, AMANDA in das internationale Supernova-Projekt (SNEWS) einzubinden, und das Prinzip der "Triangulierung" einer Supernova angedeutet. Die Diplomarbeit schließt mit dem Kapitel über die Entwicklung eines AMANDA Supernova Trigger Algorithmus (ASTA).
Aus der Analyse kann man schließen, daß AMANDA fähig ist, Neutrinoausbrüche aus Supernovaexplosionen zu suchen. Für die Analyse wurde ein "*Main Analysis*" Progamm entwickelt, welches ein wesentlicher Bestanteil für die "off-line" Supernova-Analyse ist. Aus einer Gesamtzahl von 302 Photomultipliern (PMs), die zu AMANDA-B10 gehören, wurden eine Selektion von 170 "guten" PMs getroffen, die eine langfristige Stabilität von zwei Jahren aufgewiesen haben.

Trends und Diskontinuitäten der kombinierten Rauschrate aller stabilen PMs werden durch die Anwendung einer "*Moving Average*" Methode wirksam entfernt. Um potentielle SN-Neutrinoausbrüche von nicht-gaussischen Rauschraten-Variationen zu separieren, wurde eine "*Maximum-Lihelihood*" Methode angewandt.
Es wurde keine Evidenz für SN-Neutrinoausbrüchen innerhalb einer effektiven Meßzeit von 220 Tagen gefunden.
AMANDA-B10 ist mit einer 90% -Effizienz auf 8.8 kpc Entfernung sensitiv (d.h. es würde 90% aller Supernovae in einer Entfernung von 8.8 kpc registrieren), bei einer Imitationsrate von eins pro Jahr. Auf der Basis der Resultate von Bahcall und Piran für die Sternverteilung der Sterne in unserer Galaxie, kann AMANDA bis zu 50% der Milchstraße mit S/N$\geq$ 1 ein beobachten, wobei als Signal "S" Supernovakollaps pro Jahrhundert angenommen wurde und "N" die Imitationsrate ist. Dabei ist die Schwelle so gelegt, daß ein SN-Signal pro Jahr durch Rauschen imitiert wird. Die 90% -Konfidenzgrenze c.l. für die Galaktische Supernovarate, die man aus den 18 Monaten analysierter Daten erhalten kann, ist 8.59 $year^{-1}$. Die Skalierung dieser Grenze zur Meßzeit des LVD-Detektors, ergibt 0.93 $year^{-1}$. Voraussagen für einen künftigen Ausbau zu einem 250 PMs-Detektor, angenommen eine Rauschrate von $\sim$ 300 Hz, würde möglich bis zu 14 kpc monitoriren (d.h. 79% der Galaxy). wehrend mit einem 800 PMs-Ausbau könnte man die ganze Galaxy bedecken.
ASTA, ein AMANDA Supernova Trigger Algorithmus wurde entwickelt, der zuverläßig für einen Test von 11 Daten-Tage keinen falschen Alarm gegeben hat.

Erklärung

Hiermit bestätige ich, daß ich die vorliegende Arbeit ohne unerlaubte fremde Hilfe angefertigt habe.

Ich bin mit der Auslage meiner Diplomarbeit in der Bibliothek der Humboldt-Universität zu Berlin einverstanden.

Berlin, den 8 Februar 2000

Andrea Silvestri